A New Inductive-Annealing Dual Electrochemical Cell for Crystal Alloy and Thin-Film Electrode Voltammetry: Water Oxidation on Single- and Polycrystalline Ir Surfaces

vorgelegt von
M.Sc. Ebru Özer
geb. in Berlin

von der Fakultät II - Mathematik und Naturwissenschaften
der Technischen Universität Berlin
zur Erlangung des akademischen Grades

Doktorin der Naturwissenschaften
- Dr. rer. nat. -

genehmigte Dissertation

Promotionsausschuss:

Vorsitzender:	Prof. Dr. Thomas Friedrich (TU Berlin)
Gutachter:	Prof. Dr. Peter Strasser (TU Berlin)
Gutachter:	Prof. Dr. Michael Bron (MLU Halle-Wittenberg)

Tag der wissenschaftlichen Aussprache: 18.12.2018

Berlin 2019

The creative adult is the child who survived after the world tried killing them, making them grown up. The creative adult is the child who survived the blandness of schooling, the unhelpful words of bad teachers, and the nay-saying ways of the world. The creative adult is in essence simply that, a child.

Julian F. Fleron

Danksagung

Ich möchte mich an dieser Stelle bei all jenen bedanken, die durch ihre fachliche und persönliche Unterstützung bei der Erstellung dieser Arbeit geholfen haben.

Ganz besonders möchte ich mich bei Herrn Professor Peter Strasser für die Betreuung der Arbeit bedanken, für die zahlreichen Gespräche und mannigfachen Ideengebung, die mich hoch motiviert haben, dieses spannende und gleichzeitig herausfordernde Thema anzugehen. Ich möchte mich bei Herrn Professor Michael Bron für die Bereitschaft, ein Gutachten für diese Arbeit zu erstellen, bedanken und Herrn Professor Thomas Friedrich für die Übernahme des Vorsitzes des Promotionsausschusses.

Mein besonderer Dank gilt Benjamin Paul für die großzügige fachliche Unterstützung, wichtigen Denkanstößen und für seine Mithilfe bei technischen Fragen, die zu einem wesentlichen Fortschritt der Arbeit beigetragen haben. Ich danke Herrn Paul für die Durchführung der SEM Messungen. Bei Herrn Camillo Spöri möchte ich mich für die zahlreichen Gespräche auf intellektueller und persönlicher Ebene danken, die maßgeblich dazu beigetragen haben, dass die Arbeit in dieser Form vorliegen kann. Des Weiteren übernahm Herr Camillo Spöri freundlicherweise das Korrekturlesen dieser Arbeit. Ich möchte mich ganz herzlich bei Frau Dr. Stefanie Kühl für die Durchführung von TEM und SAED Messungen bedanken und für ihr offenes Ohr für Fragen. Zusätzlich danke ich Herrn Dr. Dirk Berger und Herrn Sören Selve vom ZELMI für die Focussed Ion Beam Präparation einer cross-section Lamella. Ich danke dem Fritz-Haber-Institut der Max-Planck-Gesellschaft für den Zugang zu XPS Messungen und besonders Dr. Hong Nhan Nong-Reier für die Durchführung dieser Messungen. Herrn Dr. Ilya Sinev danke ich für XPS und AFM Messungen und Frau Andrea Mingers für ICP-MS Messungen. Vielen Dank an Herrn Jorge Araujo für DEMS-Messungen und Thomas Kropp aus der Arbeitsgruppe von Herrn Professor Mavrikakis für die durchgeführten DFT Berechnungen.

Für ein angenehmes und lustiges Arbeitsklima möchte ich mich allen Mitgliedern der Arbeitsgruppe von Professor Peter Strasser sowie den Mitarbeitern der Werkstatt bedanken. Eine sehr große Hilfe war hierbei der Glasbläser Herr Carsten Hirschfeld und Frau Zarina Pawolek, die mich in die Welt der Dünnfilme eingeführt hat. Herrn Manuel Gliech danke ich für seine immer vorhandene Hilfsbereitschaft. Ein besonderer Dank gilt meinen Eltern und meinen Geschwistern, die mich durch mein gesamtes Studium begleitet haben und immer an meiner Seite waren.

Abstract

Proton exchange membrane (PEM) electrolyzers are considered as the most promising candidates for the supply of high purity hydrogen through water electrolysis. As a non-polluting technology these electrolyzers enable to store surplus electricity of intermittent renewable power sources. In the highly acidic corrosive media of PEM electrolyzers, noble metal materials and their oxides represent the state-of-the-art electrocatalysts combining high activity and stability towards the oxygen evolution reaction (OER) at the anode. However, efficiency losses during the mechanism of OER, which limit the catalytic performance must first be surmounted to establish an affordable and sustainable energy cycle.

The first step towards understanding of the complex processes during the mechanism of OER is to create a stable foundation with suitable model systems that is essential to further improve the activity and stability of existing electrocatalysts and to reduce the amount of noble metal content. Well-defined single crystal catalysts offer the opportunity to develop valuable and substantial concepts in the research field. In this context, a coupled inductive electrochemical crystal preparation and test station was developed combining rapid inductive heating of any type of crystal surface to temperatures up to 1900 °C. The setup allows not only for electrochemical studies in distinct electrolytes but provides an environment for precise temperature studies in controlled gas atmospheres by means of finely adjusted infrared sensors. The annealing process of electrodes can be immediately followed by any type of electrochemical deposition, modification, or characterization in two distinct three electrode chambers. The development and construction of this setup was followed by verification measurements with Pt(111), Ir(111) single crystals and polycrystalline Ir (Ir_{poly}) electrodes. The independence of both electrochemical chambers through pump-controlled supply and withdrawal of liquid electrolyte facilitates the study of electrodeposition of Ni on single crystalline Ir(111) electrodes. The accessible phenomena of metal overlayer formation on a foreign metal substrate has become an important strategy to modify the electronic structure of catalyst surfaces. The process of Ni electrodeposition was initially optimized using Ir_{poly} electrodes in preliminary measurements to identify the potential range of Ni deposition. In a second step, the potential range was examined in detail to find a correlation between applied potential and deposited Ni amount. Based on these findings, the OER activity of two Ni-modified distinct Ir_{poly} electrodes was analyzed and compared to the pristine unaltered cylinder. Hereto the polycrystalline Ir electrode was modified by formation of a Ni overlayer (OL) through electrochemical potential-controlled deposition. This step was followed by inductive annealing in a reduced atmosphere to form a near-surface alloy (NSA). Interestingly, the electrocatalytic OER activity of Ir_{poly} was enhanced by the addition of Ni in form of an overlayer in both alkaline and acidic solution. The improved OER performance in acidic milieu in comparison to the NSA system was deduced to the Ni leaching process increasing the amount of surface OH groups. In alkaline media, the highly hydrophilic Ni surface adatoms are responsible for the lower overpotential.

In order to bridge the study of well-defined crystal model catalysts and catalysts which are relatively ill-defined, two distinct Ir metal films on Ti substrate as model systems were contrived for a more profound study of the electrocatalytic OER. Here, the synthesis procedure comprised the reductive heating of either calcined (Ox) or uncalcined Ir acetate films (Ac). Whereas the latter were characterized by a variable morphology and alterable electrochemical properties in dependence of heating time, the additional calcination step in the second synthesis route creates a predominant surface structure exhibiting a high OER Faraday efficiency in chloride containing solution. Here, the Ac film exposed to heating the shortest time exhibits the highest OER activity compared to the Ox films and longer heated Ac films.

Zusammenfassung

Protonen-Austausch-Membran (engl. PEM) Elektrolyseure sind vielversprechende Anwärter für die Bereitstellung von Wasserstoff hoher Reinheit über die Wasserelektrolyse. Der Einsatz der Elektrolyseure als umweltfreundliche Technologie ermöglicht die Speicherung von Überschusselektrizität aus erneuerbaren Energiequellen. Aufgrund der hoch korrosiven Bedingungen in PEM Elektrolyseuren sind Edelmetall Materialien und ihre Oxide die Elektrokatalysatoren der Wahl. Auf der Anodenseite kombinieren sie eine hohe Aktivität und Stabilität in der Sauerstoff Evolutionsreaktion (engl. OER). Dennoch müssen Effizienzverluste während der OER, die die katalytische Leistung reduzieren, überwunden werden, um einen bezahlbaren und nachhaltigen Energiekreislauf zu generieren.

Um die komplexen Prozesse während der OER zu verstehen, muss zunächst eine stabile Basis mit geeigneten Modellkatalysatoren geschaffen werden. Diese sind essentiell für weitere Aktivitäts- und Stabilitätsverbesserungen bereits existierender Elektrokatalysatoren und für die Reduktion des Anteils an Edelmetall. Wohl-definierte Einkristall-Katalysatoren ermöglichen die Entwicklung wertvoller Konzepte in der Forschung. In diesem Zusammenhang wurde eine gekoppelt induktive elektrochemische Kristall Präparations- und Versuchsstation entwickelt, in der jegliche Kristalloberflächen bei Temperaturen bis zu 1900 °C rapide geheizt werden können. Dieser Aufbau ermöglicht nicht nur elektrochemische Studien in unterschiedlichen Elektrolyten. Mithilfe von fein justierten Infrarot Sensoren können auch präzise Temperaturstudien in einer kontrollierten Gas Atmosphäre durchgeführt werden. Nach dem Glühprozess der Elektroden können jegliche elektrochemischen Depositionen, Modifizierungen oder Charakterisierungen in zwei verschiedenen Drei-Elektroden Kammern umgesetzt werden. Die Konstruktion des Aufbaus wird unterstützt durch Verifikationsmessungen mit Pt(111) und Ir(111) Einkristallen und polykristallinen Ir (Ir_{poly}) Elektroden. Beide elektrochemischen Zellen können unabhängig voneinander mit Elektrolyten über eine Pumpe versorgt werden, was den Prozess der Ni Elektrodeposition auf Ir(111) vereinfacht. Die Abscheidung von Metallen auf fremde Metallsubstrate ist eine wichtige Strategie in der Modifizierung von elektronischen Strukturen von Kristalloberflächen. Zunächst wurde die Ni Elektrodeposition auf Ir_{poly} untersucht, um den Potentialbereich der Ni Abscheidung zu identifizieren. Anschließend wurde dieser Potentialbereich detaillierter untersucht und eine Korrelation zwischen Potential und abgeschiedener Ni Menge hergestellt. Auf Basis dieser Erkenntnisse wurde die OER Aktivität von zwei Ni-modifizierten Ir_{poly} Elektroden untersucht und ein Vergleich mit dem unveränderten Ir_{poly} aufgestellt. Hierzu wurde der Polykristall mit Ni bedeckt (OL, engl. overlayer) mithilfe der potential-kontrollierten Deposition. Durch induktives Heizen wurde der OL in eine oberflächennahe Legierung (NSA, eng. near-surface alloy) umgeformt. Interessanterweise wurde die elektrokatalytische OER Aktivität des Ir_{poly} durch Hinzufügen von Ni in Form eines OL sowohl im sauren als auch im basischen Elektrolyten erhöht. Die verbesserte OER Leistung im sauren Milieu m Vergleich zum NSA Katalysator kann auf die Ni Auflösung zurückgeführt werden, die den Anteil an OH Gruppen auf der Oberfläche erhöht. Im alkalischen sind die stark hydrophilen Ni Atome verantwortlich für das geringe Überpotential.

Um wohl-definierte Kristallstudien bis hin zu nicht definierten Katalysatorsystemen zu überbrücken, wurden zwei verschiedene Ir Metall Filme auf Ti Substrat als Modellsysteme entwickelt. Hierzu wurden sowohl kalzinierte (Ox) als auch unbehandelte (Ac) Ir Azetat Filme induktiv geheizt. Die Morphologie letzterer ist variabel mit veränderbaren elektrochemischen Eigenschaften in Abhängigkeit der Heizdauer. Der zusätzliche Kalzinierschritt erzeugt eine vorherrschende Oberflächenstruktur mit einer hohen OER Faraday Effizienz in chloridhaltiger Lösung. Der am kürzesten geheizte Ac Film zeigt hierbei die höchste OER Aktivität im Vergleich zu den Ox Filmen und länger geheizten Ac Filmen.

Table of Contents

Chapter 1 Introduction, Motivation, and Goals

One of the most technical challenges of modern living has been the development of sustainable and efficient energy solutions. Within the scope of the impending threat of fossil fuel scarcity, a severe energy and environmental challenge, including local air pollution and climate change and global warming is ahead of us. The global phenomena of climate change and global warming pose a fundamental threat to humanity and impact species and places all over the planet. The unequivocal warming of the atmosphere and ocean has been proceeding over many decades and has led to massive ice mass loss in Greenland, Antarctica and the Arctic. The indispensable impacts of climate change include further rise of the sea level caused by melting of ice sheets and glaciers and expansion of warmed seawater. As not only the sea level but also the rate of sea level rise has increased over the last decade, flooding and damage of deadly storms are only some of the effects. Changes in the climate system have been observed since the 1950s and have predominantly been caused by burning of fossil fuels. The finite resources and energy carriers have irreparably harmed the environment by releasing gases (greenhouse gases), which trap the heat in Earth's atmosphere. These compounds are the fundamental reason of the greenhouse effect inducing extreme weather and climate changes since the mid of the 20th century. It is reasonable that human and industrial activities over the past 50 years have raised the temperature of the planet due to growing levels of atmospheric concentrations of carbon dioxide (CO_2), methane (CH_4) and nitrous oxide (N_2O).[1]

The supply of clean and competitively priced energy is thus an issue, which must be addressed with urgency. In the near future, the use of renewable sources to store electrical energy is considered as the key technology in reducing the consequences and effects of global warming and climate change. An advanced electrical energy system based on chemical and methods will make this technology indispensable in achieving economic independency from fossil fuels. However, the question repeatedly rises of how the growing energy and electricity demands e.g. for transport services can be met and might be answered with a combined electrolysis-fuel cell process using hydrogen as a secondary energy carrier. Notice that the most abundant element in the universe, pure hydrogen gas, is scarce in earth's atmosphere. As of today, 96 % of the global hydrogen production is still being

generated from fossil fuels, such as natural gas (steam reforming), propane, or methanol. The generation of electricity in Germany in the year 2017 (see Figure 1) from renewable energy carriers was determined to ~ 38 % with an increase of 5 % compared to last year. Globally, the share of power generation from renewable energy sources increased from 7.4 % to 8.4 %.[2]

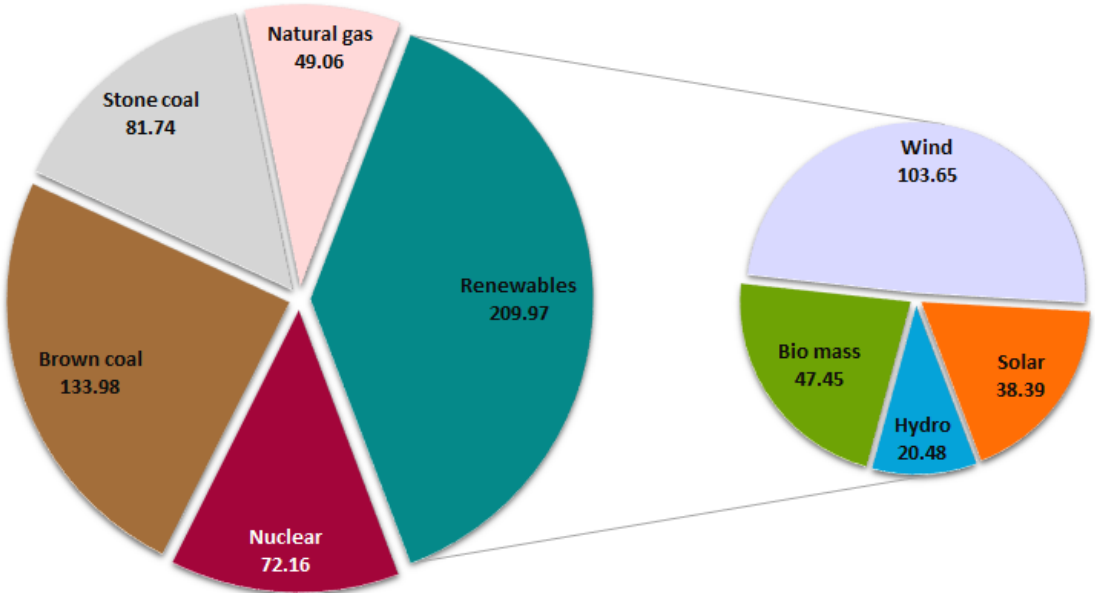

Figure 1 | Sources of energy carriers for the power production in Germany in 2017 in units of TWh (%). Data obtained from[3].

An alternative and non-polluting way of producing hydrogen is water electrolysis using solar generated electricity. In a first step of the combined procedure, hydrogen is being produced via electrolysis of water and can be stored under pressure in gas bottles or tanks. The fuel cell, which then converts the energy produced by the oxidation of hydrogen to water into electric power, is a promising technology for the application as a source of electricity. This cycle of a Hydrogen Economy has been gaining increased attention in recent years and has been the focus of intensive research and development, as the combustion process of hydrogen is clean and only water is being produced. However, the lack of experience in the use of hydrogen as a chemical energy carrier including the requirements of storage systems to fulfill the renewable energy intermittency, e.g sunlight, are only some of the major causes of a still lacking market in electrical energy storage technologies based on renewable devices.

Electrochemical storage systems, however, are for the most part well-developed devices and are being widely used for electronic systems. These devices include

rechargeable batteries such as lead acid batteries, nickel cadmium and nickel metal hydride (NiCd, NiMH) batteries, and lithium ion batteries, which have widely replaced NiMH batteries in portable and mobile devices.[4]

1.1 Proton Exchange Membrane (PEM) Water Electrolysis

In order to overcome the challenges and potential barriers, which hamper the application of water electrolysis on a large-scale, much effort has to be out into developing efficient electrode materials catalyzing the reaction on the way to an energy storage solution based on hydrogen as a flexible energy carrier. The process of water electrolysis can be divided into three categories; electrolyzers using an alkaline electrolyte, a solid ion conducting oxide and proton exchange membrane (PEM) based water electrolyzers.[5] Alkaline electrolyzers were the first commercialized electrolysis system in which the cathode and anode electrodes (often based on nickel) are separated by a gas-tight diaphragm. The separator is permeable to hydroxide ions and water molecules. The reaction takes place in concentrated KOH solution (25 – 30 wt.%) at temperatures between 65 and 100 °C.[6] However, one of the major drawbacks of alkaline electrolyzers are the high crossover rates of the produced gases through the diaphragm. It limits the electrolysis system to operate at low roads and at high pressures. These processes not only reduce the efficiency of the electrolyzers, but also produce harmful concentration levels of hydrogen in the anode chamber with reduced load. The technological disadvantages associated with alkaline electrolyzers can be overcome with the use of a solid sulfonated polystyrene membrane in PEM water electrolyzers.[7] There are a number of advantages that these devices offer, namely the operation at high current densities at low applied cell voltages and the low gas crossover rate of the membrane, which enables the production of high purity hydrogen. The compact system design due to the usage of a solid electrolyte further enables high operational pressures. Ultimately, less energy is required to further compress and store hydrogen. PEM based electrolyzers are ideal candidates to be powered by renewable energy sources based on their distinguished dynamic load behavior in combination with their rapid response.[8, 9] Another benefit is the low electrolyte volume with a resulting low heat capacity.[8] However, the harsh corrosive acid environment provided by the proton exchange membrane requires corrosion-resistant interconnects (current collector, separator plates) and durable, low-cost and active catalysts. The main challenge facing PEM water electrolyzers thereby is the limitation of the catalyst materials to noble and scarce metals, such as Pt, Ir and Ru based electrodes. In combination with the sluggish oxygen evolution reaction (OER),

the main focus of the research performed in field of PEM electrolysis will be on the reduction of the noble metal loading to decrease the capital costs, while at the same time increase the operating current density.

1.2 Electrocatalysts for OER in PEM Water Electrolyzers

In the first article of PEM electrolyzers in the year 1973, Russel *et al.*[10] already developed first thoughts on the reduction of the loading of noble materials for PEM. In 1966 Damjanov *et al*.[11] found the OER activities of Ir, Rh and Pt-Rh alloys in the order: Pt < Pt-Rh < Rh < Ir.[12, 13] Extensive research on Pt, Ir and Ru electrodes with the focus on their activity towards the OER in acidic media was carried out by Burke *et al*. between the years of 1971 and 1976. In the study of the oxygen evolution and corrosion behavior of Ir electrodes in comparison to Pt anodes, a 30 time's higher reaction rate was observed for Ir in both acidic and alkaline media. At potentials higher than 1.8 V, the sharp increase in current density was attributed to the formation of a higher oxidation state of the anodic film and thereby to a change in the oxygen evolution mechanism. It is postulated, that the subsequent reaction with water induced the corrosion process of the electrode.[14] Oxygen evolution on porous ruthenium dioxide-coated titanium electrodes is assumed to proceed over an unstable surface oxide RuO_3 whose decomposition is catalyzed by protons and might explain the increased rate of the OER in acidic media.[15]

In the study of the activity-stability relationship of a number of platinum group metal oxides by Danilovic *et al.* the following activity trend was found: Au < Pt < Ir < Ru < Os.[16] Interestingly, these monometallic oxides showed a reverse stability trend, speaking in favor of a link between those observations. In spite of its superior activity, Os oxide was being established as unsuitable for application as a catalyst in the OER due to its extraordinarily low Faraday efficiency for oxygen evolution. Its place at the top of the volcano top is owed to the fact that measured current includes a significant amount of dissolution current. Consequently, the dissolution behavior of the electrode during OER needs to be observed to determine objective information on the electrocatalytic activity.

Ru and Ir oxides have attached a great deal of importance among the transition metal oxides as electrocatalysts for the OER due to their high metallic conductivity and their low onset of oxygen evolution. However, as observed for Os oxide, Ru oxide catalyst display a high corrosion rate during OER.[17] It is suggested, that the

dissolution is initiated by a higher oxidation state, as previously discussed. Combined X-ray photoelectron spectroscopy and cyclic voltammetry measurements by Kötz and co-workers proved the presence of a highly corrosive Ru(VI) species (also referred to as RuO_3).[18-20] Based on these findings, a model reaction mechanism for Ru and Ru oxide electrodes was proposed, in which the corrosion product was identified as RuO_4 As proposed by Cherevko *et al.* the high corrosion rate, or in other words, the low stability of Ru originates from the reaction mechanism itself.[21, 22]

Rather, the focus of research is directed to Ir and Ir oxide catalysts, which are identified as the state-of-the-art electrocatalysts for the OER.[23-26] The slightly lower activity in comparison to Ru and Ru oxide catalysts is compensated by their considerable higher stability and corrosion-resistance. As previously discussed, the use of pure Ir oxide as an anode catalyst is limited by its high material costs, thus mixed oxides in which the loading of Ir is reduced, have been the focus of research in the development of highly active materials with long lifetime. Affordable oxides, such as SnO_2, Ta_2O_5, and TiO_2 are intended to serve as a stable and resistant matrix without affecting the electrocatalytic properties of the active material, but at the same time having a positive impact on IrO_2 stability.[27] In an attempt to combine the high catalytic activity of Ru with the high stability of Ir, binary IrO_2-RuO_2 electrode materials were designed to act as promising OER catalysts. However, there are different views amongst the scientific community on the question of surface stability of Ru and surface segregation of Ir. Even though, all authors agree on the overall stabilization of the catalyst with an increase in Ir content, the origin in the durability of the material during polarization is not yet fully understood. Kötz and Stucki presumed that both oxides occupy an identical electronic band.[28] However, Danilovic *et al.* suggested the stabilization of the surface Ru to be the result of Ir surface segregation.[16]

Using *in situ* X-ray absorption spectroscopy (XAS) and X-ray photoelectron spectroscopy (XPS) Pfeifer *et al.* established a hypothesis to elucidate the enhanced activity of Ir oxide based catalysts in the OER.[29-31] In combination with theoretical calculations, they concluded that a highly reactive electrophilic O^{I-} species is formed in the mixed-valent $Ir^{III/IV}$ matrix during the OER. By monitoring the electronic structure of the active surface species at different potentials (near-edge X-ray absorption fine structure (NEXAFS) of the O K-edge) an increase in the O^{I-} amount was observed with increasing oxygen evolution activity. They hypothesize that the electrophilic nature the O^{I-}species facilitates the O-O bond formation by a

nucleophilic attack of either water molecules of OH species. Interestingly, the less active crystalline rutile-type IrO_2, which was lacking the electrophilic species O^{I-}, showed an increased concentration of O^{I-} when defects were introduced into the structure by removing Ir^{IV} and $4e^-$. The lack of an electron in the O 2p state of the O^{II-} species forced the O^{I-} species to form μ_2-oxo rather than μ_3-oxo bridges.

It was found more recently that the OER performance of Ir catalysts can be considerably increased by the formation of mixed Ir-Ni oxides. These materials not only offer beneficial effects on the electrocatalytic activity, bimetallic oxides further help in reducing the noble metal content. A systematic tuning of the OER activity at a reduced Ir amount was achieved by IrNi@IrO_x core@shell nanoparticles synthesized by Nong *et al.*[24] Here, the optimum amount was found to be at ~ 77 at.% Ni. These efficient nanoparticulate systems were formed by electrochemically leaching of surface Ni and controlled surface oxidation of Ir. A systematic variation of the Ir to Ni ratio in thermally prepared IrNi mixed oxide thin-film model catalysts by Reier *et al.* resulted in volcano shaped graphs.[25] The utmost OER performance (based on geometric surface area, surface charge and applied Ir mass) was realized in the high Ni range. Reier *et al.* assumes that electrochemical leaching of Ni prior to oxygen evolution potentials generates a surface partially covered with OH groups.[25] As these OH species are presumably weakly bond to the bulk oxide, they are expected to be the cause of the improved activity. A second theory by Pfeifer *et al.*[29-31] assumes that the Ni vacancies and the subsequent need to compensate the charge forms highly electrophilic O^{-1} species from O^{2-} which presumably facilitate the nucleophilic attack of water in the proposed acid-base OER mechanism presented in the following chapter.

The aforementioned potential optimization approaches aim, on the one hand, in minimizing the noble metal content to attain cost-effective catalyst material for PEM based water electrolyzers with high sustainability. On the other hand, the performance can exhibit a strong dependence on the synthesis conditions of the active sites. Notice the difference between thermally and electrochemically prepared oxides. The former are known for their higher stability during OER and can be prepared by either thermal oxidation of metallic Ir or decomposition of suitable precursors such as Ir acetate or Ir acetylacetonate.[23, 32-34] The temperature of calcination, the applied gas atmosphere and the precursor inevitably affect the OER performance.[33, 35] In the study of thin-film Ir oxide model catalysts, Reier *et al.* found a strong dependence of the electrocatalytic activity on the calcination

temperature.[33] Here, films calcined at low temperatures displayed the lowest overpotential, however, exhibited a poor stability. The number of potential scans, the upper potential limit and the electrolyte are some of the factors, which influence the characteristics of electrochemically oxidized Ir oxide OER catalysts. These are just a few examples of how sensitive the electrocatalytic properties of OER materials react on either synthesis parameters or the addition of supplementary components in mixed catalysts.

1.3 Motivation, Hypothesis, and Goals

The synthesis and development of new and improved catalyst materials based on Ir oxide offers a tremendous potential as future application in proton exchange membrane (PEM) based water electrolyzers. However, the high sensitivity of the performance device to the synthesis parameters demands a careful and selected (in terms of parameters) investigation and analysis. In order to acquire new knowledge of the underlying phenomena, and possibly to develop new catalytic processes, an enhancement of the scientific basis is crucial. To gain fundamental insight, the reactions of utmost importance in heterogeneous electrocatalysis such as deposition and adsorption are investigated on single crystalline surfaces, or in general on well-defined surfaces. Low index planes of Pt, Au, Ag and Pd single crystals have been the subject to extensive study in an attempt to establish a correlation between different facets and atomic arrangement and their resulting electrochemical activity.[36-40] Nanoparticulate materials in industrial applications show a rather complex behavior with regard to the structural and electronic effects of the surface, which are highly distinct from the macroscopic properties of the material. Well-defined model system help in finding out the basic processes involved in the catalysis of the reactions of interest on a molecular level. In the development of novel and efficient catalytic processes, the catalyst design is a highly interdisciplinary effort. In order to comprehend the mechanism of the respective reaction, establishment of structure-activity relations are the key aspects to attain efficient use of energy and raw materials and to overcome limitations in electrocatalysis. A tremendous effort needs to be put into the understanding of material surface properties, which dictate not only the activity but also selectivity and lifetime of the catalyst. Thus, studying electrocatalytic reactions start from elucidating the interdependence of the catalysts' activity, structure and stability and subsequently using that knowledge to perform structural modifications.

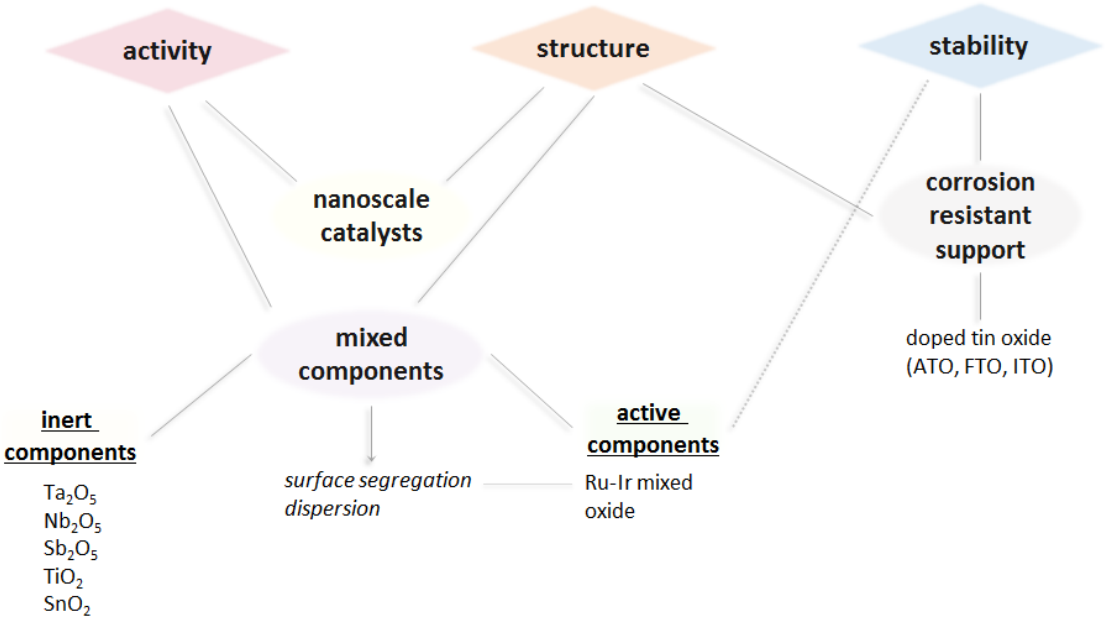

Figure 2| Uncovering the activity-structure-stability relationship by identifying the material properties determining the OER activity and stability with model systems.

The three essential challenges in the structure-activity-stability-relationship are schematically displayed as a flow chart in Figure 2. A large part of research and development in heterogeneous catalysis focuses on the reduction of the cell voltage and thus the increase of the materials' activity. However, we have to keep in mind that the OER performance of the catalysts in acidic media are already quite high, compared to alkaline electrolyzers. With Ir being one of the scarcest elements on earth, a majority of the OER studies have been focusing on reducing the costs of the catalysts by reducing the loading or utilizing mixed components. The former can be realized with nanoscale catalysts that combine a reduced noble metal content with a high surface area. The mixed components on the other hand can either contain an active component as in the Ru-Ir system. Here, the corrosion rate of Ru oxide was reduced remarkably by surface segregation of Ir oxide. The significant instability of Ru oxide during OER and its scarcity make it necessary to follow a different approach, such as the use of inert oxidic components, for example Ta_2O_5, Nb_2O_5, Sb_2O_5, TiO_2 and SnO_2. To realize a high dispersion of Ir Oh *et al.* synthesized doped and corrosion resistant SnO_2 supports with high surface areas.[41]

Therefore, to uncover the dependence of these elements on each other it is essential to identify the material properties, which determine the activity and stability in the underlying electrocatalytic reaction. A fundamental study demands a suitable

model system. Ideally, it allows creating a correlation between the orientation of a surface and its electrochemical reactivity in the complex behavior of the OER.

As apparent from Figure 2, different surface compositions may have an influence on the electronic structure and thus on the performance and stability qualities of the catalyst and necessitates a precise synthesis and characterization procedure. The great variability of the underpotential deposition (UPD) process to alter the topmost layer of catalyst materials requests single or at least poly crystalline surfaces to experimentally determine the adsorption energies of the created new active sites to the desired intermediates. The surface coverage of the metal adatoms, the nature of the solute metal and further the composition of the nearest layers will have a sensible effect on the electrocatalytic activity of the desired reaction. The discovery of the underpotential deposition (UPD) phenomena in the mid-20th century has opened the door to new opportunities for the modification of catalyst's topmost atomic layers. The key challenge, however, lies in the predictability of the binding energies and their resultant effect in the catalytic reaction.

Surface science and heterogeneous catalysis have much in common, however, there is a gap between both subjects in terms of the materials employed. An approach to bridge the gap is the use of model systems, which with the use of appropriate surface science tools, provide profound insights into the geometric structure and electronic or chemical properties of heterogeneous catalysts. These studies need further attention in elucidating the chemistry and physics occurring at the surfaces and interfaces of catalyst and electrolyte. The main goal of this thesis is to implement suitable model systems with the aid of which the activity and stability in the OER can be examined under controlled and uniform conditions. Hereafter, catalyst materials with the required structural and chemical properties can be synthesized in future projects. With the help of modern surface analytical methods, data sets will be extracted on a molecular level.

Based on the high sensitivity of catalytic reactions to the heterogeneous interface between the catalyst surface and electrolyte, the aim of this thesis is to establish a correlation between the activity and the nanoscale structure of the catalytic surface. The relevance of single-crystal modeling is mirrored in the set-up of an inductive and electrochemical crystal chamber, which is presented and validated in Chapter 5. The objective of Chapter 5 is to meet the requirements to perform electrocatalysis and surface modifications on well-defined materials, especially Ir-based electrodes, in a cost-effective alternative to ultra-high vacuum (UHV) chambers. Incorporating

innovated and unique feature into the setup, it should simplify the work with highly sensitive single crystal electrodes and guarantee a precise infrared temperature display in a controlled gas atmosphere.

The functionality of the inductive electrochemical chamber will be further validated and utilized in Chapter 6 studying the electrodeposition of Ni on single and polycrystalline Ir electrodes. The resulting electronic effects after controlled thermal treatment of the modified surfaces will be measured by means of electrocatalytic performance in the OER. Given the great structure sensitivity of carbon monoxide oxidation and the various neighboring crystallites in a polycrystal, CO stripping measurements will be performed on the pristine and Ni-modified polycrystalline Ir electrodes to uncover preferential adsorption sites of Ni. Insights and knowledge gained from these studies should help in designing functional catalyst materials. However, as the hanging meniscus configuration does not allow for rotation of the electrode in the custom-made chamber, mass transport limitations may occur for the study of single crystal electrodes.

A second type of adequate model systems will be presented in Chapter 7. Homogeneous thin-film catalyst layer prepared on Ti substrates are known to offer great control over mass transport effects and are ideal to examine the complex catalytic process of OER with surface sensitive analytical techniques. IrO_x electrocatalysts have been widely studied as promising candidates for the oxygen evolution reaction (OER). However, these studies are far from being complete due to the lack of knowledge between the structure and composition of the materials and their activity in the OER. The main object of most studies aims at improving the performance of the applied electrocatalysts. However, a thorough comprehension of the material‘s composition and structure and electrochemistry is fundamental to solve the drawbacks of activity losses at the anode side in PEM electrolyzers. To uncover the structure-activity-stability relationship of heterogeneous electrocatalysis two synthesis procedures will be developed as the conditions under which the catalyst materials are produced have a significant outcome on the OER performance. Relating to thermally prepared oxides this comprises the applied temperature, gas atmosphere and in particular the precursor, which in turn has a significant effect on the morphology. These oxides display a higher stability but lower activity in contrast to electrochemically oxidized metals. Here, the performance and electrochemical properties of selected electrochemically prepared oxides is studied using inductively reduced thin-film metallic Ir model catalysts. The

emphasis on this chapter lies in creating a model system, in which the activity of the electrode material can be tuned under uniform experimental conditions for future performance comparisons and performance enhancements. The utilization of the custom-made setup introduced in Chapter 5 will guarantee a high control of temperature and reduction time. The well-established spin-coating procedure produces homogenous and smooth films, which then will be either directly reduced in the inductive setup or calcined under air to Ir oxide prior to reduction to metallic Ir thin-films. To investigate the chemical nature of the dominant Ir oxide species existing at different states of electrochemical oxidation, the electrochemical characterization will be complemented by physico-chemical techniques, especially spectroscopic methods.

Chapter 2 The Electrocatalytic Oxygen Evolution Reaction (OER) on Ir Based Catalyst Systems

In the following chapter, the current state of knowledge of the oxygen evolution reaction (OER) on Ir based catalysts in acidic environment is discussed to lay the foundation of future catalyst optimization and forward the progress in the development of proton exchange membrane (PEM) water electrolysis. Initially, thermodynamic and kinetic aspects of water splitting will be presented to take the first step in uncovering the complex multistep oxygen evolution reaction. In a second step, detailed mechanistic insights into the reaction mechanism will be given using DFT calculations in order to unveil reaction intermediates and scaling relations.

2.1 Thermodynamics of Water Splitting[42, 43]

In the early 1789 the Dutch merchants Deiman and van Troostwijk first discovered water electrolysis by discharging the electric potential difference between two gold electrodes immersed in water.[44, 45] In the following chemical equation *(2.1)*, the simple water splitting reaction is written.

$$H_2O\ (liquid) \rightarrow \frac{1}{2}\ O_2\ (gas) + \ H_2\ (gas) \qquad \textbf{(2.1)}$$

The total energy that is required to cause the reaction given in equation *(2.1)* to proceed under standard temperature (*25 °C*) and pressure (*1 atm*) (STP) is the enthalpy $\Delta_R H^0$ of *285.58 kJ mol-1* (endothermic). The Gibbs free energy change $\Delta_R G^0$ of water splitting is equal to *236.96 kJ mol-1* (endergonic) and is supplied to the electrodes as electrical energy. An additional thermal energy input ΔS of *48.62 J mol-1 K-1* is required as heat. These thermodynamic variables can be associated with the following equation.

$$\Delta_R H^0 = \Delta_R G^0 + T\Delta S \qquad \textbf{(2.2)}$$

For the reversible cell reaction, the change of the Gibbs free energy can be related to the equilibrium potential E_{eq}^0 according to equation *(2.3)*:

$$\Delta_R G^0 = n\ F\ E_{eq}^0 \qquad \textbf{(2.3)}$$

Here, n denotes the transferred electrons per water molecule $n = 2$ and F is the Faraday constant (*96485 C mol-1*). At standard conditions an equilibrium potential of *1.229 V_{SHE}* can be calculated, which is the minimum voltage required for water

splitting. However, at this voltage, an additional heat input is needed to keep the reaction temperature at a constant value and to prevent the cell from cooling down. With higher operation temperature, the change of Gibbs free energy of water decomposition and the equilibrium potential decrease continuously. In addition, the reactions occur at faster rates and the losses are lowered. If electrical energy is the only source of energy provided to drive the water splitting reaction, the so-called thermo-neutral potential of the cell is *1.482 V* and corresponds to $\Delta_R H^0/nF$.

The cell voltage represents how efficient the water splitting system operates. The higher the voltage, the higher the losses due to overpotential. If only losses within the cell are taken into account, the efficiency of electrolyzers η can be estimated with the operating and the thermo-neutral voltage as given in equation *(2.4)*.

$$\eta = 1.482\ V/E_{cell} \qquad \textbf{(2.4)}$$

The following aspects determine a favorable energy efficiency and thus a small operating cell voltage: *(i)* low ohmic losses achieved by directly contacting the electrode with the membrane, *(ii)* highly active catalysts, which reduce the overpotential and *(iii)* operating the system at high temperatures. The apparent experimental overpotential, which defines the difference between the potential at which the reaction practically proceeds and the thermodynamically determined equilibrium potential, can be caused e.g. by resistances, mass transport and charge transfer resistances, that is sluggish interfacial reaction processes taking place at the electrodes. The origin of these overpotential regarding catalytic processes will be discussed in section 2.2. The dissociation of water in acidic electrolyte proceeds in two half-cell reactions as presented in equations *(2.5)* and *(2.6)*.

Anode $\quad 2\,H_2O \rightarrow 4\,H^+ + 4\,e^- + O_2 \quad E^0 = 1.23\,V_{SHE}$ **(2.5)**

Cathode $\quad 4\,H^+ + 4\,e^- \rightarrow 2\,H_2 \quad E^0 = 0.0\,V_{SHE}$ **(2.6)**

The reduction of hydrogen ions at the cathode (equation *(2.6)*) to molecules of hydrogen is referred to as the standard hydrogen electrode (SHE) and its standard electrode potential (E^0_{eq}) at *p(H₂) = 1 bar* and *pH 0* is declared to be *0.0 V* at all temperatures. With changing *pH* value, the standard Nernst potentials of the hydrogen electrode or of any proton- or hydroxide- containing half-cell redox system shift (with reference to SHE scale) according to the following equation.[46]

$$\mathrm{E}^0_{Red-Ox}\,(\mathrm{pH}) = E^0_{Red-Ox_{SHE}} - 0.059\,pH \qquad \textbf{(2.7)}$$

Reference of Nernst potentials to the shifting standard potential of hydrogen at any given pH, i.e. $E^0_{H_2-H^+}(pH)$ (rather than to the SHE value at $pH = 0$) is referred to as the reversible hydrogen electrode (RHE) scale. In practical terms, the reversible hydrogen electrode (RHE) is a hydrogen electrode that is immersed in the electrolyte solution of any given pH that is actually used. For redox systems that do not involve protons or hydroxide, their RHE – based Nernst standard potential values are affected by the pH value in analogy according to:

$$E^0_{Red-Ox_{RHE}}(\text{pH}) = E^0_{Red-Ox_{SHE}} + 0.059\,pH \qquad \textbf{(2.8)}$$

The performance of an electrolyzer can be directly deduced from the polarization curve, which in turn is a function of the operating pressure, operating temperature, flow rates and membrane thickness, just to name a few. In theory, the efficiency of water electrolysis is inversely proportional to the applied cell voltage (V_{cell}) and defines as the rate of H_2 production to the DC power supplied to the electrolyzer. The efficiency of a water electrolyzer can be given as:

$$\eta_{EL} = \frac{1.482\,V}{V_{cell}} \frac{i - i_{loss}}{i} \frac{\eta_{DC}}{1+\zeta} \qquad \textbf{(2.9)}$$

The current losses (i_{loss}) of an electrolyzer are caused by either internal processes or losses of hydrogen due to permeation through the membrane. These diffusion losses are more significant at higher operational pressures. However, high H_2 pressures are required for subsequent storage in tanks. As PEM electrolyzers also require voltage regulation and auxiliary components, such as small pumps to add make-up water and cooling fans, the efficiency of a DC/DC voltage regulator (η_{DC}) and the ratio between parasitic power and net power consumed by the electrolyzer (ζ) need to be taken into consideration.

2.2 Kinetic Considerations

As thermodynamics only describe the behavior of an electrocatalytic reaction at equilibrium (which is defined by a zero net reaction), kinetic equations are essential to define the reaction rate. In the following, the dependence of the current of an electrocatalytic reaction on the electrode potential is established. In this chapter, the dependence of current on the electrode potential will be established with electrode kinetic theory.

The net rate of a typical redox reaction $Ox + ne^- \rightleftharpoons Red$ is given by the difference between the rate of the forward reaction R_f and the rate of the backward reaction R_b and can be written as:

$$R_{net} = R_f - R_b = \frac{i}{nF} = \frac{i_{cathodic} - i_{anodic}}{nF} = k_f \cdot c_{Ox} - k_b \cdot c_{Red} \quad \textbf{(2.10)}$$

The overall current density i can be split into the cathodic and anodic partial current density. The rate constants of the forward and backward reaction (k_f and k_b) are both potential dependent functions. If the forward reaction was an electron accepting process (reduction, cathodic current), the rate of the reaction will increase with greater negative potential. The ability of the electrode to give away electrons becomes easier.

The rates of chemical reactions have been found to be dependent on the Gibbs free energy. The empirical Arrhenius law in equation (*2.11*) describes the effect of temperature T on the rate and is:

$$k = \frac{k_B T}{h} \cdot e^{\frac{-\Delta G^{\ddagger}}{RT}} \quad \textbf{(2.11)}$$

The Gibbs free energy of activation $\Delta G^{\ddagger}$ relates to the transition state formed by the reagents and can be written out with enthalpic $\Delta H^{\ddagger}$ and entropic $\Delta S^{\ddagger}$elements:

$$k = \frac{k_B T}{h} \cdot e^{\frac{-\Delta H^{\ddagger}}{RT}} \cdot e^{\frac{\Delta S^{\ddagger}}{R}} \quad \textbf{(2.12)}$$

$\Delta G^{\ddagger}$ is therefore the Gibbs free energy difference between the reactants and the transition state and dictates the ability of the reactants to reach the transition state. The argument of a short-lived transition state is based on the transition state theory of Eyring.[47] The values of $\Delta H^{\ddagger}$ and $\Delta S^{\ddagger}$ can be put into relation with the activation energy and the frequency factor of the well–known Arrhenius plot:

$$\Delta H^{\ddagger} \approx E_{act} - R \quad \textbf{(2.13)}$$

$$\Delta S^{\ddagger} \approx \mathrm{R} \cdot ln\left(\frac{k_0 h}{k_B T}\right) \quad \textbf{(2.14)}$$

The reactants need the activation energy E_{act} to overcome the energy barrier before they are being converted into products. The frequency factor k_0 is reaction–dependent and refers to the number of attempts needed to surmount the energy barrier.[48]

Figure 3 shows the theory of the activated complex for a typical redox reaction in the form $Red \rightleftharpoons Ox + ne^-$. According to the theory, the activated complex has a

higher free enthalpy than the reduced and oxidized state. The difference between the free enthalpy of the activated complex and the initial state is referred to as $\Delta G_{+}^{\ddagger}$. $\Delta G_{-}^{\ddagger}$ gives the difference between the free enthalpy of the complex and the final state. By applying a potential difference, the free enthalpies for oxidation and reduction change according to equations *(2.15)* and *(2.16)*.

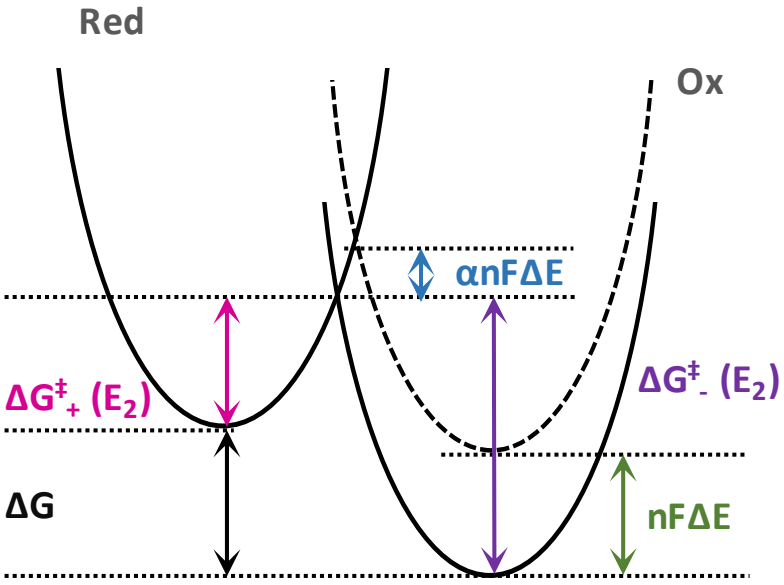

Figure 3| Schematic representation of the potential-dependent free enthalpy of a redox system

$$\Delta G_{+}^{\ddagger}(E_2) = \Delta G_{+}^{\ddagger}(E_1) - \alpha n F \Delta E \qquad \textbf{(2.15)}$$

$$\Delta G_{-}^{\ddagger}(E_2) = \Delta G_{-}^{\ddagger}(E_1) + nF\Delta E - \alpha n F \Delta E = \Delta G_{-}^{\ddagger}(E_1) + (1-\alpha) nF \Delta E \qquad \textbf{(2.16)}$$

The extent of the change is determined by the symmetry factor α, or a transfer coefficient αn, which will appear for a multi-electron transfer reaction. Put simply, the transfer coefficient determines the part of the potential difference needed to transport the electrical charge to the summit of the transition state. Note that for a multistep reaction, the mechanism of the overall reaction including the number of exchanged electrons prior to the rate-determining step need to be taken into consideration.[49] Combining the equations *(2.11)*, *(2.15)* and *(2.16)* and introducing the overpotential η as the difference between applied and equilibrium potential will lead to the Butler-Volmer equation in *(2.17)*:

$$j = j_0 \left[e^{\frac{\alpha n F}{RT}\eta} - e^{-\frac{(1-\alpha)nF}{RT}\eta} \right]. \qquad \textbf{(2.17)}$$

The Butler-Volmer equation as a fundamental basis in electrochemical kinetics considers that both, the cathodic and anodic reaction occur at the same electrode.

The exponential relationship describes the course of a purely activation controlled current in the current density versus potential curve, in other words it considers the kinetics of the reaction alone. In the Butler-Volmer equation, the reaction rate of an electrochemical reaction and the thermodynamic potential are connected. The term j_0 is referred to as the exchange current density and corresponds to the anodic and cathodic partial current flow at equilibrium. Here, the net current is zero, as the current density of the forward reaction equals the current density of the backward reaction. From the amount of the exchange current density, the rates of oxidation and reduction at equilibrium can be determined. With a large value of j_0 a small overpotential is required for a high current flow and vice versa.

2.3 Proposed Reaction Mechanism

As concluded from the previous chapter, the uncovering of the reaction mechanism is of utmost importance, as this knowledge will allow optimizing the efficiency of the electrocatalytic oxidation of water. To date, several reaction mechanisms have been proposed which rely on either kinetic models or DFT calculations. Bockris' outstanding work on electrode kinetics of the electrocatalytic evolution of oxygen has been pivotal for further research in this field. The established mechanisms were based on theoretical kinetic parameters, which were in conjunction with experimentally observed data. He demonstrated that mechanism determination depends on the precise evaluation of Tafel slopes, which in fact are associated with the rate determining steps (*rds*) within the examined reaction mechanism.

Based on DFT calculations, Rossmeisl *et al.*[50-52] proposed a four–electron reaction path which is described by the equations *(2.18)* - *(2.21)*, with * being an active surface site on the catalyst. In this thermochemical analysis, the Gibbs free energy ΔG_x of each individual elementary reaction step, in which the intermediates *HO*, *O* and *HOO* are involved, is calculated as a function of electrode potential. As the adsorption energies between catalyst and intermediates define the value of ΔG_x, the potential needed to facilitate the OER is specific to each individual catalyst.

$$H_2O_{(l)} + * \rightleftharpoons HO^* + H^+ + e^- \quad \textbf{(2.18)}$$

$$HO^* \rightleftharpoons O^* + H^+ + e^- \quad \textbf{(2.19)}$$

$$O^* + H_2O_{(l)} \rightleftharpoons HOO^* + H^+ + e^- \quad \textbf{(2.20)}$$

$$HOO^* \rightleftharpoons O_{2(g)} + H^+ + e^- \quad \textbf{(2.21)}$$

The DFT–predicted peroxide reaction path excludes the formation of O_2 by two adsorbed oxygen atoms on the catalyst's surface, as the activation barrier of the recombination is assumed to be energetically not favorable.[52] It must be borne in mind that the presented reaction mechanism is valid for the participation of only one metal site and is solely based on thermodynamics without the inclusion of any chemical elementary steps. However, this mechanistic proposal is the first step towards a fundamental understanding of the oxygen evolution reaction processes and hence towards further improvements of current electrocatalysts for the OER.

The following chapters will aim at creating a deeper understanding of the OER catalysis with focus on the requirements of catalyst optimization based on structure-activity-stability relations. A special emphasis will be placed on the properties that determine the activity of OER catalysts and hence the origin of overpotential.

2.3.1 Standard Free Energy Diagram

A catalytic reaction, which is accelerated by a heterogeneous catalyst, is a cycle of elementary steps including adsorption, surface reaction, desorption and diffusion of the product. In this catalytic process, weak bonds between the reagents and the catalyst are formed which causes the internal bonds in the reactant molecule to be stretched and weakened. The activation energy between the adsorbed reagents of a catalyzed reaction is significantly smaller than that for an uncatalyzed reaction.[53] However, an optimum catalytic performance is given if the strength of adsorption between the catalyst and the reactants is neither too strong nor too weak. This qualitative principle is given by Sabatier[54] and can be uncovered by plotting the activity of a catalyst versus its binding energy towards the reaction intermediates. If different possible catalyst materials are employed, a characteristic 'volcano' type curve is obtained. The highest catalytic activity can be yielded if the binding energy of the reacting species to the surface is strong enough to produce reaction intermediates. At the same time, the bonding of the molecules have to be weak enough so that products can be released allowing for a high turnover frequency of reactants and products.[55]

Substantial effort is still needed to optimize the rate constant and activity of existing catalysts, which in turn can be directly correlated to the adsorption energies of the reaction intermediates. The DFT–predicted oxygen evolution reaction path presented in equations *(2.18)* - *(2.21)* will be considered in this approach. The

concept of calculating the Gibbs free energies of every reaction step within an overall reaction mechanism allows determining the origin of overpotential for different types of oxide-based electrocatalysts. The constructed standard free energy diagrams in Figure 4 of the proposed reaction mechanism are based on the presumed intermediates *HO*, *O* and *HOO* and their individual binding energies to the catalyst's surface. The calculations (the details of which can be found elsewhere[50]) were made at a pressure at which H_2O in the gas phase is in equilibrium with the liquid phase, at standard conditions and at $U = 0\ V_{SHE}$. Note that for the calculation of the binding energies, additional kinetic barriers were neglected. The presented approach does not only allow for the determination of the potential determining step (*pds*), but also the potential required to make the entire reaction sequence thermodynamically feasible.[51, 52]

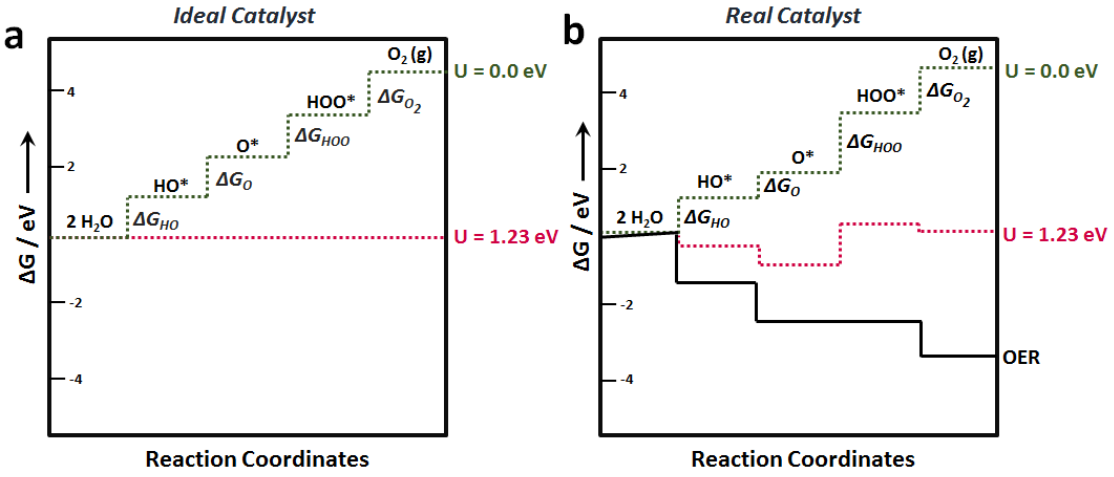

Figure 4| Schematic representation of the Gibbs free energies of the assumed intermediates *HO*, *O* and *HOO* of the four-step OER mechanism proposed by Rossmeisl *et al.*[50-52]. The Gibbs free energy diagram in (a) denotes the binding energies for the ideal catalyst. Here, all four transfer steps have a standard free energy of the same magnitude at zero potential ($U = 0.0\ V_{SHE}$). For a real catalyst (b), higher potentials need to be applied to make the reaction thermodynamically feasible (black solid line).

What makes the ideal catalyst an optimal catalyst, is its ability to realize the oxygen evolution reaction at the equilibrium potential of $U = 1.23\ V$ as depicted in Figure 4. This requires the ideal catalyst surface to bind all intermediates by the same strength, and to display equidistant free energy steps of *1.23 eV* at an electrode potential of *0 V*. Hence, all four individual reaction free energies are being zero at the standard equilibrium potential. In the energy diagram of a real catalyst (see Figure 4b), however, the free energies ΔG of reaction of each elementary step are

dissimilar from each other. The sum of all ΔG_x, however, has to equal the Gibbs free energy of the overall reaction. For most of the catalysts, a large overpotential is required (Figure 4b, black line) so that all steps including the potential-determining step become downhill in free energy.

2.3.2 Structural Effects

Developments in the field of catalyst design require the understanding of effects that influence the observed overall performance. Electrocatalytic reactions are particularly sensitive to alterations in structural and electronic effects of the active sites. Therefore, to design new and efficient materials for OER, the identification of these two major effects is crucial. The structural effects will be examined in this chapter. The electronic effects and their impact on the electrocatalytic properties has been discussed in the previous chapter.

The definition of the 'active site' by Taylor unleashed the concept of applying well-defined model catalysts, e.g. single crystal surfaces, to study the influence of distinct facets, including kinks, steps and cus (coordinatively unsaturated sites) sites, on the catalytic performance and their contribution to the overall electrocatalytic activity. The knowledge obtained from the approach of studying the OER on low-index single crystal surfaces was transformed into different categories, which were extensively reviewed by Koper and Bondarenko.[56, 57]

Materials catalyzing the OER are mainly oxidic-based electrodes and their performance is primary determined by the nature of the existing oxide, which renders much possible the optimization of their surface properties without the employment of doping metals. For the oxygen evolution reaction a surface structure dependence was found inter alia by Stoerzinger *et al.* for IrO_2 and RuO_2 electrodes with the (100) surface being more active in alkaline environments (*pH 13*) than the more stable (110) surface.[58] In the extensive study on oxide formation of Ir(111) and Ir(110) single crystal surfaces for OER showed that the (110) face of Ir was characterized by a lower overpotential in the first scans. The (111) face of Ir, however, reached the activity of Ir(110), suggesting that similar Ir oxide species were formed and that water oxidation occurs preferentially on (110) sites. Of the three low-index surfaces (111), (110) and (100), the (111) surface displays the lowest surface energy making and thus represents thermodynamically the most stable surface orientation.

However, these studies are hampered by accompanying metal dissolution, which alter the single crystal surfaces and further complicate the correlation between electrocatalytic performance and initial surface structure. Interestingly, a surface study on CO_3O_4 by Bergmann *et al.* revealed more insights into the correlation between the stability and activity of catalyst materials.[59] Catalysts, which exhibit a lower stability, show again a high catalytic activity. The reduced stability will benefit in the change of the structure into the active phase, which is catalyzing the reaction. This also explains the high electrocatalytic performance of amorphous materials compared to crystalline structure not only justified by their high surface area.

2.3.3 Scaling Relations and Electronic Effects

From the thermochemical analysis in chapter 2.3.1, it could be derived that the Gibbs free energies of each individual step ΔG_x in the overall reaction sequence has to be smaller than $0\ Jmol^{-1}$ to allow for the OER to proceed. The transfer of one proton and one electron in each individual step of the presented mechanism in equations (2.18) - (2.21) signifies that the free energies of the intermediates can be written as a function of electrode potential. In order to reduce that potential which is needed to meet the condition of $\Delta G_x \leq 0\ J\ mol^{-1}$, the catalyst's surface and hence its activity needs to be altered until all three intermediates *HO*, *O* and *HOO* bind optimally to the catalyst. Rossmeisl *et al.* established a scaling relation between the intermediates suggesting that, in the simplest case, the chemisorption energy of only one intermediate is sufficient to describe and predict the activity of the catalyst in form of a volcano curve.[51, 52] In the same way, however, this means that the individual energy levels of the intermediates cannot be changed separately. For instance, for a wide range of oxides, it was found that the binding energies between the intermediates *HO* and *HOO* maintain a nearly constant difference value independent of the catalyst and their individual binding strength to the surface. This is because their chemisorption energies scale with each other on any given catalyst. Their quasi constant offset of approximately $3.2\ eV$ ($\Delta G^0_{HOO*} - \Delta G^0_{HO*}$), unfortunately, is different from the thermochemically ideal free energy difference of $2.46\ eV$ between both intermediates. If the transfer of two protons and two electrons are taken into account, an insurmountable minimum overpotential of about $0.37\ eV$ will remain even for a catalyst whose binding energy towards *O* is perfectly placed

in the middle of *HO* and *HOO*. This inevitable overpotential can be determined as calculated in the following equation.

$$\left(\frac{3.2\ eV - 2.46\ eV}{2e}\right) = 0.37\ eV \qquad \textbf{(2.22)}$$

On the basis of the universal scaling relation between chemisorption the energies of the three adsorbates, the difference ($\Delta G^0_{O*} - \Delta G^0_{HO*}$) has been taken as suitable descriptor for the OER activity.[50] For a number of different oxide materials, the plot of the overpotential as a function of the descriptor (Figure 5) leads to a volcano shaped activity trend towards the oxygen evolution reaction. The surfaces on the left side of the volcano top have a strong binding energy towards O^*, making the formation of the HOO^* species the potential limiting step of the reaction. However, if oxygen is adsorbed too weakly the potential is limited by the oxidation of HO^* to O^*.

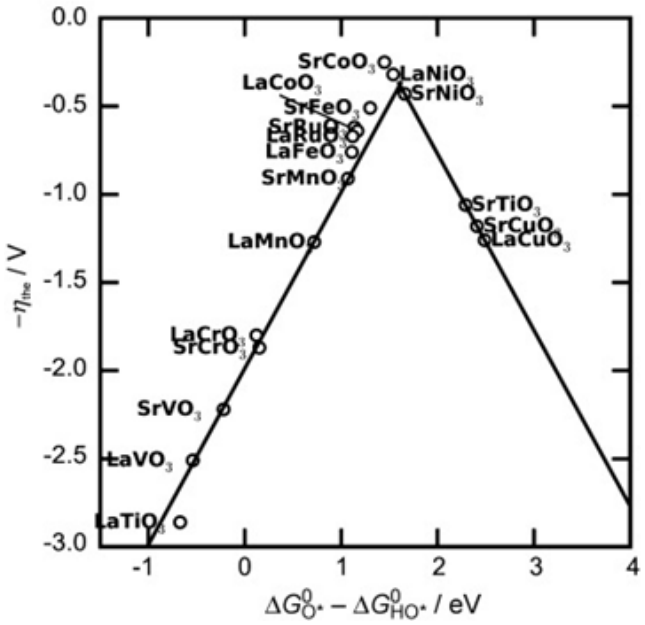

Figure 5 | Volcano shaped activity trend towards oxygen evolution reaction (OER) by plotting the theoretical overpotential η_{the} as function of the difference in binding energies between the intermediates O and HOO ($\Delta G^0_{O*} - \Delta G^0_{HO*}$). The activity of each oxide is determined by the O adsorption energy. Reproduced with permission of John Wiley & Sons.[50]

Here, the difference between the reactivity and activity of the catalysts can be distinguished. The reactivity of a catalyst material depends on its interaction with the intermediates and is thus dependent on the binding energy. The activity in turn is dependent on the reactivity and is a measure of the rate of the reaction.[60] To lower the OER overpotential below the *0.37 V*, the scaling relations of the

intermediates need to be broken. That means that a catalyst enables the change of the *OH* chemisorption energy without a concomitant linear change of the *OOH* chemisorption energy. In the work of Hack *et al.* this important point was taken into consideration as the modification of an oxide catalyst with Ni and Co resulted in an enhanced proton donor-acceptor functionality of the bridging *O* atoms. Given a (110) surface, the dopant on the bridge site facilitates the transfer of hydrogen from HO^* and HOO^* species adsorbed on a cus (coordinatively unsaturated sites, metal surface atom within an oxide with a lower coordination number compared to the bulk) site. This complementary functionality results in a lowering of the energetic states (stronger binding) of two of the intermediates, demonstrating that the addition of a second metal is an approach to overcome the linear correlation of the binding energies within a reaction sequence. The theoretical study of the OER mechanism by Fang *et al.*, however, concluded that the proton-acceptor functionality even exists on pure RuO_2 and is substantial for the reaction to proceed.[61] As introduced by Rossmeisl *et al.*, an attack of a water molecule to form the *O-O* bond is proposed rather than the coupling of two surface *O* groups.[61, 62]

It is evident that the electronic properties of the catalyst material are an important fundamental parameter on which the catalytic activity, selectivity and stability depends on. In this section, the binding energies of the electroactive species were found to be affecting the catalyst's electrocatalytic properties. The binding energies of the intermediates are a function of the electronic structure of the surface, which in turn can be altered by changing the surface composition. A desirable side effect of adding a second component to surface composition is an enhancement of the material's stability. A practical example of how the surface electronic properties can be altered is given with bulk bimetallic alloys. In these systems, the ligand and the strain effect both strongly influence the overall activity. The former describes a change in the electronic structure of the active sites due to different neighboring atoms with distinct atomic numbers. Stress is introduced to the catalyst at the surface in form of a parallel strain if the lattice constants dictated by the bulk material differ from that of the surface. The greater the difference of lattice parameters, the stronger the stress which appears at the interface. Depending on the intensity of the strained layers, the effect in the desired application can be varied. The strain ε of a given surface with the lattice constant a_L is caused by the lattice constant of the bulk a_B. The strain is defined as:

$$\varepsilon = \frac{a_L - a_B}{a_B} \tag{2.23}$$

The effect the strain has on the valence bands will be discussed in section 3.2.

Bimetallic alloys based on Pt and Pd catalyst materials are preferentially employed in proton exchange membrane fuel cell (PEMFCs) for the oxygen reduction reaction (ORR). Pt is one of the most precious and rarest metals on earth, demonstrating the intensive research performed on Pt-based alloys to enhance ORR kinetics and stability.[63-67] An alternative way to optimize the electronic structure catalyst systems is the deposition of a solute metal onto a foreign metal surface at potentials that is positive of the Nernst potential.[68] Electrodeposition as an electrochemical surface process enables a precise modification of catalyst surfaces with a second solute metal to design materials for a variety of applications. The beauty of this process lies in its simplicity to tune the binding energies of the reaction intermediates by only (sub)monolayer amounts of foreign metals. However, there is the challenge of determining the adsorption energies for the intermediates given the variety of different sites. Some examples include overlayers of foreign atoms produced by deposition of an unmodified electrode surface. These overlayers can then be transformed into sub-surface alloys or surface alloys by thermal treatment in a controlled atmosphere. The electronic structure and thus the binding energy to the intermediate species does not depend on the solute material alone, but also on its concentration in the sub-surface region. The initial coverage of the surface can be efficiently controlled by process of underpotential deposition (UPD).

Bimetallic systems in terms of sub-surface and surface alloys offer an effective method to alter the electronic structure of the monolayer, whose properties are determined by the nature of the substrate. In addition to computational methods, fundamental research with single crystal model catalysts prior to implementing real-world nanoparticle.

Chapter 3 Surface Reactivity in Electrocatalysis

3.1 Chemisorption of Adsorbates

In order to understand heterogeneous catalysis in its complexity, it is necessary to gain knowledge about the interaction of a catalyst's surface with its adsorbates. The inclusion of electronic-structure parameters, e.g. number of valence electrons, *d*-band centers and *d*-band widths will allow for a prediction of the reactivity of distinct surfaces.

The *d*-band center model by Hammer and Nørskov[69], which is based on the Newns Anderson formalism[70, 71] on the interaction of a single electronic adsorbate state with a metal surface with quasi continuum bands of electronic states, is an adequate model to predict the activity and reactivity of transition metal surfaces and the effect of alloying. The adsorbate-surface interaction is based on the interplay between the adsorbate states with all the valence states of the transition metal at the surface. In a typical 3d transition metal the delocalized *s* and *p* orbitals form a partly filled broad *sp* band (one s electron for 3d transition metals) in which the electrons behave as a free electron gas over the entire metal. The *d* orbital, however, is more localized and therefore forms a narrow *d*-band. Transition metal have a high density of states near the Fermi level due to unoccupied *d* states. The density of states for a transition 3d metal is given in Figure 6.

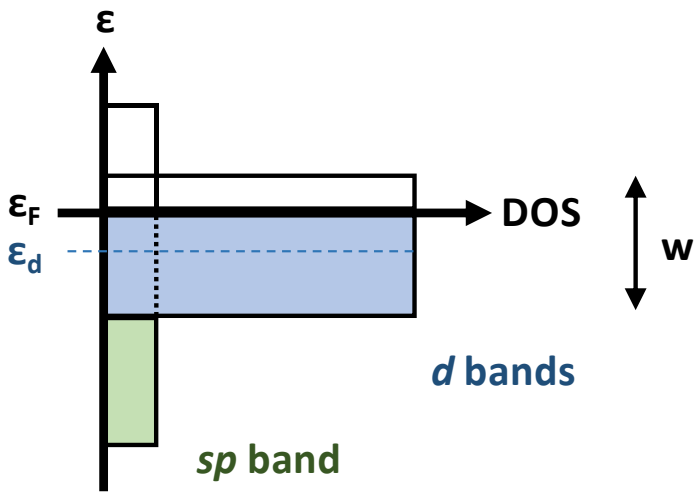

Figure 6| Schematic illustration of the density of states (DOS) of a transition metal displaying the broad *sp* band and the narrow *d* band. The width of the *d*-band around the Fermi level (ε_f) is given by w and ε_d represents the *d*-band center.

Atomic Adsorbates

As the *s* and *p* bands of the transition metals are very similar, the variation in adsorption energies and hence catalytic activity is due to the different fillings of the *d*-band. In Figure 7 the interaction and chemisorption of an adsorbate with a transition metal is illustrated by means of the simple model of an atomic (e.g. oxygen atom) adsorption. When approaching the surface, the valence level of the adsorbate (a) first interacts with the s band of the metal (d), which results in a broadening and downshift in energy of the adsorbate state (b). The stronger coupling of the downshifted level with the narrow *d*-band splits the adsorbate orbitals into an antibonding and bonding element (c).

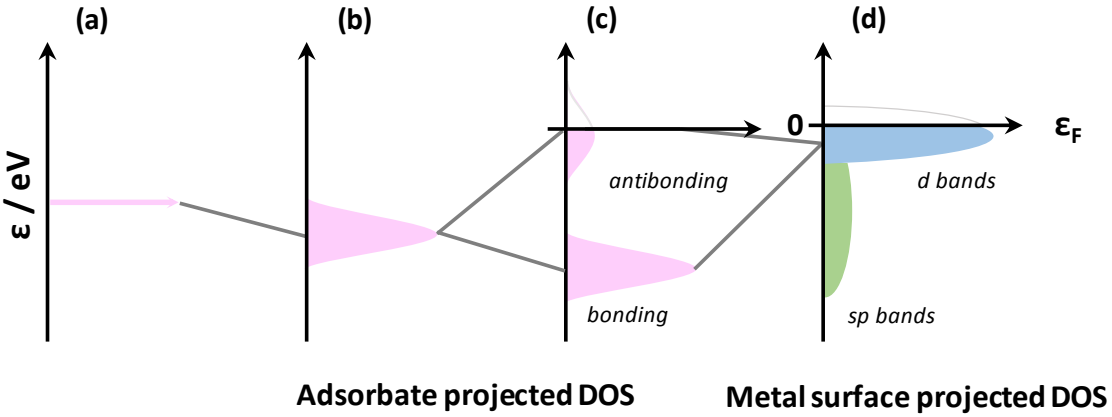

Figure 7| Local density of states (DOS) and change in local electronic structure at (a) an adsorbate atom in vacuum upon (d) adsorption on a transition metal surface. (b) The interaction with the *sp* and *d*-band of a metal surface results in broadening of the adsorbate state due to the single resonance with the *sp* band of the metal. (c) The stronger interaction with the narrow *d*-band gives rise to a bonding and antibonding state.

As mentioned already, the *d*-band filling, or to be more precise, the relative position of the metal *d* states around the Fermi energy (occupied and unoccupied states) determines the resulting interaction with the adsorbate. If the *d*-band center ε_d of the clean metal surface is high in energy (close to the Fermi energy ε_d), the antibonding state of the chemisorbed adsorbate can be shifted up in energy above the Fermi level. These antibonding states remain/become empty, whereby the chemisorption between the metal surface and the adsorbate becomes stronger. The broader the *d*-band, the lower the *d*-band center ε_d, the weaker the bond and the result of the interaction is a single resonance. The narrower the *d* band, the more

the *d*-band center ε_d shifts up in energy and a second resonance, a distinctive antibonding state, will be likely.

The difference in chemisorption energy and hence the bond strength from one metal to the next can be given by the DOS projected onto the states of the chemisorbed atom. Two trends are observed in the periodic table. First, the bond will be stronger, the farther to the left the metal is, however weaker the farther down in the periodic table. 3d, 4d and 5d transition metals on the left side have a relative low *d*-band filling causing the *d*-band to shift up in energy. As a result, more antibonding adsorbate–metal *d*-states will be above the Fermi level and become depopulated.

Molecular Adsorbates

In Figure 8 the interaction of a molecule with a bonding and an antibonding orbital is shown. Here, both of the orbitals contribute to the chemisorption. If the originally antibonding orbital of the molecule shifts below the Fermi level and obtains electron density, the internal bond of the adsorbed molecule becomes weaker. This, however, strengthens the bonding between the metal and the adsorbate and at the same time facilitates the dissociation of the molecule.

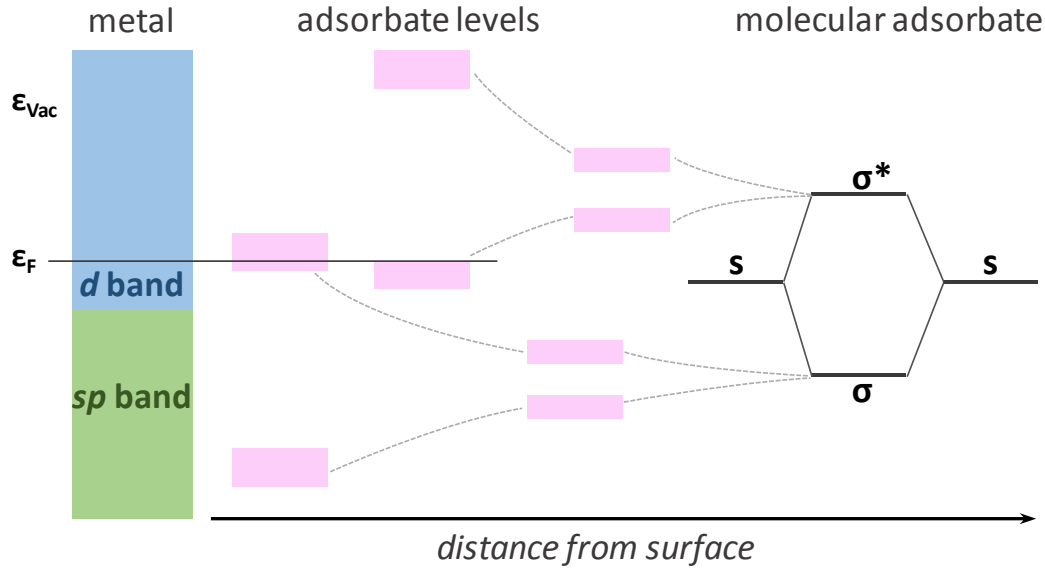

Figure 8| Interaction of the bonding and antibonding orbitals of a molecule adsorbate with the *sp* and the narrow *d*-band of the transition metal. The interaction with the *sp*-band leads to a lowering and broadening of the bands, while the effect of the *d*-band is a splitting of the bands into bonding and antibonding orbitals. Electrons in antibonding orbitals of the adsorbate result in a weakening of the internal bonding.

The energetic position of the adsorbate orbitals mostly results from the interaction with the metals *d*-band or more specifically from the center of the *d*-band. The adsorption energy can be varied through effects of stress and strain in the surface which have an impact on the position of the *d*-band center.

3.2 Effects of Stress and Strain

The reactivity of a surface can be tuned by strain and ligand effects that cause changes in the overlap of the electronic orbitals between the atoms.

By applying strain to the surface, the coordination number and hence the overlap of the *d* orbitals decreases. As a consequence, the *d*-band becomes narrower. In order to maintain the number of *d* electrons, the *d*-band shifts upwards in energy. A higher *d*-band center facilitates the transfer of metal *d* electrons to the lowest unoccupied orbital of the adsorbate, thus increasing the interaction with the adsorbate. This effect of strain explains the higher reactivity of steps and kinks on the surface. Due to their low number of metal neighbors the width of the *d*-band is much lower than of the closely packed atoms.[55]

A shift of the *d*-band and a change in reactivity can also be attained through alloying the desired metal on another metal with a distinct lattice constant which is shown in Figure 9.[72]

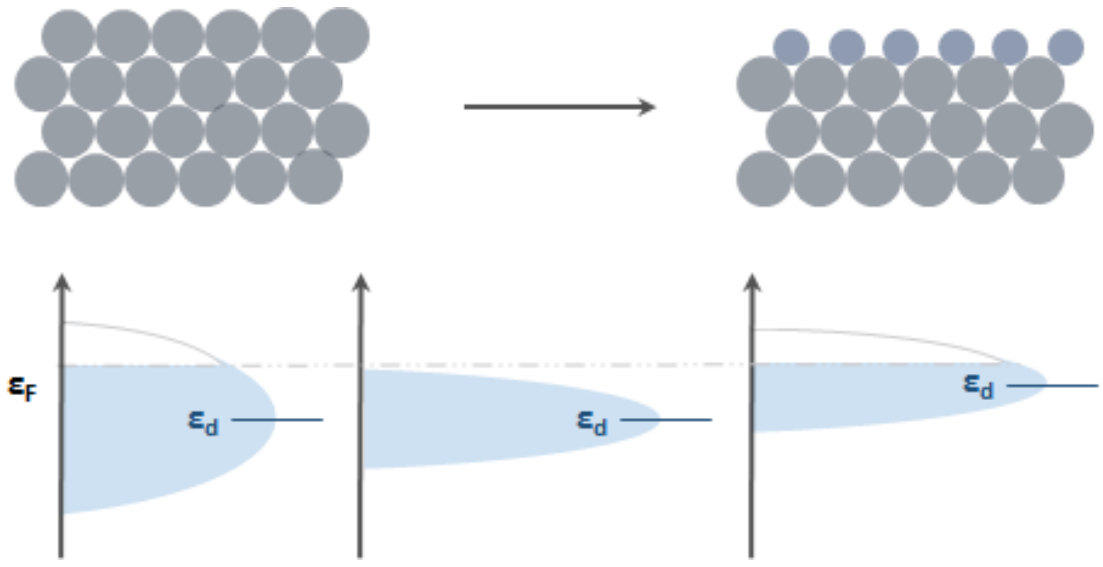

Figure 9| *d*-band center shift obtained by forming an alloy. The *d*-band center ε_d of the metal (grey circles) is raised by the addition of a second metal (blue circles).

This modification of the *d*-band energy depends on two factors, the strain and the ligand effect. Here, the metal overlayer adopts the lattice constant of the host metal

and therefore gets strained or compressed. The electronic interaction between the two metals is referred to as the ligand effect and causes a change of the chemical properties of the surface. Both effects exist simultaneously and are hard to distinguish from one another. In near-surface alloys, however, any modifications in the electronic and the chemical properties can be traced to the ligand effect. In this scenario, the second layer metal atoms adopt the lattice constant of the surface, while any alteration in the surface is due to the ligand effect.[73]

The changes in the *d*-band center for monolayers have been calculated for transition metal substrates by DFT and are illustrated in Figure 10. The diagonal determines the position of the *d*-band center relative to the fermi level for the pure metals. The greater the number of *d* electrons in the *d*-band, the more the position of the *d*-band center shifts down in energy and becomes a core level when completely filled.[74]

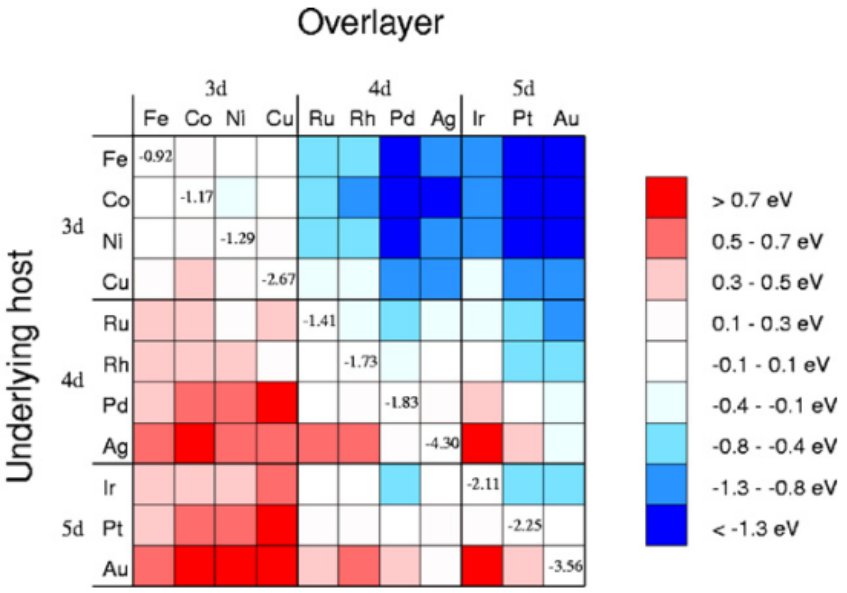

Figure 10 | *d*-band center shifts based on DFT calculations for the concept of an overlayer. The diagonal values represent the *d*-band center of the pure metal, the colored values are the shift relative to the pure metal. Reproduced with permission of Elservier.[74]

The design of new efficient electrocatalytic systems by changing the composition of the topmost atomic layer, thus the electronic structure have been studied extensively using overlayers/films[25, 75, 76] and core-shell nanoparticles[24, 77, 78]. As stressed in section 2.3.3 the electronic structure of the surface determines the catalytic properties of the heterogeneous catalyst at a given potential. Thus, the challenge here is to modify the catalyst surface and hence the binding energy of both

HO^* and HOO^* in a way that O^* is bound neither too strong nor too weak to the surface. The presented theoretical considerations offer an excellent way to optimize the binding energy of the intermediates by introducing stress and strain in order to improve the catalyst activity and approach the ideal case.

Chapter 4 Deposition Processes on Crystalline Surfaces

4.1 Thermodynamics and Fundamentals of Underpotential Deposition (UPD)

The complex process of the electrochemical deposition of metals onto foreign substrates is for the most part experimentally examined using cyclic voltammetric studies in combination with spectroscopic and scattering techniques. However, a thermodynamic analysis of the adsorption potential and UPD shift is indispensable and depends on the energetic contributions of the individual transport processes and the work function differences between the substrate and the depositing metal. The simplified scheme in Figure 11 displays the individual stages contributing to the potential of adsorption and thus to the total Gibbs free energy change (ΔG_{ML}) of a monolayer formation in the UPD process: The solvated ions M^{n+} diffuse to the inner Helmholtz plane (IHP) (ΔG_1) and lose their solvation shell. Once the unsolvated ions reach the surface, a bond between the substrate (S) and the metal (M) is formed (ΔG_3) through electron transfer from the substrate to the metal ions (ΔG_2). To allow the deposition of a foreign metal to occur, desorption of the solvent dipoles adsorbed on the surface of the substrate needs to be taken into account also.

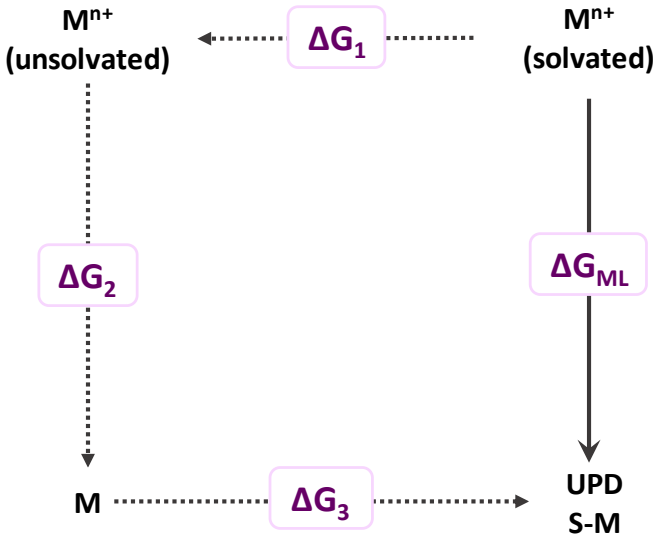

Figure 11| Thermochemical cycle displaying the different energetic stages of underpotential deposition of a monolayer amount of a metal (M) onto a foreign substrate (S)

The total Gibbs free energy change in the monolayer formation (ΔG_{ML}) is the sum of the three Gibbs free energy changes involved in the UPD cycle:

$$\Delta G_{ML} = \Delta G_I + \Delta G_{II} + \Delta G_{II} \quad \textbf{(4.1)}$$

Work ($W_{M^{n+}}$) has to be done to bring the solvated metal ions $M^{n+}$from the bulk to the surface, where it is being reduced by an electron from the substrate. This can be expressed by equation *(4.2)*.

$$\Delta G_1 = W_{M^{n+}} \quad \textbf{(4.2)}$$

The Gibbs free energy change ΔG_{et}^{S} of the electron transfer and $\Delta G^0$of the standard reduction potential M^{n+}/M both contribute to the overall Gibbs energy change of the reduction process ΔG_2 as given in equation *(4.3)*.

$$\Delta G_2 = \Delta G_{e^-}^{S} + \Delta G^0 \quad \textbf{(4.3)}$$

Both the ability of the metal ions to be reduced and the contribution of the substrate as electron source are considered here. As a next step, solvent dipoles desorb from the electrode surface (ΔG_{desor}^{S}) and are being replaced by metal adatoms as a bond between the depositing species and the substrate is formed (ΔG_{S-M}^{inter}). The respective thermodynamics are given in equation *(4.3)*.

$$\Delta G_3 = \theta(\Delta G_{desor}^{S} + \Delta G_{S-M}^{inter}) \quad \textbf{(4.4)}$$

The surface coverage of the underpotentially deposited metal adatoms is denoted with θ. The Gibbs free energy change in the monolayer formation in equation *(4.1)* can now be written as follows.

$$\Delta G_{ML} = W_{M^{n+}} + \Delta G_{e^-}^{S} + \Delta G^0 + \theta(\Delta G_{desor}^{S} + \Delta G_{S-M}^{inter}) \quad \textbf{(4.5)}$$

During the process of adsorption, the solvated metal ions diffuse from the outer Helmholtz plane (OHP) into the inner Helmholtz plane (IHP) and lose their solvent shell. This process is then followed by the diffusion of unsolvated metal ions to the reaction zone and the subsequent formation of a (sub)monolayer. The total work of transfer of the solvated ions $W_{M^{n+}}$ can be given as:

$$W_{M^{n+}} = F\chi_{M^{n+}} + {}^{\Delta G_{desolv}}/_{S_N} \quad \textbf{(4.6)}$$

The surface potential of the ions, $\chi_{M^{n+}}$ determines the energy barrier, which the ions have to overcome to lose the solvation shell. S_N represents the number of solvent molecules, which are removed in the IHP and thus reduce the desolvation energy of M^{n+} ions.

The free energy change of the electron transfer from the electrode surface to the metal ions $\Delta G_{e^-}^{S}$ depends on the work function of the substrate, which is the minimum work or energy required to withdraw an electron from the electrode surface. Equation *(4.5)* shows the relationship between $\Delta G_{e^-}^{S}$ and the electrochemical potential $\mu_S^{el(inter)}$ of the electrode surface S in contact with the liquid phase or the electrochemical interface between surface and solution.

$$\Delta G_{e^-}^{S} = nF\mu_S^{el(inter)} \tag{4.7}$$

The electrochemical potential at of the electrode surface atoms is not as strong as the potential in the bulk. It is presumed that the $\mu_S^{el(inter)}$ can be determined as following:

$$\mu_S^{el(inter)} = {\mu_S^{el}}/{CN_S} \tag{4.8}$$

CN_S represents the coordination number of the substrate. The higher the coordination number, the lower the electrical and chemical forces the metal ions are exposed to at the surface. The electrochemical potential of the substrate can further be split into the chemical potential μ_S and surface potential χ_S of the substrate.

$$\mu_S^{el} = \mu_S + \chi_S \tag{4.9}$$

Further the chemical potential μ_S can be expressed with the work function of the substrate Φ_S:

$$\mu_S = -\Phi_S - \chi_S \tag{4.10}$$

Equation *(4.8)* and *(4.7)* now become:

$$\mu_S^{el(inter)} = {-\Phi_S}/{CN_S} \tag{4.11}$$

$$\Delta G_{e^-}^{S} = {-nF\Phi_S}/{CN_S} \tag{4.12}$$

For the deposition to proceed, solvent dipoles need to desorb from the substrate surface. The Gibbs free energy change for desorption of water dipoles $\Delta G_{\text{desor}}^{S}$ is a function of the surface charge densities and can be calculated as:

$$\Delta G_{\text{desor}}^{S} = {\Delta G_{S-H_2O}}/{a} \tag{4.13}$$

For *sp* metals, the water molecules adsorb via the oxygen atoms as the surface of the substrate is positively charged. In this case a becomes unity. For d metals and thereby a negative surface charge, the solvent adsorb via any of the hydrogen atoms

and a has the value 2. Based on known hydrogen-metal bond enthalpies in tabular compilations equation *(4.13)* can be written:

$$\textbf{for sp metals: } \Delta G_{s-H_2O} = \Delta H_{s-H_2O} - T\Delta S_{s-H_2O} \quad \textbf{(4.14)}$$

$$\textbf{for d metals: } \Delta G_{s-H_2O} = (\Delta H_{s-H_2O} - T\Delta S_{s-H_2O})/_2 \quad \textbf{(4.15)}$$

The substrate metal bond formation at the interface can occur with any of the coordinated substrate metal atoms. Thus, the Gibbs free energy change ΔG_{S-M}^{inter} is:

$$\Delta G_{S-M}^{inter} = {}^{\Delta G_{S-M}}/_{CN_S} \quad \textbf{(4.16)}$$

Further,

$$\Delta G_{S-M}^{inter} = {}^{\Delta H_{S-M}}/_{CN_S} \quad \textbf{(4.17)}$$

as the term $T\Delta S_{S-M}$ is known to be 10 % of the ΔH_{S-M} term.[79]

Another way of obtaining the enthalpy of bond formation is to draw on the dissociation energy of the bond between substrate and metal DE_{S-M} according to Pauling:[80]

$$DE_{S-M} = (DE_{S-S} + DE_{M-M})/_2 + 23(\chi_S - \chi_M)^2 \quad \textbf{(4.18)}$$

where χ_S and χ_M are the electronegativities of the substrate and metal in Pauling's scale.[80]

Finally, equation *(4.5)* can be substituted by equations *(4.6) (4.12)*, *(4.15)* and *(4.17)*.

$$\Delta G_{ML} = {}^{\Delta G_{desolv}}/_{S_N} + F\chi_{M^{n+}} - {}^{nF\Phi_S}/_{CN_S} + \Delta G^0 + \theta\Delta G_{s-H_2O} + {}^{\theta\Delta H_{S-M}}/_{CN_S} \quad \textbf{(4.19)}$$

Taking the relationship between the Gibbs free energy of the reaction and the deposition potential it follows:

$$E_{ML} = {}^{-\Delta G_{desolv}}/_{(nFS_N)} + {}^{\chi_{M^{n+}}}/_n + {}^{\Phi_S}/_{CN_S} + E^0 - {}^{\theta\Delta G_{s-H_2O}}/_{(nF)} - {}^{\theta\Delta H_{S-M}}/_{(nFCN_S)} \quad \textbf{(4.20)}$$

The number of electrons needed to reduce M^{n+} will be substituted by the partial charge on the adsorbate z_{ad}.

$$E_{ML} = {}^{-\Delta G_{desolv}}/_{(z_{ad}FS_N)} + {}^{\chi_{M^{n+}}}/_{z_{ad}} + {}^{\Phi_S}/_{CN_S} + E^0 \\ - {}^{\theta\Delta G_{S-H_2O}}/_{(z_{ad}F)} - {}^{\theta\Delta H_{S-M}}/_{(z_{ad}FCN_S)} \quad \textbf{(4.21)}$$

For simplicity equation *(4.21)* may be written as:

$$E_{ML} = A + B\theta \quad \textbf{(4.22)}$$

Equation *(4.22)* expresses a linear dependency between E_{ML} and θ. The intercept A depends, among other things, on the work function of the substrate. The slope, however, is a function of the desorption energies of the solvent molecules from the substrate and the enthalpy of the metal substrate bond formation.

4.2 Single Crystals as Model Catalysts

The revolution in the field of cleaning of single crystal surfaces by means of advanced preparation procedures and the need to simplify complex electrocatalytic material systems have led to numerous researches of the desired electrocatalytic reaction on single crystal surface electrodes.

4.2.1 Crystallography of Single Crystals

The dependence of chemical and physical properties on crystal structure and generally on the arrangement of atoms in a catalyst system elucidates the long history of crystallography. The atoms in a crystal absent of defects and localized mistakes are arranged in an identical order in each direction. Each crystal is built up of infinitesimally small identical morphological unit cells characterized by three axial vectors a, b and c. The unit cell is not unique and can be further defined by the numerical values of the edges and the angles between them, termed as the lattice parameters. There are 14 possible three-dimensional configurations to arrange the lattice points such as simple cubic, face-centered cubic, hexagonal and body-centered orthorhombic to name just a few. These so-called Bravais lattices can be deduced from seven crystal systems, which provide all possible arrangements of axes and angles to describe the external form of crystals.[81]

Table 1| Lattice parameter relationship for the seven crystal systems.

Crystal System	*Axial Relationship*	*Interaxi Angles Relationship*
Cubic	$a = b = c$	$\alpha = \beta = \gamma = 90\,°$
Tetragonal	$a = b \neq c$	$\alpha = \beta = \gamma = 90\,°$
Orthorhombic	$a \neq b \neq c$	$\alpha = \beta = \gamma = 90\,°$
Rhombohedral	$a = b = c$	$\alpha = \beta = \gamma \neq 90\,°$
Hexagonal	$a = b \neq c$	$\alpha = \beta = 90\,°, \gamma = 120\,°$
Monoclinic	$a \neq b \neq c$	$\alpha = \gamma \neq 90\,° = \beta$
Triclinic	$a \neq b \neq c$	$\alpha \neq \beta \neq \gamma \neq 90°$

The position of atoms in the unit cell as an additional characteristic of the crystal structure is defined as fractions of the unit cell edges a, b and c and can be given by a vector r as defined in equation

$$r = xa + yb + zc \qquad \textbf{(4.23)}$$

The rate at which the unit cells are stacked in different directions determines the formation of different facets. The orientation of these faces is denoted with respect to the crystal axes by means of three integers (h, k, l), called Miller indices.[82] They represent the reciprocal intercepts of the respective plane with the main crystallographic axes. The result is enclosed in parentheses. Parallel planes exhibit the same Miller indices, as per definition only small integral digits are used. The individual steps of how to find the Miller indices are exemplarily displayed in Table 2 for the crystallographic (110) plane.

Table 2| Determination of crystallographic plane exemplarily shown for the Miller indices (110).

	a	***b***	***c***
1. intercept	1	1	∞
2. reciprocals	1/1 1	1/1 1	1/∞ 0
3. reduction	1	1	0

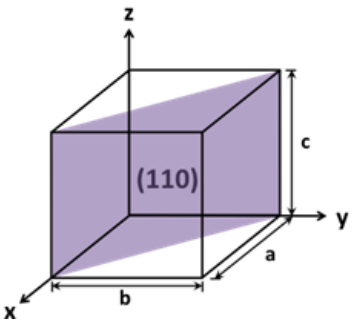

The face-centered cubic (fcc) lattice, in which Ir crystallizes, is one of the three Bravais lattices of the cubic crystal system. It represents the simple unit in a cubic

closest-packed structure in which each bulk atom is surrounded by 12 nearest neighbors. The optimal packing density for the atoms is characterized by hexagonally close-packed spheres stacked on each other with the second layer covering half of the triangular gaps formed in the layer below. In the third layer the spheres are rotated 180° relative to the second layer covering the other half of the voids of the first layer. In Figure 12 the ABC stacking pattern together with the unit cell of the fcc crystal are shown.

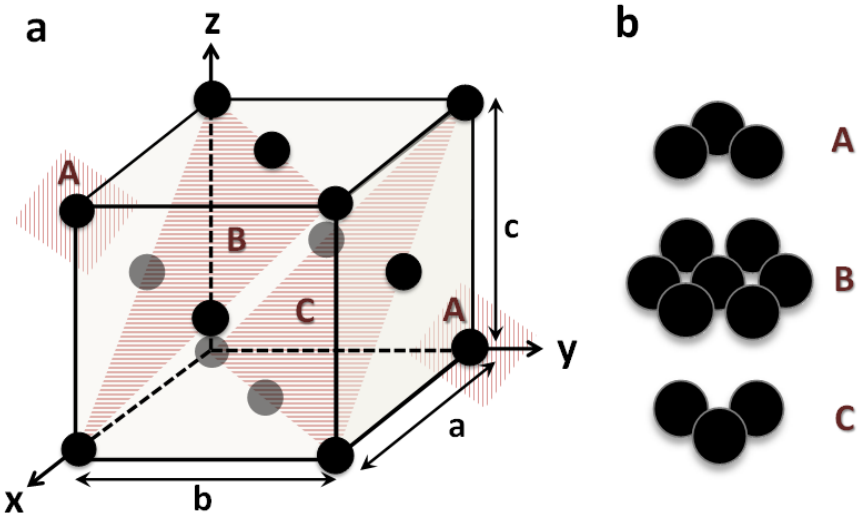

Figure 12| (a) Closed packed atomic arrangement in a face-centered cubic unit cell displaying the octahedral planes tilted relative to the crystal axes. These planes are stack in a sequence ABC as shown in (b).

Figure 13 displays the hexagonal atomic arrangement at the surface of the (111) face. The (111) plane along with the (100) and (110) planes are determined as the three atomically flat low-index planes of fcc crystals. Of all surfaces the (111) plane reveals the highest atom packing density (9 nearest neighbors for each surface atom) and thereby the lowest surface energy and less reactive then the surface atoms of the (100) and (110) (8 and 6 nearest neighbors for each surface atom, respectively) plane.

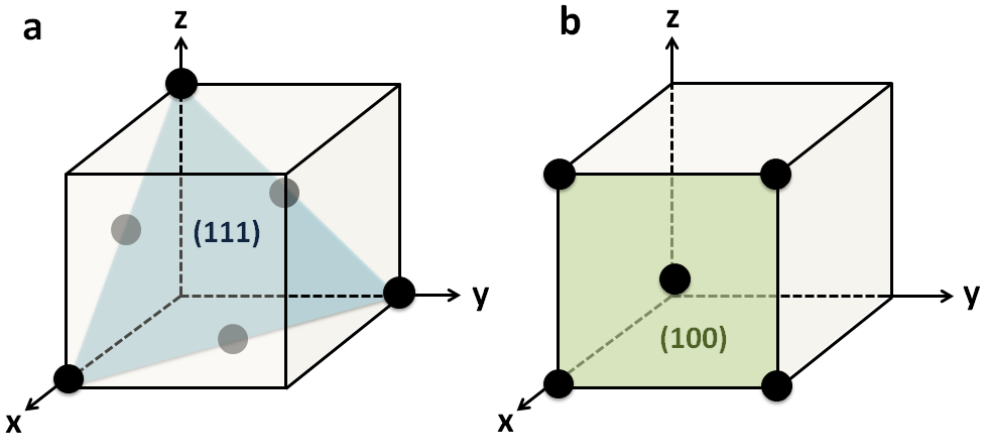

Figure 13| Crystallographic planes of the (a) (111) face and (b) (100) face in a face-centered cubic (fcc) unit cell.

The second kind of Miller indices designates the crystallographic direction in a lattice and is defined as the distance that the vector traverses. In a cubic crystal, the vector perpendicular to the (hkl) plane is termed as its surface normal $[hkl]$ and can be calculated as the cross product of the vectors lying within the plane.

$$[hkl] = [ijk]\ x\ [lmn] \qquad \textbf{(4.24)}$$

Ideally, single crystals exhibit no defects or dislocations. However, due to technical limitations in cutting and polishing, the crystal surface might reveal small misorientation angles from the low-index plane. These stepped or vicinal surfaces exhibit defects such as adatoms, islands and vacancies and are characterized by atomically flat terraces of a certain width separated by monoatomic high steps (see Figure 14). A poly crystal on the other hand consists of numerous crystallites, which are randomly oriented. In a poly crystalline material the orientation of these crystallites differ and possibly exhibit different symmetries.

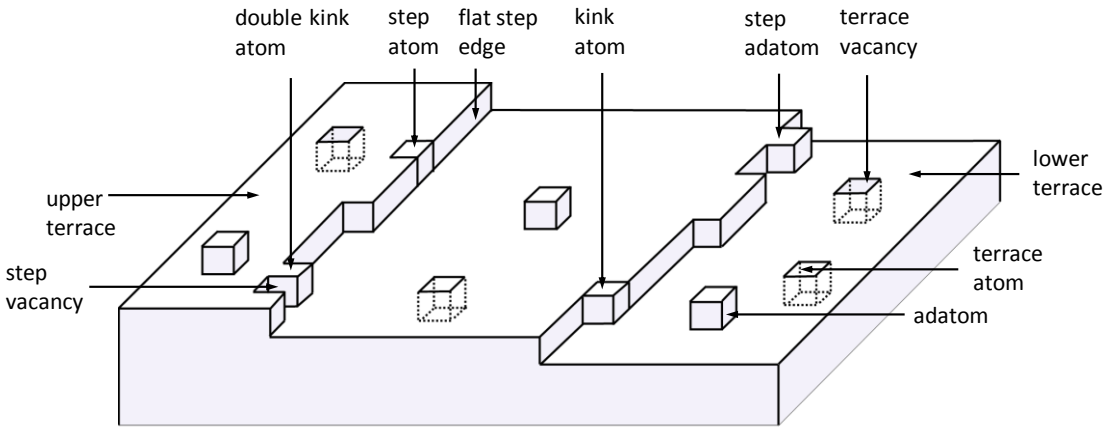

Figure 14| Schematic illustration of defects on a cubic crystalline surface.

Instead of using the Miller indices to describe the geometric structure of these stepped surfaces, it is more appropriate to apply the Lang, Joyner, and Somorjai (LJS) nomenclature[83] in the form

$$M(S)[n\ (h_t k_t l_t)\ x\ (h_s k_s l_s)] \qquad \textbf{(4.25)}$$

where M is the symbol of the metal, S represents the stepped surface, $(h_t k_t l_t)$ and $(h_s k_s l_s)$ are the Miller indices of the terrace plane and step plane, respectively and n gives the number of atoms in the terrace.

In the next chapter, the motivations behind working with single crystalline surface and well-defined thin-films as model catalysts are presented. The inclusion of theses model systems helps in better understanding of the performance of electrocatalyst and most importantly facilitate the production and synthesis of industrial real-world catalysts.

4.2.2 Single Crystals and Well-Defined Thin-Films as Model Catalyst

Technological progress in electrochemical energy conversion is mostly achieved by advances in electrocatalysis, in particular the design and synthesis of new electrocatalytic materials. However, scientific advances in the field of electrocatalysis are not exclusively limited to the development of novel catalytic systems; the study is completed when electron and ion transfer reactions are understood and the microscopic processes at the electrode surface can be elucidated. Important determinants affecting the rate of electrocatalytic reactions is the product of a complex interplay of various elements including crystallographic orientation, size and shape of the produced nanoparticulate materials and most likely defects and misorientations present on the surface. To uncover the electrochemical behavior of heterogeneous electrocatalysts, which are often complex in structure, a key role in electrochemical research is the introduction of model experiments with well-defined and distinct surfaces. The correlation between orientation and electrochemical reactivity can be established with single crystal studies.

The significant role of single crystalline surfaces in pursuing progress in solid-state science has led to a considerably effort in the development of growth techniques. The science of crystal growth reaches back into the end of the 18th century until the 1920s and has experienced a renaissance in the 1970s. The subject of single crystal studies remains dynamic; their application in the optical technology

as hosts for solid-state lasers or their utilization as substrates for the growth of superconductor films, to name just a few, reflect their rising importance in the solid-state research. The different methods include the growth from solution (both high and low temperature), growth from vapor, crystal growth in gels and growth methods from melt. Depending on the properties of the desired material (suitable solvent, melting ability of solid) the most appropriate method to match the challenge will be selected. The Bridgman and Czochralski methods[84] are the most important growth procedures to produce bulk crystals from melt. The latter is suitable for the preparation of large cylindrical single crystals using a levitating melt.[85] In this crucible-free method, an in-situ analyzation of the growth procedure is feasible. In the inexpensive Bridgman method (also known as Bridgman-Stockbarger method), the crystal is grown by direct solidification of a melt in a crucible by increasing the temperature of the furnace gradually.[86]

Clavilier developed a major contribution to the final preparation of well-ordered and structured surfaces with his competitive flame annealing and quenching method suitable for small electrodes of about 3 mm in diameter. This approach has been employed for several decades in which the electrode is quenched in milli-q water instantly after annealing and then transported to the electrochemical cell.[87] A well-established but rather expensive construction that incorporates cleansing of single crystal surfaces with detailed surface characterization is the ultrahigh vacuum (UHV) chamber, in which uniform and ordered surfaces are prepared by Ar-ion bombardment and high-temperature annealing.[88, 89] In the beginning, structure-sensitive UHV techniques were limited to low energy electron diffraction (LEED) and Auger spectroscopy to assess the quality and cleanliness of the surfaces. For a detailed analysis of the surface topography, the techniques have been extended to, inter alia, reflexion high energy electron diffraction (RHEED)[90] and scanning tunneling microscopy (STM).[91]

A successful and economical cell system established by Bondarenko *et al.*[92] combines the advantages of flame annealing with subsequent electrochemical studies in a closed glass setup. Through this unique cell design the availability and practicability of single crystals studies can be substantially increased to more laboratories allowing the investigation of relevant electrocatalytic reactions on a variety of single crystal surfaces.

The need of simplified model systems including well-defined thin films and the increasing importance of single crystal studies lie in the complexity of real-world

electrocatalysts, which are typically produced as nanoparticles. The structural effects dictating the catalytic properties of the active site are a complex combination of exposed facets, defects, size and shape of the nanoparticle and its synergy with the support.[56] This complicated system needs to be reduced by means of simplified model catalysts in order to detect the surface site which is determining the activity. These observations and activity trends can then be employed in the synthesis and design of efficient electrocatalysts. In addition to the structural effects, the electronic character of the active sites plays a crucial role in the activity, selectivity and stability trend in heterogeneous electrocatalysis. Based on the Sabatier principle[54], the binding energy of the active site, which is affected by the electronic structure of the surface can be tuned and optimized by introducing a second metal into the surface or subsurface atomic layer. The difficulty is that a fundamental understanding is required to forecast which impact a specific species on a certain position has. With that knowledge the electronic properties of a given surface can be altered by selective electrochemical deposition of monolayer and sub-monolayer amounts of metals using the electrodeposition process. This approach can be further extended to the preparation of surface alloys (SA) and near-surface alloys (NSA) by applying a controlled thermal treatment of the overlayer system to precisely position the solute element. The electrochemical design of model surfaces is a suitable means to optimize existing electrocatalysts whose binding energies are close to the activity optimum.

Chapter 5 Design, Set-up and Validation of an Inductive Annealing and Electrochemical Cell for (Single) Crystal Electrodes

This chapter is predominantly based on the following publication:

E. Özer, B. Paul, C. Spöri, P. Strasser, *Small Methods* **2018**, 1800232 (DOI: https://doi.org/10.1002/smtd.201800232).

The following chapter will present the novel versatile multifunctional electrochemical single crystal preparation and test station. The test station features capabilities for controllable thermal annealing for the purposes of restructuring and healing of any type of smooth extended metallic or oxidic crystal surfaces, in particular single crystals. The presented setup enables rapid inductive heating of the crystal electrodes to temperatures as high as 1900 °C under precise infrared temperature control in controlled gas atmospheres. The constant overpressure (with respect to the laboratory atmosphere) inside the cell prevents the laboratory atmosphere to permeate the cell and contaminate the single crystal station. The fine adjustment of the sensors affords accurate and instant information on the temperature of the electrodes' surface. The subsequent cooling process of the electrodes is carried out in Ar atmosphere without any treatment in water. After annealing, the crystals can immediately be subjected to any type of electrochemical deposition, modification, or characterization in two distinct three-electrode chambers without any exposure to air. Both chambers are incorporated into the test station and feature pump-controlled supply and withdrawal of liquid electrolyte. A special feature of this setup is the inert-gas flow inversion capability, which enables the transfer of the crystal electrodes into a separate portable inert-gas chamber designed for transport of crystal electrodes. Design details of the setup are presented and its functionality during thermal preparation and electrochemical voltammetry of Ir single crystal catalysts for the oxygen evolution reaction (OER) is demonstrated. The presented test station is designed to provide a crystal handling

environment superior to the classic flame annealing approaches, yet to constitute a cost-effective alternative to costly vacuum chambers.

The design of the cell and its unique features will be the subject of this section. In addition, the validation of this setup was implemented through single crystal and polycrystal measurements. Further surface modifications were conducted demonstrating the successful high-temperature annealing and electrocatalyst design.

5.1 Implementation of Modern Surface Science

Advancements of accurate surface analytical techniques encouraged the breakthrough in the field of modern surface science and enabled the study of alluring surface phenomena since the early 1960s. Well-defined and clean adsorbate-free and adsorbate-covered crystal surfaces respectively form the basis to determine and investigate fundamental aspects in modern electrocatalysis.

Surface studies by means of single crystal electrodes have undergone significant development in the establishment of model system that can give insight into the rather complex behavior of nanoparticulate materials. The emphasis put on fundamental electrocatalysis research results from the ambition to untangle the various parameters controlling the catalytic properties. The (surface) composition and the presence of various facets and defects are a few to mention.[56, 57] The comprehensive observation of activity and stability trends in electrocatalytic reactions that has been gleaned from studying well-defined surfaces can then be translated into the development and synthesis of efficient, real-world electrocatalysts applied in energy conversion processes.

The underlying concept of generic model system studies is ordered and uniform single crystal surface structures free from impurities.[93, 94] High-priced ultrahigh vacuum (UHV) techniques are widespread in the study and preparation of clean and well-ordered single crystals surfaces. This well-established method uses Ar-ion bombardment and high-temperature annealing in combination with surface science techniques, e.g. LEED, AES and XPS.[88, 89] While the atmospheric control is more sophisticated in UHV chambers than in the presented design, the former lack of accessible application. Their utilization and mainly the transport of electrodes between electrochemical cells and surface analysis section (LEED, XPS) is rather time-consuming and complex. The flame annealing and quenching method represent a more economical and sufficient approach and has been applied for

several decades. Here, the cleaned electrode surface is quenched in milli-q water instantly after annealing and transported to the electrochemical cell.[87] However, the protection of the surface with a drop of water is limited to small electrodes with a diameter of < 3 mm. Thus, it would be beneficial to combine the advantages of flame annealing[95] with subsequent electrochemical studies in a closed setup to ensure reproducibility and to prevent contamination of the surfaces. Furthermore, this would allow studying larger single crystals with an economical cell setup and would spread the availability of single crystal studies to more laboratories.

The modification of surfaces by underpotential deposition (UPD)[96-98] of (sub)monolayer amounts of foreign metal atoms opens the way to a variety of applications including the optimization of electronic structure of the active sites. This approach may be further extended to the preparation of surface alloys (SA) and near-surface alloys (NSA) under controlled annealing conditions.[99-101] Besides the conventional approach in an UHV chamber, an inductive electrochemical single crystal chamber can give access to these surface modifications. In such a cell, the preparation and characterization of single crystal surfaces allows electrochemical surface design without exposing the electrodes to the laboratory environment.

A cell design meeting some of the challenges above was reported by Bondarenko *et al.*[92] consisting of an inductive section and one three-electrode electrochemical section. This initial design was improved significantly by i) including a second electrochemical cell, ii) automated electrolyte dispensing and removal, iii) accurate automated infrared temperature control during inductive annealing, and iv) inert-gas flow conversion and crystal electrode transfer capabilities. Both electrochemical cells can be filled and emptied with electrolyte completely independently thanks to four separate purging electrolyte reservoirs. Here, the new test station is presented and its functionality demonstrated using electrochemical measurements on Pt(111) and Ir(111) single crystals and a polycrystalline Ir electrode, evidencing the successful high-temperature annealing and surface modification. Any types of electrodes can be employed and heated by means of induction, as long as they exhibit sufficient critical mass and couple into the electric field. The wide accessible temperature range controlled by sensitive IR and the resulting precise control of the surface temperature is what sets this set up apart from all earlier designs. Given its cost-effectiveness, this electrochemical test station is an affordable alternative to costly vacuum techniques and conventional flame annealing approaches.

5.2 General Cell Design

A detailed sketch of the custom-made inductive electrochemical single crystal setup with its two compartments is displayed in Figure 15. The compartment at the bottom of the cell (marked in pink) is referred to as the electrochemical chamber and is equivalent to a typical three-electrode glass cell. The setup in our previous work[102] was extended with a Luggin capillary at the bottom chamber to enable clean and straightforward electrochemical measurements in a protective environment. With the use of two mass flow controllers (MFCs) the atmosphere inside the cell can be adjusted to N_2, Ar, H_2, CO and any desired mixture thereof. The installation of a 4-way valve at the gas inlet port atop the electrochemical section allows not only for the electrolyte to be degassed with argon but also an air-free transport of the electrodes out of the cell. The transport of single crystal electrodes in the transfer chamber is described in detail in Figure 19a-e.

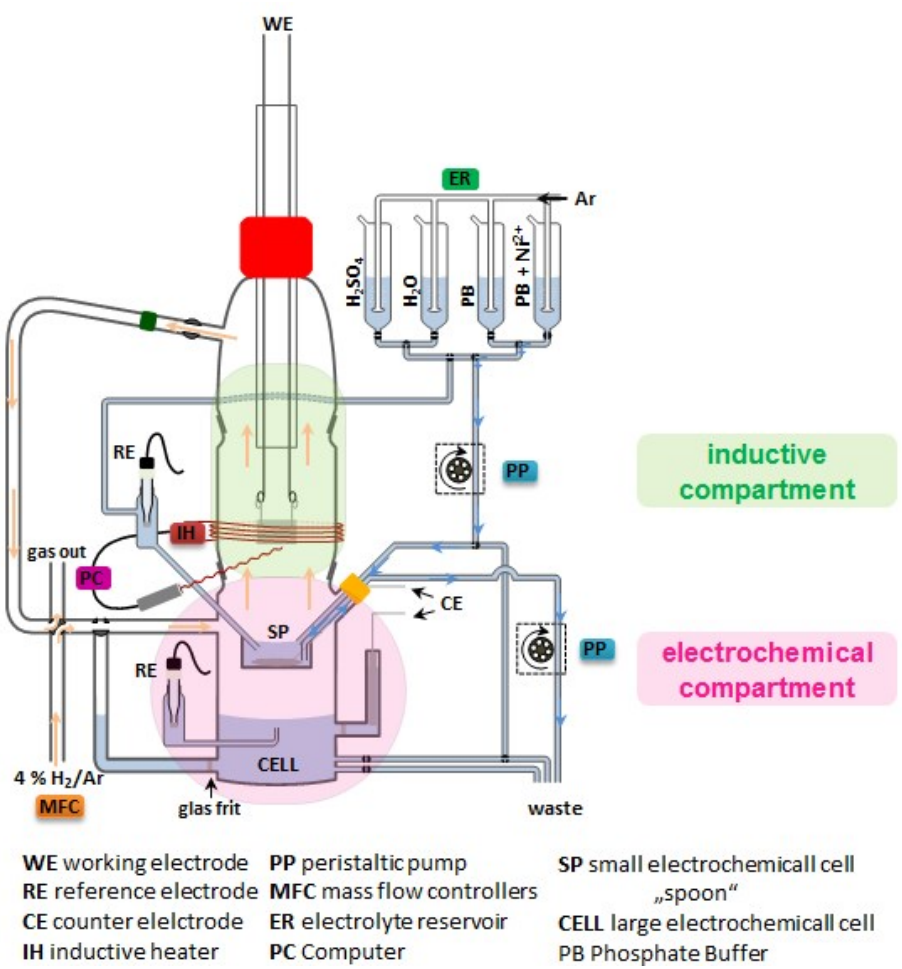

Figure 15 | Detailed sketch of the final version of the inductive electrochemical single crystal chamber (left) and photograph of the cell (right). The arrows drawn represent the gas flow of annealing and preparation of single crystal surfaces, respectively. Explanations concerning abbreviations are given below the cell.

The preparation of reproducibly well-ordered noble metal single crystal surfaces is a fundamental basis for all electrochemical investigations on these facets. To this end, thermal treatment of a single crystal working electrode takes place in the second (inductive) compartment, until well-defined, atomically flat surfaces are obtained (confirmed by CV). Hereto, the working electrode can be positioned in the center of a quartz tube, which in turn is placed amid the inductive coil of an inductive heater. The lid of the inductive compartment is equipped with a gas outlet port. The cylinders are mounted with iridium wires, which are attached to four tungsten rods via iridium loops. The tungsten rods are placed in a glass tube, forming the working electrode mount, which is introduced to the cell via a GL (glass thread) fitting on the lid. A detailed description of the electrode mount is presented in Figure 20.

In the following chapters, a detailed description of the individual components and elements of the setup will be presented.

5.2.1 Inductively Coupled Annealing

An automatic heating system controller. (OvenControl, lab-control, Berlin, Germany) is connected to two IR pyrometers (PyroUSB 2.2 series infrared sensor, Calex Electronics Limited, temperature range $T_1 = 250 – 1000$ °C and $T_2 = 450 – 2000$ °C) which need to be positioned manually prior to each heating protocol to accurately monitor the temperature of the crystal. In Figure 16, a close-up picture of the back of the IR pyrometers is given showing the screws that enable a very fine adjustment. Via a tactile contact, the inductive oven is automatically regulated through the temperature controller to a pre-set temperature and time. The heating protocol, defined by target temperature, holding time and cooling phase, runs automatically and enables accurate and reproducible heating cycles. The combination of automated control, IR temperature measurement and the iridium-tungsten electrode mount allows for annealing of single or poly crystalline electrodes at much higher temperatures than accessible through any direct contact thermocouple. Avoiding the direct contact also avoids any sintering between thermocouple and working electrode.

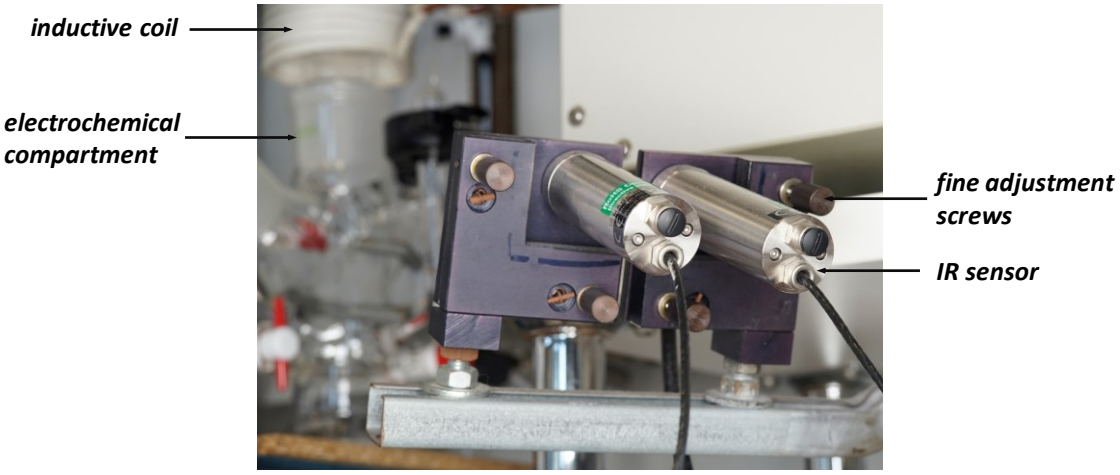

Figure 16| Close-up of the two IR pyrometers, which can be oriented towards the surface of the cylinder amid the inductive coil with very fine adjustment screws. The electrochemical compartment of the setup is visible.

The heating system controller is equipped with two modes of operation. In the 'adjust modus', the single crystal is heated up manually via a pedal at a heating current of approximately 80 % (I_{heat} = 940 - 950 A) until both sensors display a temperature in the range of 600 and 700 °C. After setting the toggle switch at the inductive oven from 'Manual' to 'Automatic', the 'Start' button at the oven is pressed. During the automated heating process managed by the inductive oven, the OvenControl is still in the 'adjust modus' allowing for an alignment of the IR sensors until both feature the same temperature. Each individual sensor is positioned in x- and y-direction by two sensitive screws until a maximum temperature is obtained. Figure 17 explains the principle.

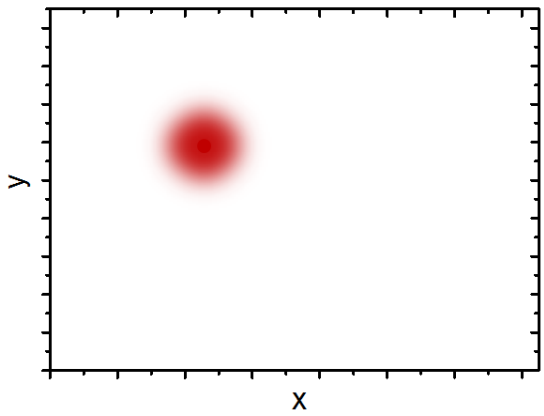

Figure 17| Diagrammatic drawing showing the principle of the fine adjustment of the IR pyrometers towards the crystal. Continue turning the screws until the maximum temperature is displayed in both directions. The dark red spot in the middle represents the highest temperature and hence the real temperature of the cylinder's surface.

In order to guarantee a secure application, a fault detection is enabled in the 'normal modus'. During the heating process, an acoustic and visual alarm is triggered once the target temperature is not reached or the temperature difference between both sensors exceeds a predefined value. Here, the button 'Alarm Reset' needs to be pressed once to mute the acoustic sound and twice to delete the alarm message. The source of the malfunction is most probably a misalignment of the sensors and must be eliminated accordingly.

5.2.2 The 'Spoon'

The smaller electrochemical cell, referred to as the "spoon" (see Figure 18a), is a small-scale three-electrode setup allows for additional 'dirty' electrochemical measurements. A platinum wire runs through the spoon handle and ends at the ground of the spoon to serve as the counter electrode. A small piece of platinum mesh is tack-welded to the wire to guarantee a large enough surface area. An additional Luggin-Haber reference electrode capillary for measurements inside the spoon is mounted on a retractable inlet allowing access to measurements in the bottom compartment when not in use. Through the electrolyte inlet and outlet channels in the spoon handle, the electrolyte liquid in the spoon cell can be dosed and removed at will without contamination of the bottom electrochemical compartment and without exposure to ambient air atmosphere. A two-channel hydraulic pump controls the electrolyte flow automatically. The purposes of the spoon cell is not limited to electrochemical measurements, such as deposition of overlayers (OL) electrodeposition but also to mechanically clean the electrodes with milli-q water. A novel and quite important feature of the overall test station is the continuing electrolyte stream through the spoon cell, which simplifies the cleaning process. Without removing the crystal electrode from the spoon cell, the milli-q water flow removes any adhering impurities prior to heat treatments as well as after each electrochemical measurement.

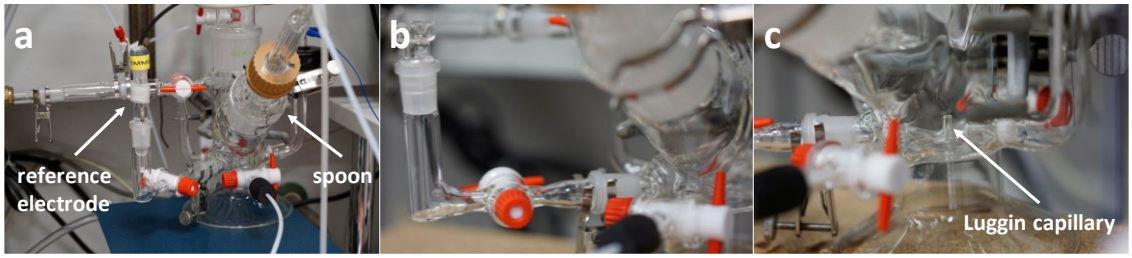

Figure 18| Electrochemical compartment at the bottom displaying (a) the three-electrode setup with the reference electrode/Luggin capillary and the counter electrode with (b, c) close-ups of the Luggin capillary.

5.2.3 Electrolyte Reservoirs

The presented test station setup is completed by four individual electrolyte reservoirs, which allow up to four different degassed electrolytes to be inserted into the electrochemical compartment at the bottom or into the spoon cell, thereby offering large flexibility to the user. These reservoirs are connected to the electrochemical compartment, the spoon and the adjustable Luggin capillary via a pipe system. The electrolyte storage containers are constantly purged by Ar gas individually allowing for an air free replacement of electrolytes between measurements.

5.2.4 Crystal Transfer

A 4-way valve further enhances the overall inductive electrochemical test station. The valve allows for a flow direction inversion when the crystal electrodes are to be transferred to an external location, like a synchrotron. The installation of the valve is given in Figure A1 in the Appendix

Figure 19 displays the detailed procedure of the Ar-blanketed transfer of a crystal electrode to a portable glove box, inside which the electrode is placed under argon for additional transport. During annealing and electrochemical operation, the gas flow conditions are controlled as shown in Figure 19a. Gas flow direction from bottom to top serves to maintain a clean electrochemical compartment, as all removed impurities from the crystal surface leave the test station through the lid at the top into the waste. To ensure a safe transport, the electrodes are first pulled upward into the top part of the cell. Thereafter, the gas flow direction inside the station is inverted, and then the top lid of the station is lifted and separated from the bottom of the station (see Figure 19b). The larger mass of Ar compared to air prevents the crystal electrode surface to come in contact with the ambient

atmosphere. As shown in Figure 19c the lid is then positioned on top of a transport vessel, which is subsequently deaerated before both parts are attached to each other (Figure 19d). After flushing for several minutes more, both valves are closed, and the lid of the cell can be separated from the Ar line.

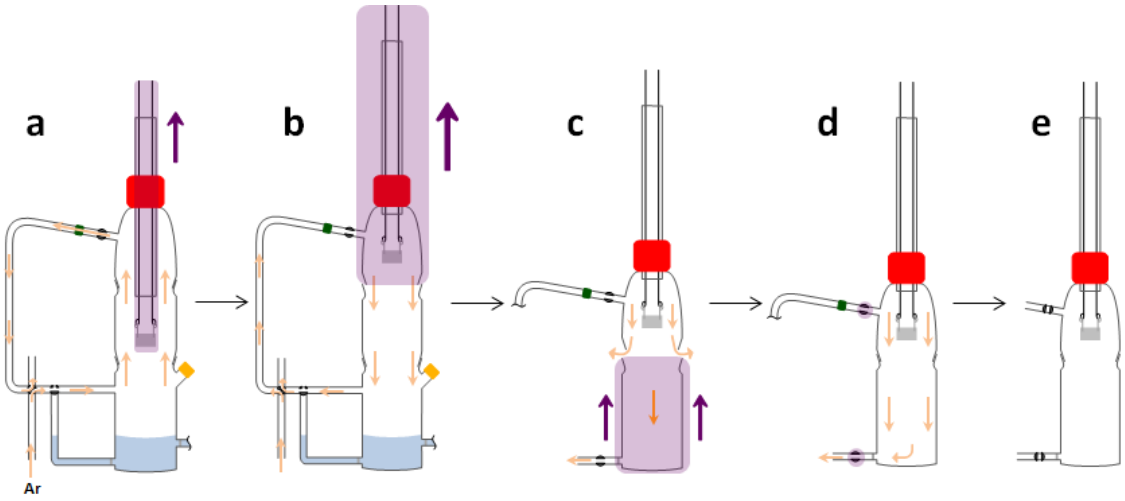

Figure 19| Schematic representation of air-free removal and transport of the electrode in an Ar flooded transport vessel. (a) The cylinder is pulled up into the top part of cell and the gas flow is reserved. (b) The lid is separated from the cell and (c) positioned on top of the transport vessel to reduce its oxygen amount. (d) After attaching both parts together and purging the transport vessel for several minutes, (e) both valves can be closed.

5.2.5 Mounting of Crystal Electrodes

The detailed steps involving the mounting of a single crystal electrode are presented in Figure 20. In order to increase stability and reliability, the mount is constructed of four tungsten rods (Ø= 1.60 mm) which are rolled up at one end (i). The inside of the open O-shaped ends is coated with iridium (ii) to ensure electronic contact to the electrode. The cylinder is then suspended on four iridium hooks (iii) as shown step by step in Figure 20a-d.

Figure 20| Custom-made mounting of single crystal electrodes for heating and electrochemical measurements in the inductive electrochemical chamber. The mounting consists of (i) four tungsten rods (ii) welded with iridium and (iii) four attached iridium hooks, which hold the cylinder.

5.3 Detailed Description of Experimental Procedures

Preparations prior to experimentation, crystal annealing, and electrochemical procedures in spoon and electrochemistry in the large bottom cell

Before the single crystal electrodes were mounted into the setup, the glassware was cleaned thoroughly in a solution of 95 % H_2SO_4 and an oxidizer (NOCHROMIX®, Sigma-Aldrich), followed by a bath in 0.1 M HNO_3 and repeated rinsing with milli-q water. The spoon, however, was rinsed with 37 % HCl due to the integrated Pt wire.

Two types of verification measurements were applied to test the cell. In a first step, electrochemical measurements of a Pt(111) single crystal surface were performed in both electrochemical compartments to confirm the principle operation of the cell setup. Afterwards, the second verification measurement proves the application to higher annealing temperatures by preparation of an Ir(111) single crystal as well as Ni overlayer and (near-) surface alloy formation by annealing a polycrystalline Ir electrode.

For the first experiment, a Pt(111) single crystal electrode with a diameter of 10 mm and a precision of orientation of ≤ 0.1° (MaTecK GmbH, Jülich) was used. For mounting, two continuous lateral holes with a diameter of 0.5 mm were machined into the shell surface through which loops made of Ir wire (Alfa Aesar,

Ø = 0.25 mm, 99.9 %) run. A saturated mercury/mercury sulfate (MMS) reference electrode was applied and calibrated frequently against a reversible hydrogen electrode (RHE) in the same electrolyte at room temperature. Before the Pt(111) single crystal was heated in the inductive compartment, a cyclic voltammogram of its surface was recorded in the bottom compartment. After annealing at 800 °C in Ar atmosphere (purity 5N, 99.999 %) for 2 min, the surface of the electrode was characterized in the spoon cell.

In experiment 2, the single crystalline Ir measurements were done as described elsewhere.[102] The final refinement of Ir(111) electrode was performed in 4 % H_2/Ar atmosphere. Hereto, a heating protocol consisting of several heating cycles per heating phase was applied in which the changes of the surface was monitored in between. In each heating cycle the crystal was heated for 2 min at 1900 °C with a heating current of 80 % (I_{heat} = 940 – 950 A) and subsequently cooled down for 5 min. A heating phase was followed by a characterization CV in the electrochemical chamber at the bottom between the potential limits of 0.05 and 0.8 V_{RHE}. These verification measurements were performed in 0.05 M H_2SO_4 (diluted from 95 % H_2SO_4, Suprapure, Carl Roth). Ir(111) electrodes with a diameter of 10 mm and a precision of orientation of ≤ 0.1° (MaTecK GmbH, Jülich) were used.

For evaluation of the surface quality, the electrodes were immersed in the hanging meniscus configuration into the Ar-degassed electrolyte at the lower potential limit of 0.05 V_{RHE}. A cyclic voltammogram at a scan rate of 50 mV s^{-1} was then recorded. The upper turning potential for Pt was 1.2 V_{RHE} and 0.8 V_{RHE} for Ir.

The electrodeposition measurements were conducted with a polycrystalline Ir electrode (Ø = 10 mm, MaTecK GmbH, Jülich) grinded and polished in a half-automatic polishing machine (AutoMet 250, Buehler) to a mirror-like surface finish. For a detailed description of the polishing procedure see section 6.2.1.2. The deposition measurement to obtain an overlayer (OL) of Ni (Ni/Ir_{poly} OL) was performed in a rotating disk electrode setup (see section 6.2.2.1) in phosphate buffer solution of pH 6.85 (0.1 M KH_2PO_4, 0.1 M K_2HPO_4: 99.95% trace metals basis) containing 2 mM $NiSO_4$. The electrode was immersed at the deposition potential 0.05 V_{RHE} and held for 10 min. To produce a Ni/Ir_{poly} near surface alloy (NSA) the electrode was initially unmounted from the RDE setup and attached to the custom-made mounting by four tungsten wires as shown in Figure 20. Subsequently the cylinder was annealed in 4 % H_2/Ar at 400 °C for 2 min in the inductive setup. Both catalysts were then tested for OER activity in 0.1 M KOH in the RDE setup

after thorough rinsing with milli-q water. The samples were immersed in the hanging meniscus configuration at 1.0 V_{RHE} followed by a polarization curve into the OER potential region with 5 mV s^{-1} to an upper potential limit required to reach a current of 0.785 mA (current density of 1 mA cm^{-2}) in the respective scan.

The measured current is normalized to the geometric area of the electrodes to provide comparable current densities (jgeo). The geometric surface area of the electrodes is 0.785 cm^{-2} corresponding to the diameter of 10 mm. The electrolytes in the reservoirs were degassed with Ar for 15 min before they were introduced into the cell. All electrochemical measurements were performed by using a potentiostat (SP-240, BioLogic, France). During electrochemistry, the reference electrode was placed in a smallest distance as possible to the crystal surface via a Luggin capillary. The counter electrodes are manufactured from platinum wire and platinum wire mesh (Chempur GmbH, purity 99.99+%). These electrodes are characterized by a high surface area to ensure that the reactions taking place at the counter electrode are not rate determining. The atmosphere inside the custom-made setup was created by gases with a purity of 5N (AirLiquide, 99,999 %) and two Bronkhorst EL-Flow mass flow controllers (MFC). After mounting, the crystal electrodes are positioned centrally in the inductive coil and annealed automatically (see section 5.2.1) with an SP-25A induction heater (Desk-Top Induction Heater 30-80 kHz, 25 kW, EQ-SP-25A by MTI Corporation, USA). The induction heater is cooled by a recirculating cooler (Van-der-Heijden, 002-RB400 VP, $P_{cooling}$ = 1.0 kW, $\dot{V}$ = 4 l min^{-1} at p = 2.2 bar, $\dot{V}_{max}$ = 10 l min^{-1}, p_{max} = 3.5 bar). The Ar-degassed electrolytes from the installed electrolyte reservoirs are introduced into the electrochemical compartments by a two-channel hydraulic pump (Roth Cyclo II, 8 rolling).

5.4 Annealing and Voltammetry Validation

In order to verify the full functionality of this new test station, a Pt(111) cylinder was inserted as working electrode for both the larger electrochemical bottom compartment and the spoon cell. Initially, the cyclic voltammetry (CV) of the non well-defined Pt(111) was recorded in the bottom electrochemical compartment without any previous annealing procedure in order to demonstrate the effect of surface structure healing during thermal preparation. As expected, the CV (shown as the dotted line in Figure 21a displayed hardly any characteristic features of a well-ordered (111) facet of platinum except for a broad and undefined underpotentially deposited hydrogen (HUPD) region between 0.05 and 0.2 V_{RHE}. A dramatic change in the cyclic voltammetry of the Pt surface was observed after suitable thermal annealing at 800 °C for 2 min. Even after a short heating period, the spoon cell is fully sufficient to display characteristic electrochemical redox features of Pt and distinguish between chemically distinct adsorption sites. The voltammetry displays three typical regions of Pt(111)[103]: (i) the HUPD adsorption/desorption region at around 0.15 V_{RHE} with (ii) two shoulders at 0.25 and 0.3 V_{RHE} and (iii) a broad nondescript Pt oxidation region stretching from 0.85 to 1.2 V_{RHE}.

The cyclic voltammogram of a single crystalline Ir(111) surface during preparation phase is presented in Figure 21b. The initial voltammetry of the crystal surface is largely featureless and only displays the hydrogen underpotential deposition (HUPD) and the exchange of sulfate and hydrogen sulfate from the electrolyte with adsorbed hydrogen atoms at potentials around 0.1 V_{RHE}, respectively. With increasing number of heating cycles, the HUPD peak is shifted to more negative potentials implying a more cathodic desorption of atomic hydrogen from the Ir(111) surface.[102] The potential range between 0.5 and 0.8 V_{RHE} lacks any OH adsorption demonstrating a strong adsorption of sulfate and hydrogen sulfate, respectively.

Finally, in Figure 21c the catalytic activity towards the oxygen evolution reaction (OER) of bimetallic Ni/Ir_{poly} surfaces including a monoatomic Ni overlayer (Ni/Ir_{poly} OL) and a bimetallic Ni/Ir_{poly} surface alloy (NSA) are compared to each other, all measured in 0.1 M KOH. Clearly visible is the electrochemical $Ni(OH)_2$/NiOOH redox transition in the CV of the OL at ~ 1.4 V_{RHE} (see inset) proving that the conditions under which the deposition was conducted successfully forms a Ni overlayer on a polycrystalline Ir surface. Ni/Ir_{poly} OL electrode

additionally showed a higher OER activity than the Ni/Ir_{poly} NSA. When the OL electrode surface was subsequently annealed at 400°C for 2 min in a reducing atmosphere, the Ni atoms diffused into the Ir crystal and formed the near surface alloy structure (Ni/Ir_{poly} NSA).[96, 104] The formation of the surface alloy, likely with a single segregated Ir atom top layer, was evidenced by the absence of the $Ni(OH)_2$/NiOOH redox peak. This near surface alloy exhibited a loss in its catalytic OER activity when compared to the OL.

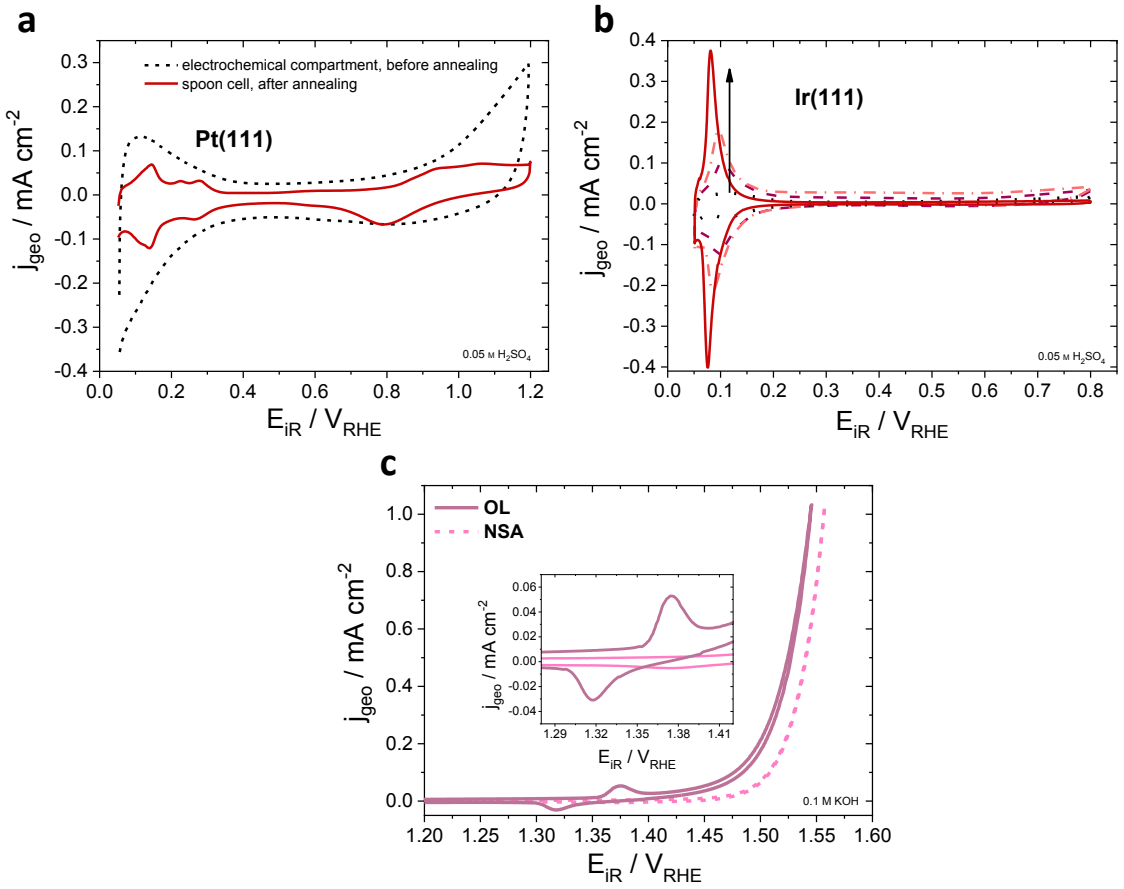

Figure 21| (a) Electrochemical surface characterization of Pt(111) cylinder in 0.05 M H_2SO_4 measured with 50 mV s^{-1} in the electrochemical compartment without preparation and in the spoon after annealing for 2 min in 4 % H_2/Ar at 800 °C. (b) Cyclic voltammogram of a well-defined Ir(111) single crystal in 0.05 M H_2SO_4 at 50 mV s^{-1} during preparation at 1900 °C: (···) initial, (---) after 20 heating periods, (··-) after 40 heating periods and (–) final CV. (c) Voltammetric anodic scans of a Ni/Ir_{poly} OL (overlayer) and a Ni/Ir_{poly} NSA (near-surface alloy) in 0.1 M KOH at a scan rate of 5 mV s^{-1} into the potential region of the oxygen evolution reaction (OER).

Chapter 6 Ir-Ni Bimetallic OER Catalysts Prepared by Controlled Ni Electrodeposition on Ir_{poly} and Ir(111)

This chapter is predominantly based on the following publication:

E. Özer, I. Sinev, A. M. Mingers, J. Araujo, T. Kropp, M. Mavrikakis, K. J. J. Mayrhofer, B. R. Cuenya and P. Strasser, *Surfaces* **2018**, *1*(1), 165 (DOI: https://doi.org/10.3390/surfaces1010013).

6.1 Introduction

Ir as one of the most important electrode materials for basic surface science and industrial applications (i.e. in the automotive industry as a component of exhausts and as a catalyst for the prediction of acetic acid) enjoys a high position in the field of electrochemistry due to its enhanced catalytic properties in water splitting electrolyzers.[105, 106] Its efficiency or the efficiency of electrolyzers in general and thus the catalytic properties are highly dependent on the interface between electrode surface and electrolyte. However, the main impediments to an effective application of water electrolysis as a sustainable method for hydrogen production are the high potential losses at the anode side and the potential limitations at the anode side and high Ir material costs. In this context, studies on low index surfaces of single crystals offer a meaningful opportunity for the fundamental understanding, and based on it, the rational design of enhanced electrocatalytic materials. A wealth of information on structural and electronic effects can emerge from these studies, particularly in the context of electrochemical deposition of metal adsorbates at sub-monolayer coverage including underpotential deposition (UPD). Potential-controlled deposition results in the growth of a new two-dimensional phase, which is believed to have electronic properties that differ significantly from those of the respective bulk materials. In addition, the electronic structure of the substrate itself and thus the interfacial reactivity is altered by the metal adatoms.[107, 108] These systems therefore offer a great variability in optimizing the binding energies to the reaction intermediates. The deposition of metal adatoms on foreign metal substrates provides attractive systems with highly controllable surface coverages by means of electrode potential and deposition time. In particular, the resulting structure and surface properties of the new electrochemical materials

are dependent on the variable surface coverage and thereby allow for a precise and reproducible control of the coverage-dependent properties.

The UPD, which has already been known since the early years of the last century[109-111] is a cost-effective method, by which the atomic and electronic structure of active sites can be controlled through electrolyte composition, applied potential and crystal plane. In the UPD process, a sub-monolayer or monolayer of a foreign metal is electrochemically deposited onto a substrate at electrode potentials that are more positive with respect to the Nernst potential for bulk deposition of the foreign metal. The electrodeposition of different metals on single crystalline and polycrystalline substrates and its theoretical aspects have been extensively studied only in the past decades and are included in the works of Kolb *et al.*[112], Adzic *et al.*[113] and Szabó *et al.*[114] Whereas electrochemical techniques offer a profound insight into the kinetics and mechanisms of the UPD process at the interface of the metal substrate and the electrolyte solution, surface science techniques are required to characterize and identify species formed at the surface. Due to its practical importance in surface chemistry and electrocatalysis[115] a number of *ex situ* and *in situ* techniques such as cyclic voltammetry (CV), scanning tunneling microscopy (STM), X-ray photoelectron spectroscopy (XPS) and low-energy electron diffraction (LEED) have been applied to augment the process of deposition at the molecular and atomic level.[116]

In this chapter, the deposition of Ni on polycrystalline Ir and well-characterized Ir(111) electrodes in both sulfate-containing electrolytes and phosphate-buffered solutions will be presented employing experimental techniques. *In situ* cyclic current-potential curves are used to detect the redox potentials of the electroactive species or rather the potential range in which deposition takes place. The well-established *ex situ* X-ray photoelectron spectroscopy (XPS) technique provides a complete information on the chemical composition of the surface and subsurface structure. Due to the narrow penetration depth of the X-rays, the obtained data is limited to the outer ~ 5 nm of the examined samples. In addition, a more quantitative trace metal analysis was performed with inductively coupled plasma-mass spectrometry (ICP-MS) to determine the adsorbed metal concentration based on high sensitivity and detection capability. Surface sensitive CO stripping measurements in combination with theoretically calculated hydrogen binding energies provide valuable insights into the morphological and structural composition of the deposit. The Faraday charge efficiencies (FE) towards oxygen

evolution of the modified electrodes were measured with differential electrochemical mass spectrometry (DEMS) and confirmed that the entire charge is transferred to facilitate the OER.

Due to the higher degree of complexity to prepare and maintain well-ordered and clean single crystal electrodes, a majority of the work has been carried out on polycrystalline Ir electrodes to study the multi-faceted Ni deposition process and to establish profound procedures and protocols for the precise control of surface coverage and structural composition. The intent is to present a broad overview and to provide detailed observations of the deposition process of Ni on Ir using not only electrochemical methods but also knowledge obtained from other surface sensitive techniques. The following studies and conclusions therefore present a first step in the electrodeposition of Ni layers on Ir electrodes and their electrochemical properties in the oxygen evolution reaction (OER). The results of this research expand the fundamental knowledge about the deposition process on polycrystalline Ir and show initial studies on Ir(111) single crystal electrodes under well-defined conditions of cleanliness thanks to the custom-made inductive and electrochemical crystal chamber introduced in Chapter 5.

6.2 Experimental

6.2.1 Substrates

Ir(111) single crystalline and Ir polycrystalline (I_{rpoly}) electrodes were used as working electrodes for the potential-controlled deposition of monolayer and sub-monolayer amounts of Ni. Ir_{poly} was applied for preliminary measurements to determine the desired information about the amount of deposited metal in dependence of the applied potential.

6.2.1.1 Ir(111) Single Crystal

Ir(111) single crystal electrodes with a diameter of 10 mm and a precision of orientation of ≤ 0.1° (MaTecK GmbH, Jülich) were applied as working electrodes for the study of surface modification. To mount the cylinder into the inductive and electrochemical setup, two continuous lateral holes with a diameter of 0.5 mm were machined into the shell surface through which loops made of Ir wire (Alfa Aesar, ∅ = 0.25 mm, 99.9 %) run. In order to refine the surface thermally, the single crystal electrode was introduced into a custom-made inductive electrochemical single

crystal chamber specifically constructed for this purpose (see Chapter 5). Section 5.2.5 describes in detail how single crystal electrodes are mounted into the setup. The heating protocol (see section 5.3) is applied until the determined electrochemical surface characterization is consistent with a perfectly clean and well-ordered (111) single crystalline Ir surface.

6.2.1.2 Ir Polycrystal

The polycrystalline Ir cylinder was manufactured by MaTecK (purity 99.999 %) with a diameter of 10 mm and a height of 4 mm. For mounting into the inductive setup, two continuous lateral holes with a diameter of 0.5 mm were machined into the shell surface. Through these holes, loops made of tungsten wire run. Before each experiment, the electrodes were mounted into a custom-made Teflon holder for the grinding and polishing procedure. To ensure the surface of the cylinder sits flush with the holder (Figure 22b), its height can be adjusted with a Teflon stick (Figure **22**c) and a screw (Figure 22d), which will be positioned in the back of the holder.

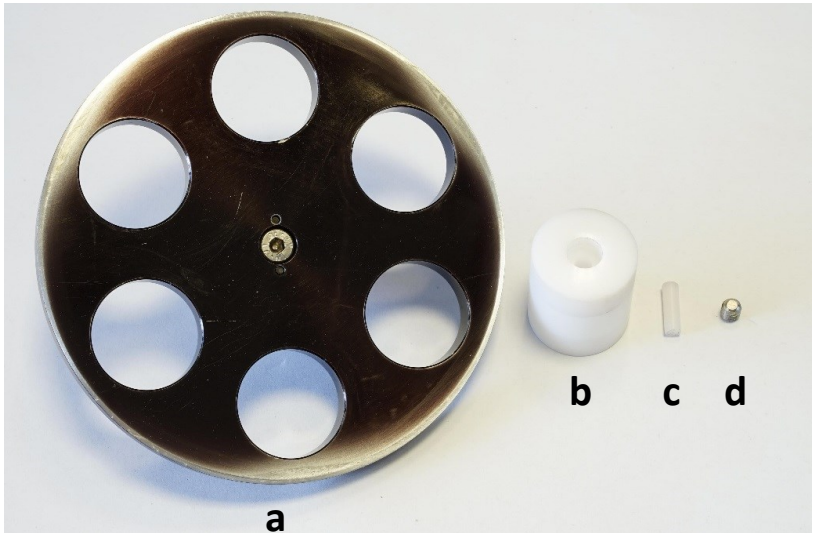

Figure 22| Equipment for polishing of poly crystalline Ir cylinder to a mirror-like surface. (a) Central force polishing head and sample holder into which the (b) Teflon holder together with the cylinder is integrated. The height of the cylinder is adjusted with a (c) Teflon stick and (c) a locking screw.

The grinding and polishing were performed with a half automatic polishing machine (AutoMet 250, Buehler) until a mirror-like surface finish was obtained. Basically, the mechanical preparation implies the usage of finer grain sized grinding

particles for each consecutive polishing step. All grinding and polishing settings are given in Table 3.

Initially, the electrode was ground with SiC grinding paper (P320, Buehler) to remove excess material from a deformed or damaged material. This step also aims at producing an entirely planar surface with minimal damages, which can be easily removed by polishing. In the following next two steps, the occurred damages are eliminated by diamond polishing. Hereto a diamond suspension (MetaDi Supreme 9 µm, Buehler) is used in combination with the polishing cloth TextMet C. In a final step the mirror-like surface finish is achieved by applying a smaller grain size of the polishing agent (MetaDi Supreme 1 µm, Buehler) and using MicroFloc as polishing cloth. To avoid cross-contamination of the polishing agents and to remove polishing residues, the Ir cylinder must be sonicated in distilled water between the individual steps and after the complete polishing procedure also.

Table 3| Settings for grinding and polishing of a polycrystalline Ir electrode in a half automatic polishing machine (AutoMet 250, Buehler).

	Step 1: grinding	*Step 2: polishing*	*Step 3: polishing*
polishing cloth	grinding paper P320	TexMet C	MicroFloc
polishing agent	water	MetaDi Supreme 9 µm	MetaDi Supreme 1µm
rotation *base / rpm* *head / rpm*	complimentary 200 60	contra 150 30	contra 150 30
force / N	5	30	20
time / min	1	5	10

6.2.2 Electrochemical Characterization

6.2.2.1 Ni Deposition Experiments

The electrodeposition of Ni on Ir electrodes was studied at a polycrystalline Ir electrode Ir_{poly} and at a single crystalline Ir(111) cylinder. The electrochemical measurements with Ir_{poly} were conducted in a rotating disk electrode setup (see section 6.2.2.1). The Ir(111) single crystal was measured in a custom-made setup as described in Chapter 5.

Four different types of experiments were conducted. Initially (experiment 1), the cyclic voltammograms of Ir(111) were evaluated in 0.05 M H_2SO_4 and in a phosphate

buffer solution of pH 6.85 (0.1 M KH_2PO_4 and 0.1 M K_2HPO_4, 1:1 mixture by volume) in the absence and presence of 2 mM $NiSO_4$. The polycrystalline Ir electrode was measured solely in phosphate buffer solution. The electrodes were immersed at an upper potential limit of 0.8 V_{RHE} and 1.0 V_{RHE} for Ir(111) and Ir_{poly}, respectively and cycled in the respective potential window to determine the charge of Ni adsorption-desorption.

The potential range of Ni deposition in phosphate buffer was examined more thoroughly in the second experiment. To this, the amount of deposited Ni on Ir_{poly} was examined at six potentials in the potential range determined in the first experiment. The electrode was immersed under potential control and the respective potential was held for a time of 10 min. Subsequently, the coverage of Ni was determined by inductively coupled plasma mass spectrometry (ICP-MS) after dissolving all Ni during immersing the electrode in 5 ml 0.1 M HNO_3 for one hour after they were rinsed thoroughly with milli-q water.

In a next step (experiment 3), the deposition of Ni at Ir(111) was examined by surface sensitive techniques including X-ray photoelectron spectroscopy (XPS) and atomic force microscopy (AFM). These measurements also served to validate the air-free transport process from the novel inductive and electrochemical setup[117] into the transfer chamber (see section 5.2.4) and further into the analysis chamber.

Finally in experiment 4, OER activities were measured with Ni-modified Ir_{poly} electrodes in both acidic and alkaline medium and compared to the unmodified and pristine Ir_{poly}. In addition, differential electrochemical mass spectrometry (DEMS) was used to identify the evolved products during OER. To gain surface sensitive information on the favored deposition sites of Ni, CO stripping experiments were performed on three catalyst systems, including the unmodified polycrystalline Ir electrode, an overlayer of Ni on Ir_{poly} (Ni/Ir_{poly} OL) and a near-surface alloy (NSA) in which Ni is present in the subsurface (Ni/Ir_{poly} NSA).

6.2.2.1.1 Ni Sweep Voltammetry (Experiment 1)

The Ni electrodeposition was studied using the cyclic voltammetry technique in strong acidic medium and in phosphate buffer. The well-defined single crystalline and polycrystalline electrodes were transferred into the degassed solution containing 2 mM $NiSO_4$. A voltammetric scan was then performed from the immersion potential of 1.0 V_{RHE} for Ir_{poly} and 0.8 V_{RHE} for Ir(111) to the negative potential limit of 0.05 V_{RHE} at a scan rate of 50 mV s^{-1}. Under the same conditions,

cyclic voltammograms of the electrodes were recorded in the absence of Ni^{2+} ions to locate the Ni adsorption-desorption region. These solutions, however, contained 2 mM Na_2SO_4 to have the same anion concentration in both electrolytes. To trace conductivity changes of the electrode, impedance spectroscopy was conducted to determine the ohmic drop of the electrode. In both electrochemical measurements, the voltammetric scan ended at the positive potential limit to ensure the oxidation of all deposited Ni. All electrolytes were purged with either Ar (Ir(111) in the inductive setup) or N_2 (Ir_{poly} in the RDE) for at least 15 min to remove dissolved oxygen prior to use.

6.2.2.1.2 Preparation of Ni Overlayers (OL) and Ni (Near-) Surface Alloys (NSA)

To produce an overlayer of Ni (Ni/Ir OL), the electrode was immersed at the desired deposition potential into a phosphate buffer solution of pH 6.85 (0.1 M KH_2PO_4, 0.1 M K_2HPO_4) containing 2 mM $NiSO_4$ and held for 10 min. The Ni/Ir_{poly} OL electrode catalyst for further electrochemical testing was produced at a deposition potential of 0.05 V_{RHE}.

For establishing a dependence of the deposited Ni amount as a function of deposition potential, the Ni/Ir_{poly} OL electrodes were immersed in 5 ml 0.1 M HNO_3 for one hour. Ni deposition at Ir_{poly} was studied in a potential window between 0.05 and 0.5 V_{RHE}. The total metal content of the deposition process was determined using ICP-MS.

For the preparation of the Ni/Ir_{poly} near surface alloy (NSA) the Ni/Ir_{poly} OL electrode (E_{dep} = 0.05 V_{RHE}) was subsequently annealed for 1 min in 4 % H_2/Ar at 400 °C in the custom-made inductive setup presented in Chapter 5. The Ni-modified catalysts were then tested for OER activity in 0.1 M KOH and 0.05 M H_2SO_4. A detailed description of the electrochemical OER testing, the DESM measurements and the CO stripping measurements can be found in the next sections.

6.2.2.2 Rotating Disk Electrode Setup

The electrochemical experiments on polycrystalline Ir were performed in a rotating disk electrode (RDE) setup at room temperature. The three-compartment cell consists of a Luggin capillary arrangement and platinum based counter electrode. A saturated mercury/mercury sulfate (MMS) was used as the reference electrode, with potentials corrected to the RHE scale. The MMS was calibrated regularly against a reversible hydrogen electrode in the same electrolyte at RT. The

potentiostat used was a SP-200 potentiostat (BioLogic, France). To mount the cylinder into the measurement equipment a custom-made RDE sample holder was used. Prior to mounting into the assembly, a conical Teflon ring was strapped on and after that introduced into the sample grid.[118] A screw nut was put on to further tighten the cylinder into the holder and to keep the electrode from falling off. The electrical contact was provided through a gold contact pin screwed into the back of the holder. The sample holder was then mount into an RDE shaft and installed into the RDE setup.

6.2.2.3 Electrochemical OER Protocol at RDE

Two types of OER protocols were used to test the performance of unmodified and Ni-modified Ir_{poly} electrodes at the RDE. The schematic illustration in Figure 23 shows the sequence of electrochemical measurements for both OER protocols. In OER protocol I, the OER activities of Ir_{poly}, Ni/Ir_{poly} OL and Ni/Ir_{poly} NSA were tested in both 0.05 M H_2SO_4 and 01 M KOH. The electrolytes were prepared by dilution of 95 % H_2SO_4 (Suprapure, Carl Roth) with ultrapure water. For electrochemical OER measurements in an alkaline electrolyte, purified Fe free 0.1 M KOH was prepared according to the method reported by Trotochaud *et al.*[119]

In a separate protocol, the stability of the Ni/Ir_{poly} OL catalyst was subject to greater stress. Hereto, the catalyst was first tortured in 0.05 M H_2SO_4 before continuing the OER measurement in 0.1 M KOH. In between measurements, the electrode was rinsed thoroughly with milli-q water.

Both OER protocols are schematically presented in Figure 23. For both procedures, the immersion of the electrodes at 1.00 V_{RHE} was followed by 10 polarization curves into the potential region of OER at a scan rate of 5 mV s^{-1} from the immersion potential up until a current of 0.785 mA cm^{-2} (current density of 1 mA cm^{-2}) was reached. The measured currents are normalized to the geometric area of the electrodes to provide comparable current densities (j_{geo}). The geometric surface area of the electrodes is 0.785 cm^2 corresponding to the diameter of 10 mm. After the 10 consecutive cycles into the OER region, electrochemical impedance spectroscopy (PEIS) was measured to obtain the ohmic resistance. The respective potentials are referred to as E_{iR}.

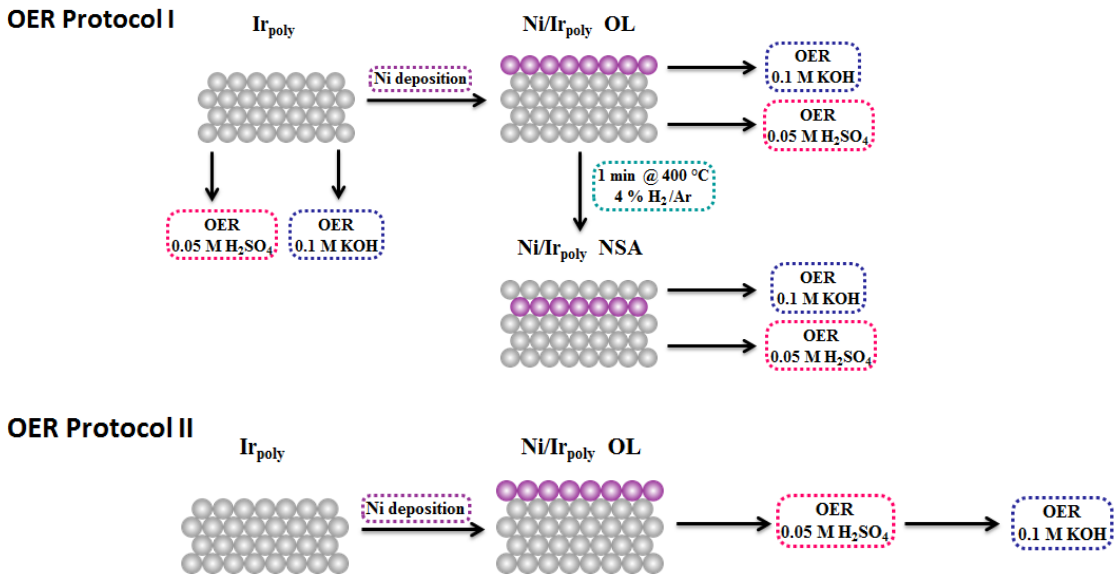

Figure 23 | Schematic illustration of the OER measuring sequences at the RDE of I_{poly}, Ni/Ir_{poly} (OL) and Ni/Ir_{poly} (NSA).

6.2.2.4 CO Stripping Protocol

The CO stripping measurements were carried out in a rotating disk electrode setup (RDE) resembling a three-electrode setup employed with a reversible hydrogen electrode (RHE) as reference electrode and a Pt-mesh as counter electrode. The measurements were recorded on a Bio-Logic SP-200 potentiostat. A polycrystalline Ir cylinder polished according to the description given in section 6.2.1.2 was used as working electrode in this study. Before each experiment, the electrode was electrochemically cleaned in N_2-degassed 0.05 M H_2SO_4 by repetitive cycling between the potentials 0.05 V_{RHE} and 0.8 V_{RHE} until a stable voltammogram evolved. The CO stripping measurements were performed on an unmodified Ir_{poly} and two Ni modified Ir_{poly} electrodes. Ni/Ir_{poly} OL and Ni/Ir_{poly} NSA electrodes were prepared as described in section 6.2.2. Purified Fe free 0.1 M KOH, prepared from high purity reagents (semiconductor grade, 99.99% trace metals basis, Aldrich) and milli-q water (Millipore MilliQ gradient, 18.2 MΩ) was used as electrolyte. The purification of KOH was performed using the method reported by Trotochaud *et al.*[119]

In a first step of the CO protocol, the electrolyte was deoxygenated with N_2 (99.998 %, Air Liquide Deutschland GmbH) for at least 15 min before the working electrode was immersed under potential control at 0.05 V_{RHE}. After just another 5 min, the electrolyte was saturated with CO (99.999 %, Air Liquide Deutschland GmbH) for 15 min, followed by N_2 purging for 15 min to remove excess CO from the

electrolyte. Finally, the oxidation of adsorbed CO was initiated by scanning the potential in the positive direction to 1.4 V_{RHE} with 50 mV s^{-1} under rotation of 1000 rpm.

6.2.2.4.1 DFT Calculated H-Ir Binding Energies (in collaboration with Thomas Kropp, Manos Mavrikakis)

Theoretical H-Ir binding energies were calculated using the projector augmented wave (PAW) method[120, 121] as implemented in the Vienna ab initio simulation package (VASP).[122, 123] Exchange–correlation energies were obtained using the functional by Perdew, Burke, and Ernzerhof (PBE).[124] A plane wave cutoff of 600 eV was used. Structure optimizations were performed until total energies were converged to 10^{-6} eV, and forces acting on the relaxed ions were below 0.02 eV $Å^{-1}$.

Surface models were obtained by cutting bulk iridium (lattice constant a = 8.877 Å) in (001), (011), and (111) orientation. The resulting slab models consist of five atomic layers separated by a 12 Å vacuum layer. The lowest two atomic layers are frozen to simulate the bulk. For Ir(001) and Ir(111), the Brillouin zone was sampled at $6 \times 6 \times 1$ k points, while $4 \times 4 \times 1$ k points were used for the larger Ir(011) model.

6.2.3 Mass Spectrometry

6.2.3.1 Differential Electrochemical Mass Spectrometry (in collaboration with Jorge Ferreira Araujo)

Differential electrochemical mass spectrometry (DEMS) was acquired in a custom-made dual thin-layer electrochemical flow cell based on the concept reported elsewhere.[125, 126] A Prisma quadrupole mass spectrometer (QMS 200, Pfeiffer-Vacuum) equipped with two turbomolecular pumps (HiPace 80) operating under 10-6 mbar was applied to detect any volatile products. The instrument allows a continuous flow of the electrolyte of 2-10 µl through the hydrophobic pores to the MS ion source. Here, a high mass transport rate is assured, as the electrolyte volume near the electrode is being reduced. The thin film of electrolyte below the working electrode allows for high ionic currents. A hydrophobic PTFE membrane with a pore size of 30 nm and a thickness of 150 µm (Cobetter, Cat. No. PF-003HS) separates the electrolyte from the chamber.

The electrochemistry was controlled using a BioLogic potentiostat, a leak-free Ag/AgCl as reference electrode (Warner Instruments), and a Pt mesh as counter

electrode. Cyclic voltammograms (CVs) in 0.1 M KOH and 0.05 M H_2SO_4 were recorded between the potential range of 0.6 and 1.6 V_{RHE} (prior to iR-compensation) at a scan-rate of 50 mV s^{-1}. The flow cell setup was used for evaluating the faradaic charge efficiencies towards oxygen evolution for Ni-modified polycrystalline Ir electrodes. The preparation of the electrodes is described in section 6.2.2. The measurements were also performed with the untreated and pristine Ir_{poly} as a reference. In a first step, the ionic current baseline was recorded in a steady-state measurement to obtain a catalyst-specific calibration factor K^*. A constant purge N_2 flow at a flow rate of 8 µL s^{-1} ensures that the electrolyte is oxygen-free before the electrodes are integrated into the flow cell. Formation of volatile products (m/z 2, 16, 18, 28, 30, 36, 32, 34, 44) was monitored during the CV scan. The aforementioned catalyst-specific calibration factor K_j^* was applied for quantification of the faradaic efficiency (FE) of O_2 (m/z 32). Hereto, chronopotentiometric steps were applied in the linear region of the ionic current baseline during the steady-state measurement. In the following equation *(6.1)* the relation between the mass spectrometric ion current ($i_{MS,j}$) and the faradaic current (i_F) to the volatile product j is given.

$$K_j^* = \frac{i_{MS,j} \cdot z_j}{i_F} \qquad \textbf{(6.1)}$$

Here, z_j is the number of transferred electrons per molecule of volatile product j. The division of the integrated mass spectrometric ion current ($Q_{MS,j}$) by the integrated capacitive current-corrected, faradaic current (Q_F), allows for determination of the faradaic efficiency (FE) (charge selectivity) according to equation *(6.2)*.

$$FE(\%) = \frac{Q_{MS,j} \cdot z_j}{Q_F \cdot K_j^*} \cdot 100 = \frac{Q_{F,j}^{DEMS}}{Q_F} \cdot 100 \qquad \textbf{(6.2)}$$

In the analysis, only anodic faradaic currents are taken into account as solely the anodic processes of molecular oxygen evolution is of interest. The limits of integration were given by the detection signal of oxygen evolution (m/z 32) and initial baseline level. For the different samples, the limits varied due to distinct onset potentials for oxygen evolution.

A photograph of the Differential Electrochemical Mass Spectrometric (DEMS) dual thin-layer flow cell in Figure 24a shows the working electrode compartment in enlarged display. The measurements with Ø 10 mm cylinders are performed with the PEEK holder presented in Figure 24b. Initially the working electrode is pressed

on to the Teflon spacer to ensure that a constant thin layer of electrolyte is formed at the surface of the working electrode. The electrical contact is generated at the back of the electrode with the tip of the custom-made PINE holder. After placing the flow cell into the vacuum system, the purged electrolyte flow will be opened. Once the MS chamber has been in contact with electrolyte, the vacuum can be opened.

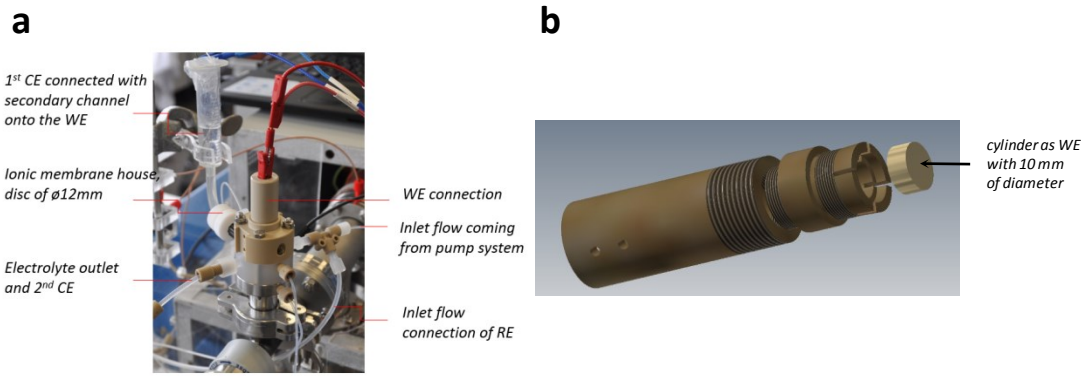

Figure 24| Differential Electrochemical Mass Spectrometric (DEMS) dual thin layer flow cell. (a) Detailed photograph of the working electrode compartment in enlarged display. (b) Schematic drawing of the PEEK holder used for working electrodes (WEs) with a diameter of 10 mm. The WE is tightened in the PEEK holder with the integrated Teflon spacer.

6.2.4 Physicochemical Characterization

6.2.4.1 Inductively Coupled Plasma Mass Spectrometry (ICP-MS)

ICP-MS of the HNO_3 aliquots taken to dissolve the electrodeposited nickel was measured with a NexION 300 X equipped with a Meinhard nebulizer and a spray chamber. In a first step, the Ni sample is introduced into the nebulizer by a peristaltic pump. In the enclosed spray chamber, the Ar flow produces an aerosol of the sample that is then ionized by plasma. The plasma is created by inductively heated Ar gas with a flow of 15 l min^{-1} through a strong electromagnetic coil. The radio frequency (RF) power of the plasma was held at 1300 W. In the high vacuum zone (~ 10^{-7} Torr) a quadrupole mass filter detects the desired ions based on their mass to charge ration which then reach the dynode-type detector. A detailed description of the operation principle can be found elsewhere.[127]

6.2.4.2 Atomic Force Microscopy (AFM)

The AFM images were done in tapping mode using a Bruker MultiMode 8 microscope on the samples after transport in Ar. In the tapping mode, the distance

between the tip and the sample's surface is in the median distance range of 0.5 - 2 nm. Here, the topography is mapped by lightly tapping the surface with the sharp ending of the AFM probe. In this mode, attractive and repulsive forces from the surface of the sample interact resulting in the oscillation of the cantilever at the tip's resonant frequency (dynamic mode), providing a high resolution.

6.2.4.3 X-ray Photoelectron Spectroscopy (XPS)

The pristine and the Ni modified Ir(111) surfaces were analyzed by X-ray photoelectron spectroscopy in an UHV setup equipped with Phoibos 150-MCD 9 hemispherical analyzer (SPECS GmbH). A monochromatic Al Kα X-ray source ($h\nu$ = 1486.5 eV) at 12 kV of anodic voltage and 300 W of emission power was used to perform the characterization. For calibration of the binding energy, the C 1s signal of graphitic-like carbon (285 eV) was used. For peak deconvolution, Gaussian-Lorentzian product functions and Shirley background were applied in the Casa XPS software.

6.3 Results and Discussion

6.3.1 Calculation of Surface Coverage and Roughness Factor of Ir_{poly}

A dependence of the amount of deposited nickel on Ir_{poly} on the applied deposition potential was established by analyzing the quantity of deposited Ni by ICP-MS in section 6.3.2.2. In order to transfer these values into monolayer (ML) specifications, the determination of the surface roughness of the polycrystalline Ir electrode is an important prerequisite. Hereto electrochemical double-layer capacitance measurements were carried out using cyclic voltammetry (CV) as has been proposed in the work of McCrory *et al.*[26] The calculations are based on the relationship in equation *(6.3)*, which states that the double-layer charging current density is equal to the product of the scan rate and the electrochemical double-layer capacitance (per geometric area).

$$j_c = \nu \cdot C_{dl} \tag{6.3}$$

To solely measure the electrochemical capacitance, the potential range in which no faradaic processes occur must be determined from CV measurements of the electrodes of interest. For Ir_{poly} a potential window between 0.4 and 0.5 V_{RHE} was chosen as depicted in Figure A2 in the Appendix. The roughness factor (RF) of Ir_{poly} is then calculated from the double-layer capacitance according to equation (6.2)

$$RF = \frac{C_{dl}}{C_S} \tag{6.4}$$

C_S denotes the electrochemical double-layer capacitance of a smooth and planar electrode surface of the same material measured under the same conditions and has been conducted for a single crystal Ir(111) electrode. The double-layer capacitance measurements for determining the RF of Ir(111) and Ir_{poly} are depicted in Figure 25. Given the slopes of both electrode surfaces, a roughness factor of 4.3 of the polycrystalline Ir electrode can be defined according to the following equation:

$$RF = \frac{148.6\ \mu F}{34.3\ \mu F} = 4.33 \tag{6.5}$$

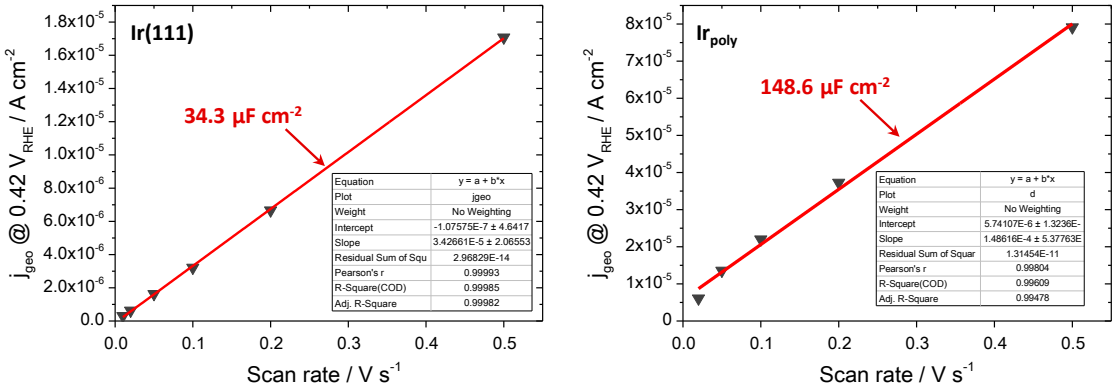

Figure 25 | Double-layer capacitance measurements of Ir(111) and Ir_{poly} displaying the anodic charging current densities measured at 0.42 V_{RHE}.

A polycrystalline crystal is composed of randomly oriented crystallites that can be distinguished from a single crystal. It is assumed that the terraces consist of the three low-index surfaces (111), (110) and (100) almost to the same extent. Thus, it is legitimate to assume a predominant (111) face on Ir_{poly} for the following calculations. First, the number of Ir atoms per unit area must be known that can participate in the adsorption and desorption of Ni to further determine the Ni amount needed to produce a monolayer on a (111) face of Ir.

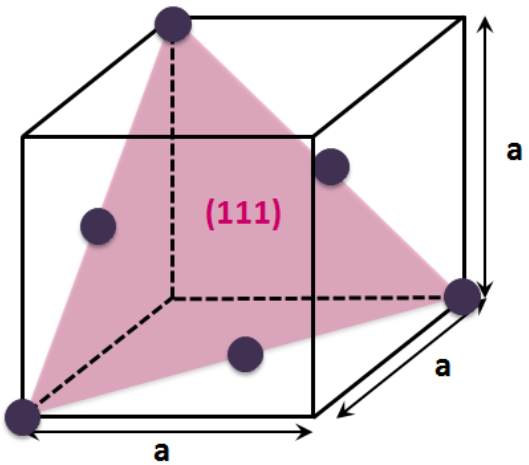

Figure 26| Unit cell of a face-centered cubic (fcc) lattice displaying the (111) face and the Ir(111) atoms.

In a first step, the surface area of the (111) face is calculated from the lattice parameter of Ir. Hence,

$$area\ calculation: A_{111} = \sqrt{\frac{3}{4}} \cdot a^2 \qquad \textbf{(6.6)}$$

$$lattcie\ parameter\ Ir: a = 3.8394\ \text{Å}\ \ (\text{PDF: } 00-006-0598) \qquad \textbf{(6.7)}$$

$$\rightarrow A_{111} = 1.277 \cdot 10^{-15}\ \mathrm{cm}^2 \quad \textbf{(6.8)}$$

Subsequently, the number of atoms per (111) face in the unit cell must be determined as:

$$edges: 3 \cdot \frac{1}{2} \quad \textbf{(6.9)}$$

$$corners: 3 \cdot \frac{1}{6} \quad \textbf{(6.10)}$$

$$\rightarrow 2\ atoms\ per\ (111)\ face \quad \textbf{(6.11)}$$

In the next step, the counted atoms are divided by the calculated surface area to obtain the atoms per unit area $a_{(111)}$. By means of the Avogadro constant N_A, the amount of substance per surface area is introduced. Thus,

$$a_{(111)} = \frac{2}{1.277 \cdot 10^{-15}\ \mathrm{cm}^2} = 1.566 \cdot 10^{15}\ \mathrm{cm}^{-2},\ N_A = 6.022 \cdot 10^{23}\ mol^{-1} \quad \textbf{(6.12)}$$

$$n_{(111)} = \frac{1.566 \cdot 10^{15}\ \mathrm{cm}^{-2}}{6.022 \cdot 10^{23}\ mol^{-1}} = 2.6 \cdot 10^{-9}\ \frac{\mathrm{mol}}{cm^2} \quad \textbf{(6.13)}$$

It is of interest to calculate the amount of substance needed to form a complete monolayer. The (111) single crystal electrode has a diameter of 10 mm and therefore a surface area of 0.785 cm^2. Hence, equation *(6.13)* becomes

$$n_{ML} = 2.6 \frac{\mathrm{nmol}}{cm^2} \cdot 0.785\ cm^2 = 2.04 \frac{nmol}{ML} \quad \textbf{(6.14)}$$

Analogously, the mass of Ni per monolayer can be obtained by introducing the molar mass of Ni as:

$$m_{ML} = 2.04 \frac{\mathrm{nmol}}{cm^2} \cdot 58.68 \frac{g}{mol} = 0.12 \frac{\mu g}{ML} \quad \textbf{(6.15)}$$

The determined amount of adsorbed Ni by ICP-MS can now be translated into a degree of coverage for a single crystalline Ir(111) face with a diameter of 10 mm. With a given RF of 4.33, the estimated Ni amount to produce a ML on Ir_{poly} is:

$$m_{ML}(Ir_{poly}) = 0.12\ \frac{\mu g}{ML} \cdot 4.33 = 0.52\ \frac{\mu g}{ML} \quad \textbf{(6.16)}$$

The calculated values in dependence of the deposition potential and the degree of coverage are given in section 6.3.2.2.

6.3.2 Surface Chemical Characterization

The study of Ni deposition was conducted and analyzed on polycrystalline Ir (Ir_{poly}) and single crystalline Ir(111) electrodes. The experiments with Ir_{poly} have served to gain better understanding of the deposition process and for determining the influence of adsorbed Ni on the surface and the resulting catalytic properties. In a first step, cyclic voltammetric studies of the electrodes were used to determine the redox processes during the deposition mechanism.

6.3.2.1 Ni Deposition on Ir_{poly} by Sweep Voltammetry

The nickel deposition process on a polycrystalline Ir electrode was first studied using the cyclic voltammetry technique in order to determine the potential area in which Ni deposition occurs. Figure 27 depicts the cyclic voltammogram of a polished and electrochemically cleaned polycrystalline Ir cylinder in a phosphate buffer solution with and without 2 mM $NiSO_4$. The solution without Ni^{2+} contains 2 mM Na_2SO_4 to guarantee the same concentration of anions in the electrolyte and to make the measurements comparable. In the presence of Ni, the hydrogen adsorption-desorption region is reduced significantly suggesting a blocking of Ir sites by Ni ad-atoms. By contrast, in the negative going sweep there is only a slight distinction in the total electric charge between the cyclic voltammograms in the potential area of 0.5 to 0.0 V_{RHE}, which implies that Ni electrodeposition on Ir is not recognizable as strongly defined deposition peaks. It cannot be determined with absolute certainty if oxygen desorption in the Ni-free solution (at ~ +0.7 V_{RHE}) is shifted towards lower potentials in the presence of Ni^{2+} (at ~ +0.65 V_{RHE}) due to the so-called ligand effect[128], triggered by adsorbed Ni adatoms, or if the deposition of Ni occurs on distinct adsorption sites which are, however, merged into one broad redox wave. In the positive going sweep, desorption of Ni ad-atoms begins beyond the HUPD region and attains its maximum value at around 0.65 V_{RHE}.

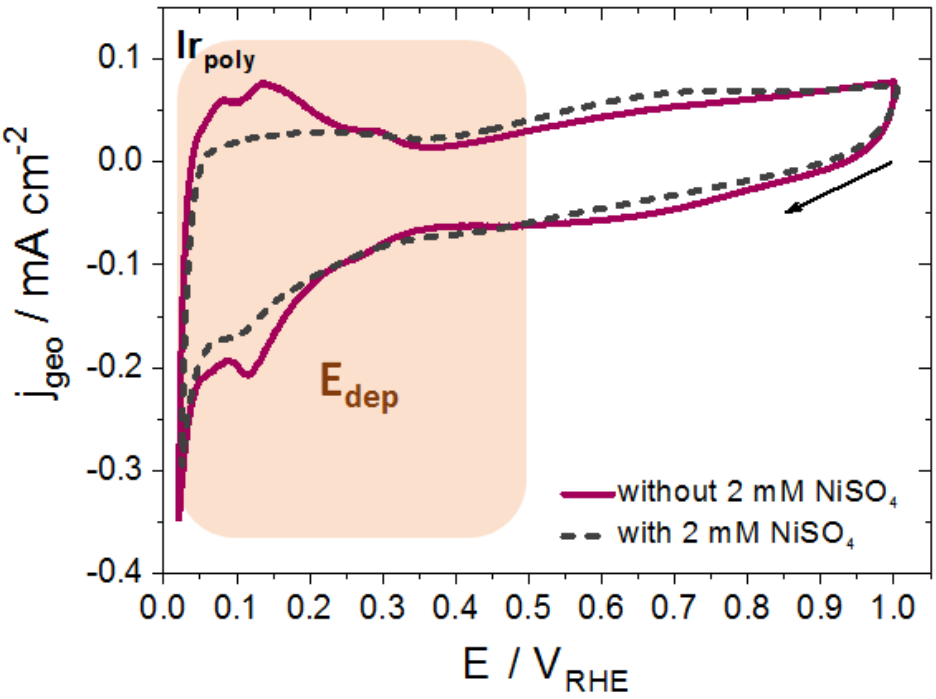

Figure 27| Cyclic voltammograms of a polycrystalline Ir electrode in a phosphate-buffered solution (ph = 6.85) containing either 2 mM Na_2SO_4 (solid lines) or 2 mM $NiSO_4$ (dashed lines) at a scan rate of v = 0.05 V s^{-1}.The electrode was polished to a mirror-like surface and electrochemically cleaned in 0.05 M H_2SO_4 prior to measurements. Immersion potential at 1.0 V_{RHE}.

Under the electrodeposition conditions specified in section 6.2.2.1 the reduction of Ni^{2+} ions to metallic Ni is relevant in accordance with the Ni Pourbaix diagram. To determine the potential region in which Ni deposition occurs, the standard potential of the redox couple (Ni/Ni^{2+}) must be converted into the RHE scale. The standard potential of (Ni/Ni^{2+}) is -0.23 V_{SHE} at standard conditions and independent of any pH shift. Given the negative shift of the zero point of the RHE scale by -0.404 V, the Nernst standard redox potential of the Ni system is +0.17 V_{RHE} under the pH of the deposition conditions. Thus, the given potential range E_{dep} between 0.05 and 0.5 V_{RHE} comprises the underpotential deposition (UPD) and some of the overpotential deposition (OPD) region of the Ni redox couple.

6.3.2.2 Ni Deposition on Ir_{poly} by Controlled-Potential Technique

The formation of a Ni layer is likely a process that requires some time, as the cyclic voltammogram in Figure 27 do not display defined Ni redox peaks. Hence, the cycling technique may not be the most suitable approach. On this account, the potential range E_{dep} in Figure 27 was used to establish a relationship between Ni coverage and applied deposition potential. Hereto, the electrode was immersed at

the desired potential under potential control and the potential was held for 10 min. The deposited amount of Ni was determined chemically by ICP-MS. The process was conducted for six distinct deposition potentials. In Figure 28 the effect of the deposition potential E_{dep} on the amount of adsorbed Ni is related. The obtained values from ICP-MS and the resultant extent of Ni monolayer formation on polycrystalline Ir are presented in Table 4. As described in section 6.3.1 the analyzed amount of Ni with ICP-MS was translated into a degree of coverage (ML) by assuming that (111) facets are prevalent on a polycrystalline Ir surface. The amount of substance of Ni to form a complete monolayer on a (111) facet are given in detail in section 6.3.1.

At first, a slight increase in Ni coverage is observed with decreasing deposition potential. The linear rise becomes larger until the Ni amount approaches a limiting value at a potential of $\leq +0.1$ V_{RHE}. As the surface of a polycrystalline Ir electrode is not well-defined, the calculated values of Ni ML coverage provide approximate guidance for the relationship between absolute molar Ni amount and deposition potential. The assumption of a prevalent (111) facet on Ir_{poly} is there by the most a severe assumption as a polycrystalline surface generally consists of a number of different types of facets. Crystallites with uniform lattice orientations are distinguished from one another without a break through grain boundaries. Some of these orientations may be less suitable or have less potential for Ni deposition. However, with an estimated average roughness factor of 4.33 for the polycrystalline Ir electrode (see section 6.3.1) a maximum coverage of ~ 0.36 ML was obtained. In the following chapters, the respective deposition window will be used for formation of the bimetallic Ni/Ir catalyst systems.

Table 4| Calculated amount of adsorbed Ni on a polycrystalline Ir electrode in dependence of deposition potential E_{dep}. The coverage of Ni (ML) was determined from ICP-MS based on the assumption of a predominant (111) face on Ir_{poly}.

E_{dep} / V_{RHE}	Ni / nmol	Ni / ML
0.05	3.178	0.36
0.10	3.157	0.36
0.20	1.857	0.21
0.30	1.018	0.12
0.40	0.844	0.09
0.50	0.635	0.07

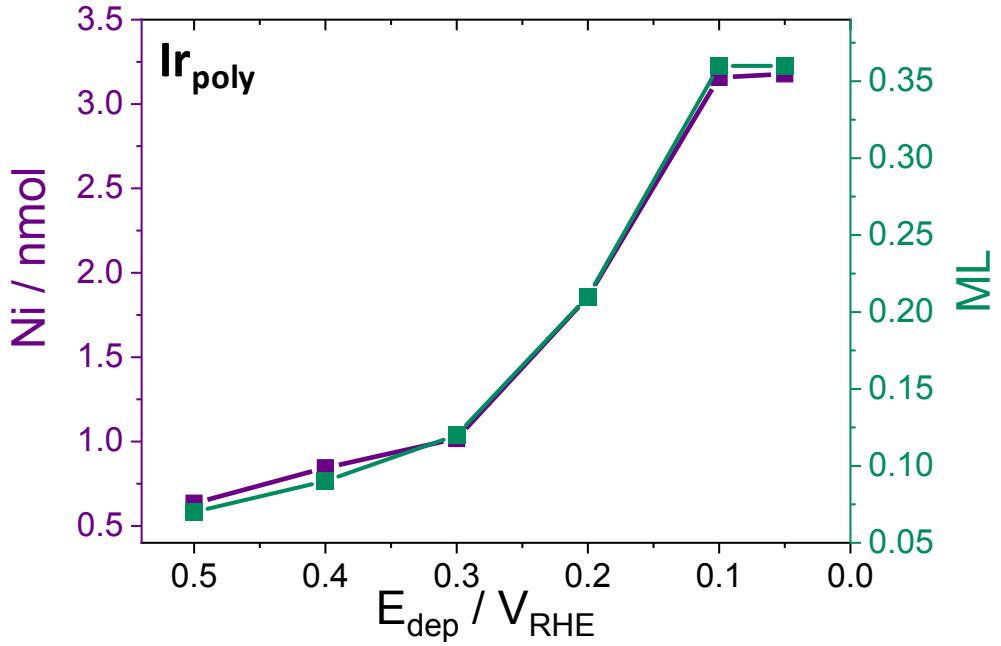

Figure 28| Relationship between amount of deposited Ni (in nmol, left axis) on polycrystalline Ir electrode and deposition potential E_{dep}. The electrode was held for 10 min at each potential in a phosphate-buffered solution (pH = 6.85) containing 2 mM $NiSO_4$. The amount of deposited Ni was analyzed by ICP-MS. The right axis (green) gives the determined value of monolayer (ML) formation.

6.3.2.3 Ni Deposition on Ir(111) by Sweep Voltammetry

6.3.2.3.1 Ni Deposition in 0.05 M H_2SO_4

The Ni deposition process on single crystalline Ir(111) electrodes was first intensively studied in 0.05 M H_2SO_4 by employing the cyclic voltammetry technique. In Figure 29 the cyclic voltammograms of a pristine Ir(111) single crystal electrode in 0.05 M H_2SO_4 in the absence and presence of 2 mM $NiSO_4$ only show noticeable differences in the hydrogen underpotential deposition (HUPD) region and a slight distinction in the negative going sweep.

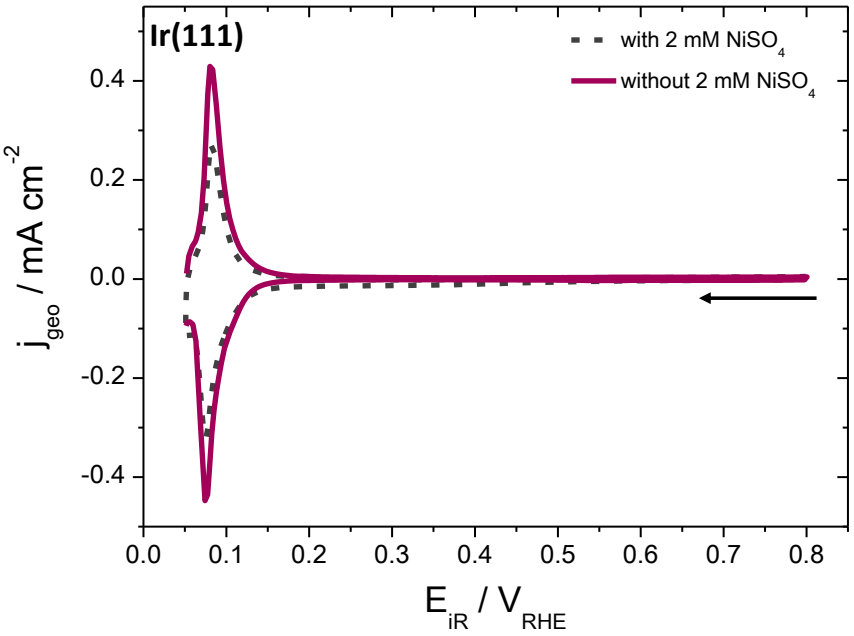

Figure 29| Cyclic voltammograms of pristine Ir(111) in 0.05 M H_2SO_4 with (dotted lined) and without (solid lines) 2 mM $NiSO_4$ at v = 50 mV s^{-1}.

A minimal increase in charge between the potential limits of 0.5 and 0.25 V_{RHE} is observed in the negative sweep and might be assigned to deposition of Ni on Ir sites, which, however, is mostly hindered as the current increase is only little. The smaller HUPD peak in the presence of Ni ions are likely due to blocking of (111) Ir sites by Ni adatoms. In the positive going sweep, the effect of charge increase is not observed. From the established observations it appears that Ni deposition on single crystalline Ir(111) occurs in the potential range of 0.5 and 0.25 V_{RHE}. However, it must be taken into consideration that the processes of hydrogen adsorption-desorption and Ni deposition might be overlapping and that the adsorption of hydrogen is more favorable than the adsorption of Ni on Ir(111) facets.

The Ni deposition process on Ir was further investigated in acidic media by decreasing the lower turning potential from 0.05 (i) to 0.01 (ii) and finally to -0.005 V_{RHE} (iii) to identify any changes in the surface chemistry of Ir(111). The corresponding voltammograms are given in Figure 30.

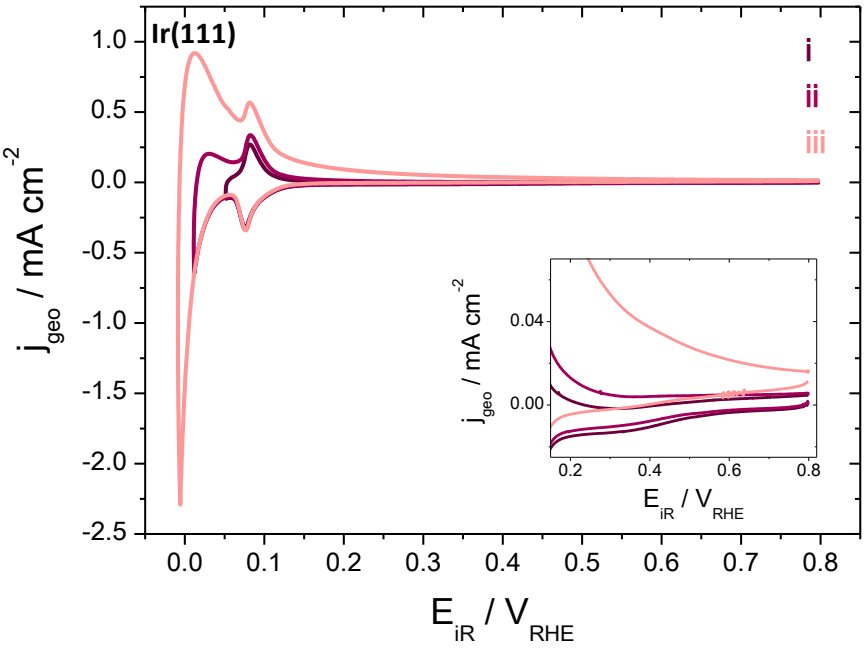

Figure 30| Cyclic voltammograms of Ir(111) in 0.05 M H_2SO_4 with 2 mM Ni_2SO_4 at a scan rate v = 0.05 V s^{-1}.The lower turning potential was successively decreased from 0.05 to 0.01 and -0.005 V_{RHE}. Each scan is cycle 3 in the given potential range.

In all three curves the region of hydrogen adsorption and desorption is well-defined. While the hydrogen evolution is only slightly present up to potentials of 0.01 V_{RHE} it is the dominating voltammetric feature in the cyclic voltammogram recorded between -0.005 and 0.8 V_{RHE}. On the reverse sweep (cathodic region), the charges associated with the deposition of Ni (corrected for the background) decrease with lower turning potential limit as is discernible from the given inset. At the same time, however, the anodic current of curve ii between the potentials of 0.2 and 0.5 V_{RHE} increases. The conclusion is reached that the Ni deposition process on single crystalline Ir(111) can be localized between the potential limits of 0.5 and 0.05 V_{RHE} as no significant stripping peak of Ni is observed in the forward sweep despite the higher potential window. The higher anodic currents are more likely to be associated with the oxidation of formed hydrogen.

6.3.2.3.2 Ni Deposition in Phosphate Buffer

The process of Ni deposition has been studied in phosphate buffer not only to separate the Ni adsorption charge from the hydrogen evolution region (HER) but also to favor the Ni layer formation in a less acidic environment. Figure 31 displays the cyclic voltammogram of a pristine Ir(111) single crystal electrode in phosphate buffer of pH 6.85 containing 2 mM $NiSO_4$. A cyclic voltammogram of the same electrode in the absence of Ni is also shown for comparison. Both voltammograms

were recorded in the potential window of 0.05 – 0.8 V_{RHE}, a potential range which is adequate for a sufficient characterization of the Ir(111) surface.[102] The CV of Ir(111) in phosphate buffer without Ni is mostly featureless and only displays the HUPD redox peak at ~+0.1 V_{RHE}. The significant difference between both voltammograms is located in the HUPD region. The characteristic HUPD peak of the (111) face is mostly masked in the presence of Ni. The voltammogram is presumably dominated by a broad deposition and stripping region of deposited Ni between 0.50 - 0.05 V_{RHE} and 0.3 - 0.8 V_{RHE}, respectively. The peak in the positive going sweep at ~ +0.1 V_{RHE} can either be ascribed to stripping off Ni or to a hydrogen desorption charge due to remaining hydrogen adsorption on Ir(111) sites or both. The latter case presupposes that not all Ir sites are being blocked by Ni adatoms during deposition. This might be a kinetically controlled problem if the deposition process by cyclic voltammetry requires some time to form a complete Ni layer. Free Ir sites may be explained by a deposition of Ni on existing Ni adatoms.

In the negative going sweep, the charge is found to be higher (≈ 375.9 µC cm^{-2}) than the sum of the charges in the positive going sweep. From this observation it seems that Ni deposition at single crystalline Ir(111) is not entirely reversible meaning that Ni is not being completely stripped off the surface in the anodic scan up to 0.8 V_{RHE}.

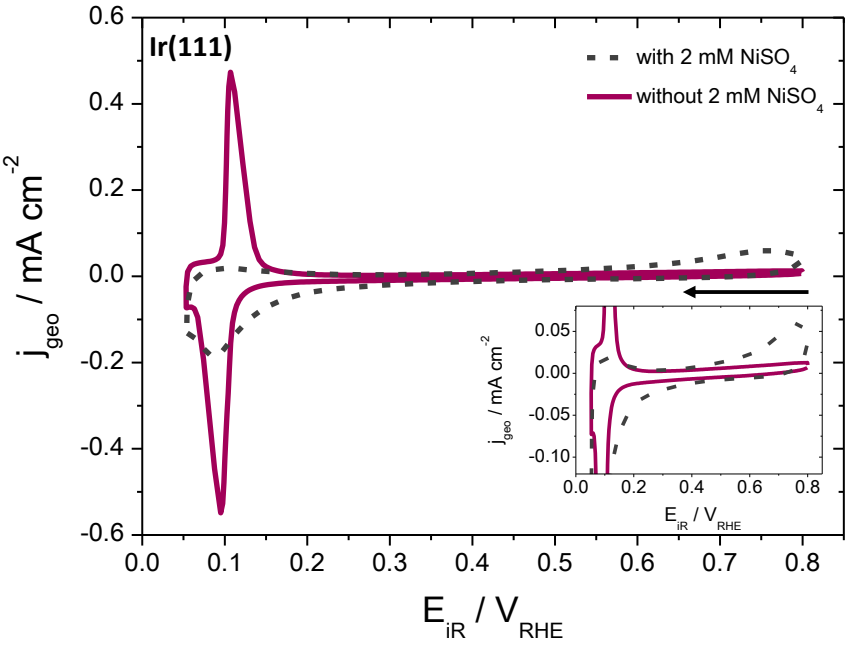

Figure 31| Cyclic voltammograms of pristine Ir(111) in phosphate buffer (pH ≈ 6.85) with (dotted lines) and without (solid lines) 2 mM $NiSO_4$ at a scan rate of v = 0.5 V s^{-1}.

6.3.2.4 X-Ray Photoelectron Spectroscopy of Ni/Ir OL

The XP spectra of the Ni-modified single and polycrystalline Ir electrodes are presented in Figure 32. The deposition was performed at a potential of 0.05 V_{RHE} to form an overlayer. The Ni overlayer on polycrystalline Ir (Ni/Ir_{poly} $OL_{t = 20\ min}$) was formed by deposition for 20 min, twice as long as for the formation of an OL on Ir(111).

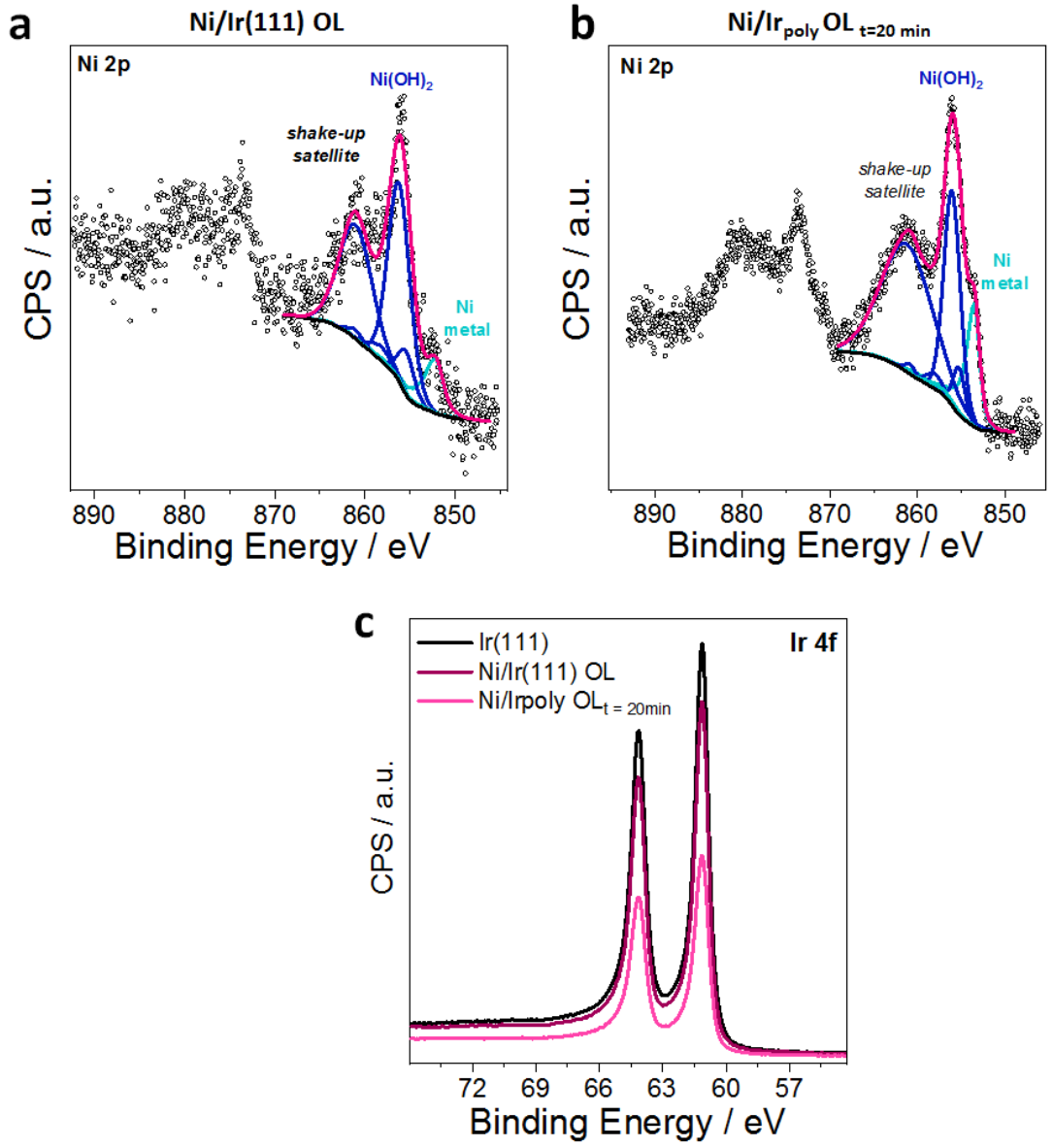

Figure 32 | XP spectra of (a) Ni modified Ir(111) single crystal(Ni/Ir(111) OL) and (b) a Ni-modified Ir polycrystal (Ni/Ir_{poly} $OL_{t = 20min}$). (c) XP spectra for the Ir 4f line for Ir(111), Ni/Ir(111) OL and Ni/Ir_{poly} $OL_{t = 20min}$. The deposition potential was 0.05 V_{RHE}. The deposition time for formation of the overlayer on Ir_{poly} was twice as long as for Ir(111).

For comparison, the XP core level spectra of the well-defined and unchanged Ir(111) single crystal are given in Figure A3 in the Appendix. Here, the survey spectrum over the entire energy range (Figure A3a, top view) is characterized by intense photoemission peaks distinctive for Ir and weak O 1s and C 1s lines. The high-resolution spectra in Figure A3b (4 panes) excludes the presence of Ni in the sample. During transfer of the single crystal into the UHV chamber and until vacuum conditions were reached, the sample was shortly exposed to laboratory atmosphere. The detected carbon and oxygen signals can therefore be assigned to chemisorbed species during the loading process. After extended exposure time, a Ni-free near surface region could be affirmed. The binding energy and line shape of Ir(111) and Ir_{poly} in the Ni-modified samples in Figure 32c are in accordance with the pure Ir spectrum. Thus, the deposition process does not affect the Ir state.

This observation is, moreover, consistent with images of the topography of the Ni-modified Ir(111) surface analyzed by atomic force microscopy (AFM). The AFM images and their respective height profiles are presented in Figure A4 in the Appendix with increasing magnifications from Figure A4a to Figure A4c. The Ni/Ir(111) OL surface was found to exhibit well-resolved flat terraces vertically separated by ~1.53 Å tall steps, which is coherent with single or double atomic steps. The Ni 2p region of all prepared samples in Figure 32a and Figure 32b indicate the prevalence of Ni^{2+} species with its main peaks at ~ 857 and 874 eV and its typical shake-up satellite peaks at ~ 863 and 880 eV. The intensity of the Ni lines increases with longer deposition time while the underlying Ir lines decrease in intensity (see Figure 32c) implying higher Ni coverages. In Ni/Ir_{poly} $OL_{t = 20\ min}$ the Ni content was determined by XPS was three times greater than on the Ni-modified single crystalline Ir sample (Ni/Ir(111) OL).

6.3.3 Impact of Ni Deposition on the Electrocatalytic Oxygen Evolution Reaction (OER) – Structure-Activity Correlations and Faraday Charge Efficiencies

There is considerable interest in optimizing the catalytic activity and simultaneously reducing the noble metal content of Ru and Ir electrodes through the addition of non-noble transition metal atoms. Even though RuO_2 electrodes offer the lowest overpotential in the OER[16, 105, 129, 130], the focus has shifted to Ir oxide electrodes as they exhibit much greater corrosion stability in combination with oxygen chemisorption energies near to the volcano top. Nong *et al.* have successfully

implemented a significant increase in intrinsic activity with IrNi@IrO_x hybrid core-shell systems.[24, 131] The effect of Ni incorporation was twofold: The higher OER activities were attributed to the increasing electrochemical surface area (ECSA) during dealloying and to electronic and strain effects in the subsurface. In the work of Reier *et al.* thermally prepared Ir-Ni mixed oxide thin-film catalysts showed a significant improvement in the OER activity compared to unmodified IrO_x catalysts.[25]

In the following section, the Ni-modified polycrystalline Ir electrodes will be discussed with respect to their electrocatalytic properties towards the OER and compared to the unmodified Ir_{poly} pristine sample. Hereto two distinct Ni-modified electrocatalytic materials were used. The Ni/Ir_{poly} OL catalyst system was prepared by deposition of Ni on a polycrystalline Ir electrode by controlled-potential technique to form a Ni rich surface are. Subsequent annealing of the OL in a reducing atmosphere for 1 min produced a material with Ni in subsurface layers as the catalyst surface CV was characterized by a hardly noticeable $Ni(OH)_2$/NiOOH redox peak. These model systems enable to identify the effect and relative position of Ni addition to the OER performance. For this, distinct OER protocols have been applied, which differ in the sequence of measurements to monitor eventual activity modifications. In addition to rotating disk electrode OER measurements, differential electrochemical mass spectrometry (DEMS) in a dual-thin layer flow cell was used to detect oxygen *in situ* mass-resolved for determining Faraday efficiencies.

6.3.3.1 Oxygen Evolution Activities and Faraday Efficiencies

In this section, the influence of the relative position of Ni on the electrocatalytic OER performance will be determined by RDE and DEMS measurements to establish correlations between structure and activity of distinct Ni-modified electrode materials.

The electrochemical OER activity of Ni-modified Ir_{poly} electrodes have been tested using the rotating disk electrode (RDE) technique in both acidic and alkaline environment according to the OER protocol I which is presented in section 6.2.2.3. The respective OER polarization curves are depicted for the first cycle in Figure 33 and are compared to the pristine and unmodified Ir_{poly} catalyst. The 10^{th} OER cycle of the electrode materials is also depicted (Figure 33c and d) to monitor the stability of the catalysts. The Ni/Ir_{poly} NSA sample was formed by reductive annealing of

Ni/Ir_{poly} OL for 1 min and shows a very weak pronounced $Ni(OH)_2/NiOOH$ redox peak in 0.1 M KOH in the 10th cycle (see Figure 33d). The reductive treatment of the overlayer for 2 min was sufficient to produce a near-surface alloy of Ni in the subsurface region.[117] Thus, a reduced time was chosen to design a surface in which Ni is both at the surface and in the subsurface of the catalyst.

As can be seen from Figure 33a and b, the geometric OER activity of the Ir_{poly} reference catalyst was improved by the addition of Ni in form of an overlayer (OL) in both electrolyte systems. The superior catalytic performance of Ni/I_{rpoly} OL in acidic solution is not only displayed via the higher current density of the cyclic voltammogram (CV) curves, but also reflected by its lower Tafel slope at higher potentials of ~ 52 mV dec^{-1} (Figure 34a), which is significantly smaller than the slope of the unmodified (~ 70 mV dec^{-1}) and NSA (~ 65 mV dec^{-1}) electrocatalysts. The lower Tafel slope of the OL system can be most likely deduced to a facile electron transport through the catalyst. Ni atoms in the subsurface layer (NSA), formed by inductive annealing of the OL, however, does not seem to have an enhanced effect on the OER activity in acidic and alkaline media. In acidic solution the OER performance of the NSA is almost identical to the unmodified Ir_{poly}. These observations indicate that the performance of the modified material is strongly influenced by the relative position of the second component in the electrode material. In order to correlate the observed reactivity with the structure of the catalyst, the surface composition of a polycrystalline surface has to be considered in detail. Given the high roughness factor (see section 6.3.1) of the polycrystalline Ir surface (due to the grain boundaries), the Ni/Ir_{poly} OL might have a similar surface structure to an Ir-Ni surface alloy in which Ni atoms are adjacent to Ir surface atoms. The result is an optimization of the binding energy towards critical reaction intermediates of the proposed oxygen evolution mechanism, such as O, OH and OOH.

In alkaline environment, the mechanism of the OER has been proposed to occur via the following steps:[25, 52, 132, 133] *(M represents the catalytic active site)*

$$M + OH^- \longrightarrow M - OH + e^- \quad \textbf{(6.17)}$$

$$M - OH + OH^- \longrightarrow M - O + H_2O + e^- \quad \textbf{(6.18)}$$

$$M - O + OH^- \longrightarrow M - OOH + e^- \quad \textbf{(6.19)}$$

$$M - OOH + OH^- \longrightarrow M - OO + H_2O + e^- \quad \textbf{(6.20)}$$

$$M - OO \longrightarrow O_2 \quad \textbf{(6.21)}$$

By annealing the OL system in a reductive atmosphere, the amount of Ni adatoms at the surface is significantly reduced. As the characteristic $Ni(OH)_2/NiOOH$ redox peak can be recognized very weakly in the cyclic voltammogram of the 10th curve in 0.1 M KOH (see Figure 33d), Ni is still present at the surface, albeit to a considerably smaller extent. The electronic effect of underlying Ni atoms on Ir surface atoms seems to have a slightly negative impact on the binding energy of reaction intermediates to Ir. However, the activity behavior of the three examined catalysts are somehow similar in KOH (see Figure 33b), whereby the pristine Ir_{poly} is slightly more active than the NSA. Interestingly, the Tafel slopes of the electrocatalysts differ significantly in both examined electrolyte solutions. In acidic solution the OL system exhibits the lowest slope followed by the NSA and the unmodified catalyst. Under alkaline conditions, the order of the Tafel slopes, however, is as follows: NSA > Ir_{poly} > OL. The analysis of the experimentally observed Tafel slopes is a powerful tool for determining the reaction steps that are rate-limiting at the reaction interface. It must be kept in mind that these parameters are greatly influenced by the concentration of the surface species formed during the reaction. In acidic the Tafel slopes of the catalysts differ far more than in alkaline milieu suggesting a greater influence of Ni on the reaction mechanism. In 0.1 M KOH the Tafel slopes lie in the range of ~ 60 mV dec^{-1} predicting a slow chemical step to be rate-limiting.[134] The above presented reaction mechanism *(6.17) – (6.21)* proposes electron-transfer steps determining the overall kinetics. However, the reaction step in *(6.18)* can also be divided into an electron transfer process subsequent to a proton transfer step as:

$$M - OH + OH^- \longrightarrow M - O^- + H_2O \qquad \textbf{(6.22)}$$

$$M - O^- \longrightarrow M - O + e^- \qquad \textbf{(6.23)}$$

Thus, if the rate-determining step involves the purely chemical step in *(6.22)*, a Tafel slope of 60 mV dec^{-1} is predicted.

The electrode processes were also measured in a dual-thin layer flow cell setup in combination with differential electrochemical mass spectroscopy (DEMS) according to the OER protocol II. The respective Faraday efficiencies (FE) and faradaic current densities are given in Figure 36. Here, the same order of activity performance was measured in alkaline solution (OL > Ir_{poly} > NSA). The superior OER performance of the Ni/Ir_{poly} OL catalyst can be deduced to surface enrichment of Ir atoms promoting positive synergies between Ir and Ni atoms. The increase in activity with

Ir-Ni binary systems has been observed in various studies in alkaline and acidic electrolytes.[25, 135-137] The higher activity of Ni/Ir_{poly} OL in acidic electrolyte may be deduced to an increase of surface OH groups initiated by leaching of the Ni adatoms from the surface.[25] Notice, that at these high potentials, partial oxidation of the catalyst surface cannot be precluded. The oxygen atoms, which were previously bound to Ni, will be protonated to become electroneutral. As OH is considered to act as a crucial intermediate in the oxygen evolution mechanism, a higher fraction of OH at the surface will have an advantageous effect on the reactivity.

As can be seen from Figure 33e all Ni-modified catalyst systems display a higher OER reactivity in 0.1 M KOH compared to the acidic milieu, which might be partly attributed to the already higher activity of polycrystalline Ir in alkaline media compared to the acidic. During repetitive cycling, the OER performance is declining for all catalysts in both systems. In H_2SO_4, the OL system shows the highest drop in activity, which is most likely due to dissolution of Ni surface atoms. After 10 cycles into the potential regions of OER, the activities of the OL and NSA in acidic solution approach each other, or in other words, the OL catalyst approaches the more stable NSA system. Here as well, the relative position of Ni is critical for the stability of the catalyst material. The addition of Ni in form of an overlayer immensely enhances the electrocatalytic activity in comparison with an unmodified reference system. However, the stability of the Ni OL system is not given in acidic media. By contrast, Ni in the subsurface layer of Ir_{poly} seems to positively affect the stability of the respective catalyst material as it shows the lowest drop in current density during the 10 cycles.

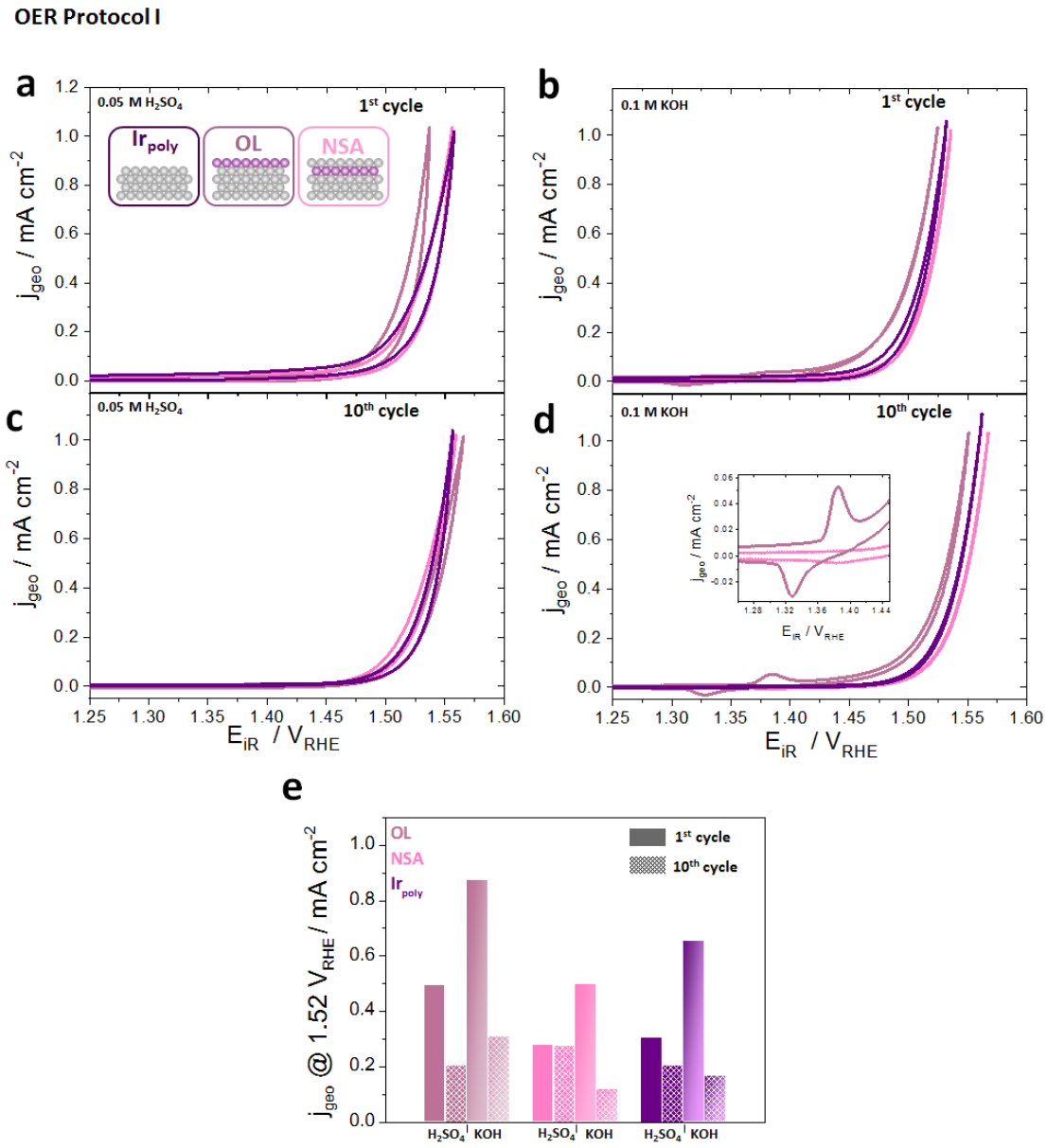

Figure 33 | Electrocatalytic oxygen evolution reaction (OER) activities of Ni-modified Ir electrodes compared to pristine polycrystalline Ir at scan rates of 5 mV s^{-1}. (a) 1st OER cycle in 0.05 M H_2SO_4 and (b) 1st cycle in 0.1 M KOH of Ir_{poly}, Ni/Ir_{poly} OL and Ni/Ir_{poly} NSA. (c) 10th OER cycle in 0.05 M H_2SO_4 and (d) 10th cycle in 0.1 M KOH of all catalysts. (e) Current densities of electrodes measured at 1.53 V_{RHE} normalized to the electrode's geometric surface area of 0.785 cm^{-2}.

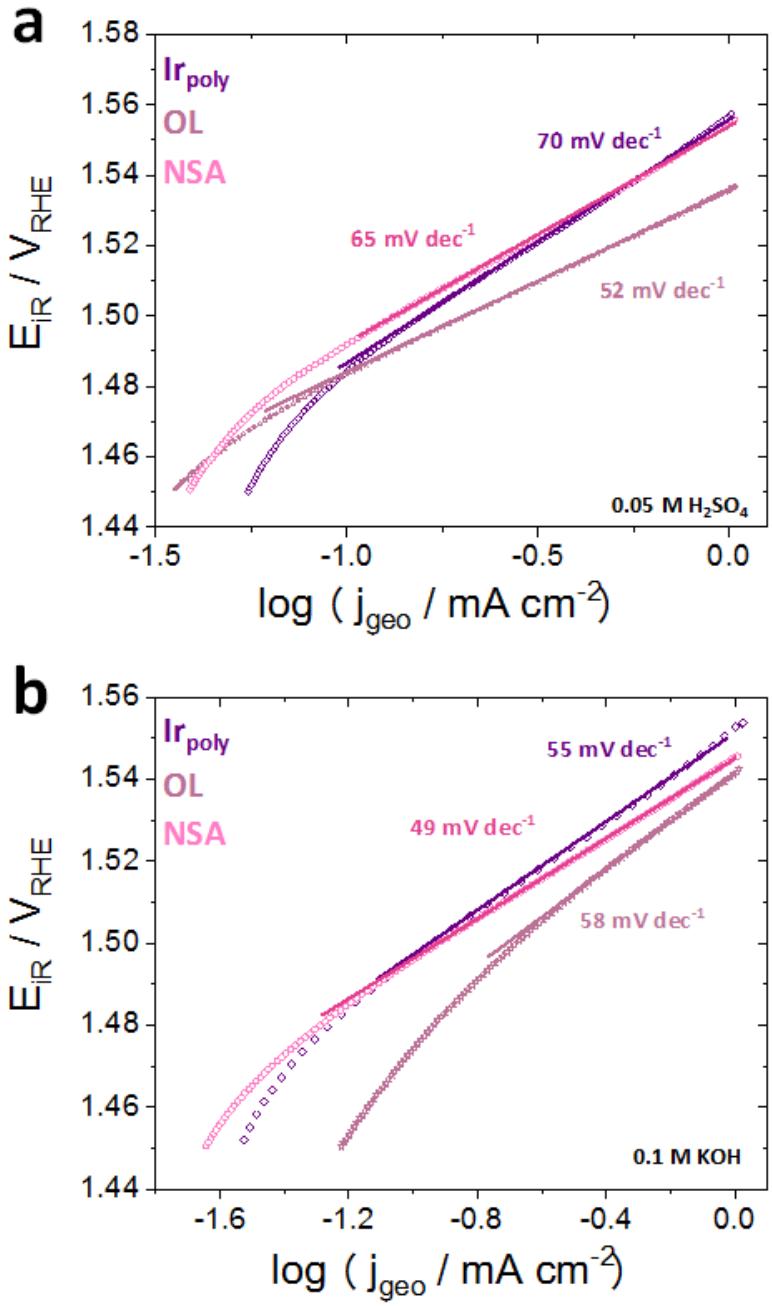

Figure 34| Tafel plots (with ohmic-drop correction) of the 1st cycle of Ir_{poly}, Ni/Ir_{poly} OL and Ni/Ir_{poly} NSA in (a) 0.1 M KOH and in (b) 0.05 M H_2SO_4.

The OER activity of polycrystalline Ir has been enhanced both in acidic and alkaline solution with the addition of Ni at the topmost layer (OL) using controlled-potential technique. Based on the significantly higher OER performance of the OL by contrast with the NSA and unmodified Ir electrode, the Ni/Ir_{poly} OL system was investigated in a second OER protocol. In Figure 35 OER polarization curves of two Ni OL catalyst systems are depicted in 0.1 M KOH. The

electrochemical performance of each sample was tested by 10 consecutive cycles. However, both samples differ in their electrochemical pretreatment. The Ni-modified Ir_{poly} electrode OL_{di} was tested in KOH directly after the process of Ni deposition. The electrochemical activity of the catalyst OL_{pr} was initially recorded in 0.05 M H_2SO_4 before it was transferred into the alkaline setup. For the OL_{di} catalyst, the characteristic $Ni(OH)_2$/NiOOH redox transition[138, 139] at ~ +1.35 V_{RHE} (see Figure 35b) is clearly visible and grows with increasing cycle number. A slight cathodic shift of the precatalytic $Ni^{2+/3+}$ redox wave is observed with increasing cycle number indicating a destabilization of Ni^{2+} under OER catalytic potential. The redox charge obtained by integration of the area under the cathodic wave from the last scan amounts to 137.15 µC (with consideration of geometric surface area) which is equivalent to 1.42 nmol redox active Ni atoms. Taking into consideration that the Ni amount determined by ICP-MS for deposition at 0.05 V RHE was 3.178 nmol (see section 6.3.2.2), this result would imply that not all Ni sites in the Ni/Ir_{poly} OL system contribute equally to the OER current. The pre-treated OL_{pr} catalyst shows no sign of a $Ni(OH)_2$/NiOOH redox peak, clearly confirming the instability of a Ni OL in acidic media. The characteristic redox peak of the OL_{di}, however, demonstrates the successful implementation of electrochemical deposition of Ni on polycrystalline Ir electrode and forms the basis of further atomic structure modifications. Interestingly, the prior OER treatment of the OL catalyst in sulfuric acid seems to activate the catalyst by ~ 31 %. The enhanced electrochemical property of the pre-treated catalyst might be deduced to an increased presence of electrophilic oxygen species[29, 31] Pfeifer *et al.* identified the reactive O^{I-} species by characteristic near-edge X-ray absorption fine structure (NEXAFS) features in Ir(III/IV) oxohydroxides. The dissolution of Ni adatoms along with the introduction of Ir vacancies in highly acidic solution and the accompanying formation of electronic defects in the cationic and anionic framework might lead to the formation of highly electrophilic oxygen atoms. As these oxygen atoms are highly susceptible to nucleophilic attack, they are suggested to facilitate the O-O bond formation, which is a key step during electrocatalytic OER. Another conclusion that can be drawn from the higher activity of the OL_{pr} catalyst is roughening of the surface by repetitive cycling.

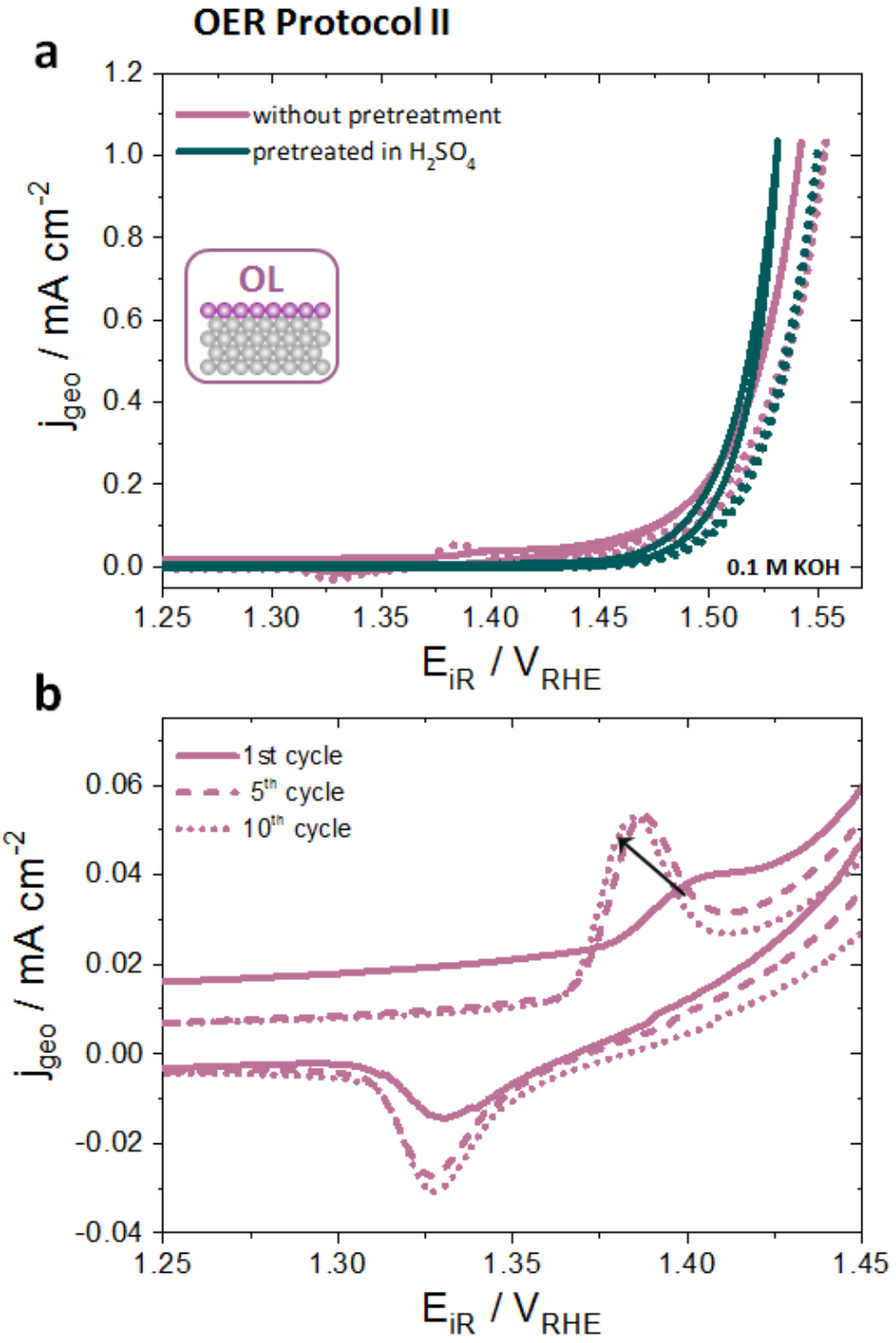

Figure 35 | (a) OER polarization curves of Ni/Ir_{poly} OL in N_2-saturated 0.1 M KOH without (lilac) and with (green) electrochemical OER pre-treatment in 0.05 M H_2SO_4. Scan rate v = 5 mV s^{-1}. First (solid lines) and 10th cycle (dotted lines) included. The overlayer (OL) was formed by electrodeposition of Ni at 0.05 V_{RHE} for 10 min. (b) Cathodic shift of the $Ni(OH)_2$/NiOOH redox peak of the OL implies destabilization of Ni^{2+}.

The selective leaching of a sacrificial component is a promising approach to design alloy systems with enhanced activity and stability towards the OER. In the work of Seitz *et al.* a highly active $IrO_x/SrIrO_3$ electrocatalyst was formed by leaching strontium in the near-surface during electrochemical testing from the surface of $SrIrO_3$ thin-films.[140] In comparison to known IrO_x catalyst materials, these IrO_x surface layers induced by Sr deficiencies showed significantly higher OER activities, supporting the theory of increasing active sites by selective leaching of sacrificial components from surface alloys.

The observed order of activity of the Ir_{poly} catalysts measured in KOH in the RDE setup could be confirmed with an electrochemical flow cell setup, which directly interfaced to a differentially pumped electrochemical mass spectrometer (DEMS). In Figure 36a, the OL system displays the highest measured current density at 1.56 V_{RHE} followed by Ir_{poly} and the NSA system, which are quite close to one another. The subsequent OER measurements in acidic solution slightly differ in the sequence of activity. These were measured directly after the catalysts were treated in alkaline solution. The unmodified polycrystal experiences a drastic loss in current density, the NSA catalyst system, however, offers a greater stability and activity compared to Ir_{poly}. The enhanced activity behavior of the NSA system was also observed in the 10^{th} cycle directly measured in acidic solution. In Figure 33e almost no activity loss is observed in acidic solution. Within the context of the measuring accuracy, the Faraday Efficiency (FE) of O_2 evolution reaches ~ 100 % for Ir_{poly} and for the OL catalyst in both electrolytes and in KOH, respectively. The FE over 100 % for the OL catalyst in acidic solution is significant and may be deduced to Ni dissolution in the highly corrosive environment, which simultaneously produces additional oxygen. For both Ni-modified NSA catalysts the FE amounts to ~ 104 % within the precision of measurement.

Notable differences in the characteristics of the Ni-modified catalysts are observed. Whereas the OL shows remarkable high activities in both acidic and alkaline milieu, the NSA catalyst demonstrates enhanced stability in acidic environment.

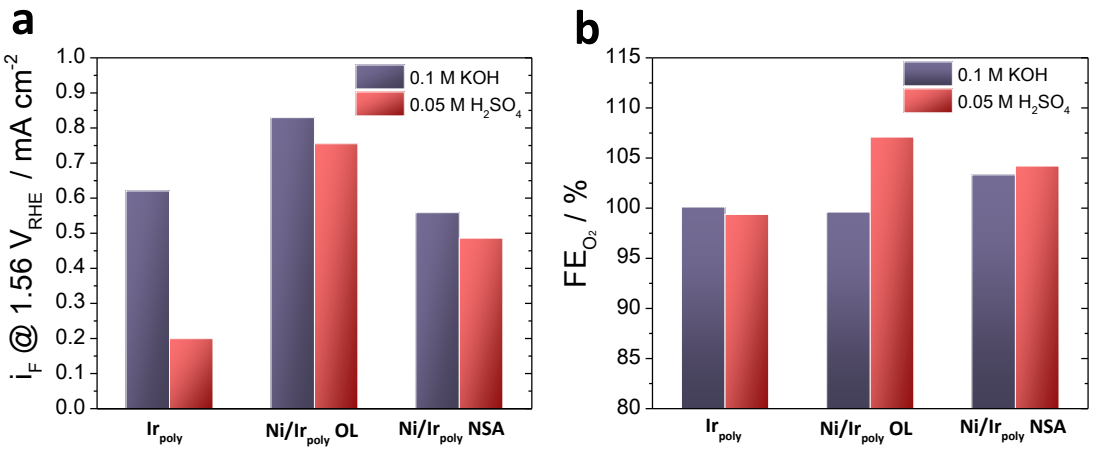

Figure 36| Electrocatalytic OER activities of Ni-modified electrocatalysts and pristine Ir_{poly} measured by differential electrochemical mass spectrometry (DEMS) in a dual-thin layer flow cell setup at a scan rate of 10 mVs^{-1}. (a) Faradaic current densities measured at an OER overpotential of 300 mV (1.53 V_{RHE}) normalized to the electrode's geometric surface area of 0.785 cm^{-2}. The electrocatalytic OER activity in H_2SO_4 was measured directly after the treatment in KOH. (b) Faraday efficiency of oxygen evolution (FE_{O_2}) determined for the catalysts.

6.3.4 Comparative Study of CO stripping Voltammetry on Ir_{poly} and Ni-modified Ir_{poly} Electrodes

The surface-sensitive electrochemical oxidation of adsorbed CO on pristine Ir_{poly} and Ni-modified Ir_{poly} electrodes have been studied in alkaline solution (0.1 M KOH) using stripping voltammetry. Here, the Ni/Ir_{poly} NSA catalyst was prepared by annealing the OL for only 1 min in the reductive atmosphere. Due to the reduced exposure to the reductive treatment the characteristic $Ni(OH)_2$/NiOOH feature is still visible in the cyclic voltammogram. The following study intends to assess and compare surface features of the three distinct catalyst electrodes, as CO oxidation is a process well-known to be dependent on the surface structure.[96, 141, 142] In this chapter, the CO oxidation mechanism is examined in alkaline electrolyte in order to integrate the Ni electrochemistry and to identify if CO adsorption is favored in the presence of Ni, as the (sub)surface layers of Ni on Ir have not been stable in acid environment. Furthermore, the concept of OER in alkaline media may be of interest from the catalytic point-of-view, as the pretreatment of the Ni/Ir_{poly} OL catalyst in H_2SO_4 seems to have a beneficial effect in the subsequent activity measurement in KOH (see section 6.3.3.1)

Figure 37 compares the anodic stripping voltammetry observed for a CO adlayer on the three distinct electrode surfaces in 0.1 M KOH solution at 50 mV s^{-1}, followed by the second sweep cycle between the potentials of 0.05 and 1.40 V_{RHE}. The presence of a CO surface adlayer can be confirmed as for each electrocatalyst a CO stripping peak was recorded. The voltammetric profiles further validate the complete electrooxidation of the adsorbed CO in the first anodic sweep, as the second cycle produces a voltammogram displaying HUPD peaks characteristic for Ir.

It can be noticed that there is a clear distinction between the Ni-modified electrocatalysts and the unmodified, pristine polycrystalline Ir electrocatalyst with regard to the stripping peak shape and position in Figure 37a. The Ni/Ir_{poly} OL and Ni/Ir_{poly} NSA electrodes produced a stripping peak at much lower potentials than the pure Ir_{poly}, which suggests that the oxidation of surface CO to CO_2 is promoted by the presence of Ni. In accordance with the enhanced CO oxidation of the Ni-modified catalysts, the onset of OH adsorption on the OL and NSA starts at more negative potentials than on pristine Ir_{poly}.[143] The oxidation of Ir sites is favored, or in other words, the adsorption of HO* (* denotes a free metallic site) is highly favored in the presence of Ni. An additional voltammetric feature of the CO-loaded Ir polycrystal is a broad peak at ~ +0.3 V_{RHE} (Figure 37a), which is only weakly defined for the OL and no longer present for the NSA. The possible origin of this peak will be discussed in the following.

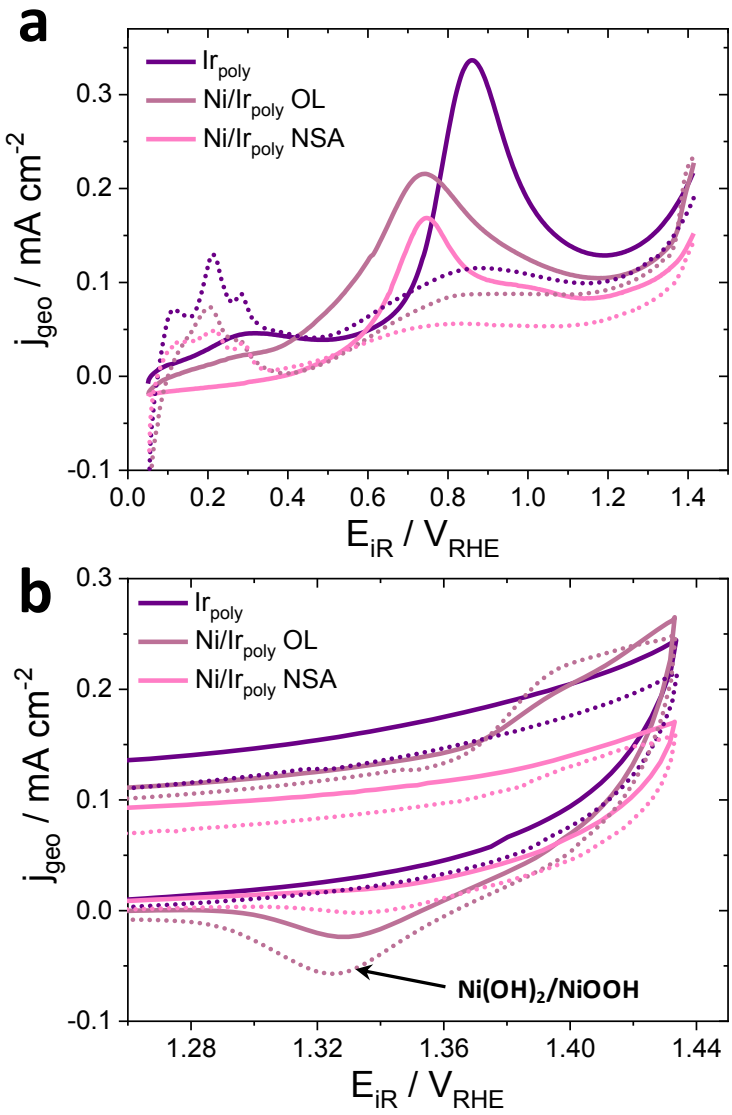

Figure 37| CO stripping (solid line) and the subsequent cyclic voltammogram (dotted line) for Ir_{poly}, Ni/Ir_{poly} OL and Ni/Ir_{poly} NSA measured in 0.1 M KOH. (a) anodic curves over the entire potential range and (b) anodic and cathodic curves in a potential range of 1.25 – 1.44 V_{RHE}.

To gain a quantitative understanding of the effect of Ni modification on the CO oxidation activity in alkaline electrolyte, the CO stripping profiles were deconvoluted into multiple peaks. In order to place hidden peaks, a linear background-correction was performed to the CO stripping peaks and subsequently the individual peaks were fitted. The respective CO stripping curves are presented in Figure 38 for Ir_{poly}, Ni/Ir_{poly} OL and Ni/Ir_{poly} NSA catalysts. All profiles can be sufficiently fitted by at least two peaks. The major component is centered at ~ +0.85 V_{RHE} for Ir_{poly} and is shifted towards more cathodic potentials for Ni/Ir_{poly} OL and Ni/Ir_{poly} NSA. The effect of a facilitated CO oxidation with respect to the

unmodified Ir_{poly} is quite likely due to a Ni richer surface, as has been observed in earlier studies.[141, 144, 145] The hypothesis is further reinforced by the fact that no Ni was removed by the CO stripping procedure, as the characteristic $Ni(OH)_2$/NiOOH redox couple was observed for both Ni-modified catalysts in Figure 37b after CO was stripped off the surface. The early onset of CO oxidation for the OL and NSA is initiated by highly hydrophilic Ni-rich areas, forming Ni(oxo)hydroxides, which further react with adsorbed CO on neighboring Ir sites as early as ~ 0.72 V_{RHE} for Ni/Ir_{poly} OL. The most likely reaction scheme to the CO oxidation process in alkaline solution can be assigned to a Langmuir-Hinshelwood mechanism involving the competitive adsorption of the reactants CO and OH[146]:

$$CO_{ads} + OH_{ads} \rightarrow COOH_{ads} \quad \textbf{(6.24)}$$

$$COOH_{ads} \rightarrow CO_2 + H^+ + e^- \quad \textbf{(6.25)}$$

The oxidative removal of adsorbed CO on Ir in the presence of Ni is presumed to proceed according to the following equations:

$$Ni_{ads} + H_2O \rightarrow Ni_{ads} \cdots OH_{ads} + H^+ + e^- \quad \textbf{(6.26)}$$

$$Ni_{ads} \cdots OH_{ads} + CO_{ads} \rightarrow Ni_{ads} + CO_2 + H^+ + e^- \quad \textbf{(6.27)}$$

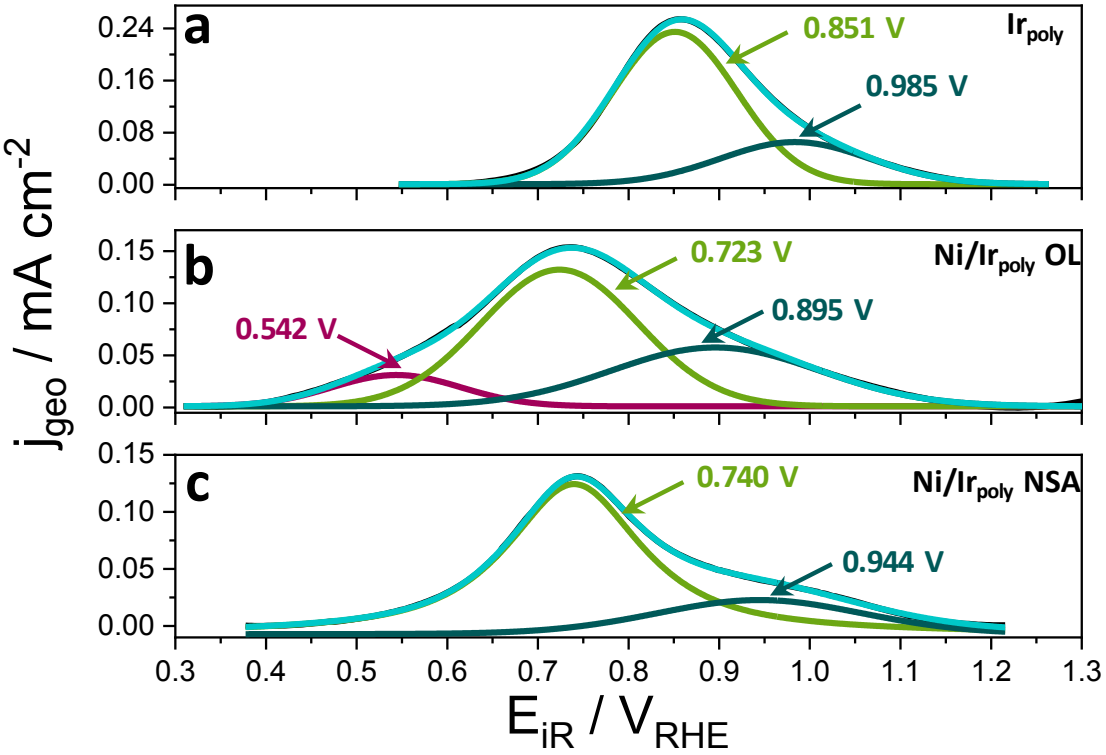

Figure 38| CO stripping curves for (a) the unmodified polycrystalline Ir electrode and the Ni modified (b) Ir_{poly} OL and (c) Ir_{poly} NSA catalysts obtained at 50 mV s^{-1} in N_2-saturated 0.1 M KOH (purified Fe free) at a rotation of 1000 rpm. Linear-background correction was performed through baseline subtraction for the anodic CO stripping voltammetry in Figure 37 between 0.4 and 1.2 V_{RHE}. The peaks were fit by Gauss functions and the individual contributions are shown in colors. The cumulative curve is given in turquoise.

In the CO stripping voltammetry of the pure Ir polycrystal in Figure 37a an anodic redox wave is visible at ~ +0.3 V_{RHE}. The origin of this peak cannot be adequately verified, however, a rather small "pre-peak" observed by Spendelow *et al.*[146] and García *et al.*[142] was attributed to oxidation of CO at step sites. In the study of the mechanism and kinetics of CO oxidation on stepped surfaces by *in situ* infrared spectroscopy, Lebedeva *et al.* found that the step trough is the most active site for CO oxidation.[147] After deposition of Ni, this peak is weakly identifiable, suggesting that Ni adatoms adsorb to some extent on Ir step sites. After annealing, however, the peak disappeared, probably due to healing of a majority of defect sites on the polycrystalline Ir surface.

The CO stripping peaks in Figure 38 all consist of a small peak or shoulder at higher potentials (dark green fit) arising very likely from the adsorption of HO*. Ir oxidation is prevented until the oxidative removal of adsorbed CO. On the

Ni-modified catalysts, OH adsorption is more favored and thereby shifted to lower potentials as discussed earlier. The main peak positioned at ~ +0.85 V_{RHE} for Ir_{poly}, ~ +0.72 V_{RHE} for Ni/Ir_{poly} OL and ~ +0.74 V_{RHE} for Ni/Ir_{poly} NSA can be attributed to CO oxidation at terrace sites of Ir.[148] Based on the fitted data, the cathodic shift of the CO stripping peak is slightly more pronounced for Ni/Ir_{poly} OL (~ +0.72 V_{RHE}) than for Ni/Ir_{poly} NSA (~ +0.74 V_{RHE}). This finding can be interpreted under consideration of the CO oxidation charge of both Ni-modified catalysts.

The CO stripping charge is frequently used to determine the electrochemical active surface area (ECSA), which is inevitable to assess the stability and activity properties of electrocatalytic materials.[141, 149-151] Hereto the baseline-corrected deconvoluted peaks (light green) were integrated for each individual catalyst. As expected, the net CO stripping charge of Ir_{poly} was found to be the highest with 803 µC cm^{-2}. The electrodeposition of Ni on the surface of Ir reduces the surface area available to CO, as Ir sites are blocked by Ni adatoms. A net charge of 569 µC cm^{-2} can be assigned to the OL catalyst. Interestingly, the CO charge for the NSA is slightly reduced to 529 µC cm^{-2}. However, in addition to purely geometric blocking, electronic effects due to the Ni atoms need to be taken into consideration as well, when discussing the CO coverages. As the outer layer of the NSA in this study consists of both Ir and Ni atoms, the lower CO coverage on the NSA, must be deduced to the modified electronic properties of the Ir surface atoms due to Ni atoms in the subsurface layer. A lowering of the chemisorption energy is the result leading to a weaker adsorbate binding. A similar behavior has been reported by Bandarenka *et al.* in the study of the CO oxidation on alloys of Cu/Pt(111).[96] It is thus feasible that the electronic effect of Ni in the subsurface region on Ir either has a negative effect to the oxidation of CO or does not compensate for the reduced amount of surface Ni atoms. Consequently, the peak position of the main CO stripping peak is not only a function of the pure composition but depends strongly on the specific position of the non-noble metal. Apparent from Figure 38b the CO stripping curve of the OL seems to consist of a second feature at ~ +0.54 V_{RHE}, which might be deduced to OH adsorption on Ni adatoms prior to the facilitated electrochemical oxidation of CO. Even after intense fitting, this rather small peak was not found on the NSA most likely due to the comparatively small amount of Ni surface atoms. However, the absence of this peak on the NSA system strengthens the observed higher activity of the OL towards CO oxidation.

In the foregoing discussion, a distinction between distinct active Ir sites has not been addressed yet. The behavior of hydrogen on the polycrystalline Ir surface, however, may provide important information on the deposition process of Ni. In Figure 37a there are three distinct redox features in the anodic branch of the HUPD region of the pristine Ir_{poly} in the second scan after the complete oxidation of adsorbed CO. These redox peaks indicate distinct Ir sites at which oxidation of UPD hydrogen occurs. The well-defined HUPD peaks can be assigned to the three low-index crystallographic facets (111), (110) and (100) of Ir.

A thorough theoretical study of the adsorption/deposition of hydrogen on various close-packed facets of noble and non-noble metals, including the face-centered cubic (fcc) facets of Ir(111), Ir(110) and Ir(100) was performed in collaboration with the group of Mavrikakis as described in 6.2.2.4. The energetically most favored adsorption sites for Ir(111) and Ir(100) were adopted by Ferrin *et al.*[152] The binding energies (BE) for the three distinct low-index surfaces along with the coordination numbers (CN) of surface Ir atoms and calculated geometries for surface hydrogen (Site) are given in Table 5. The binding energies are calculated relative to the hydrogen atom in the gas phase. The computational details reveal that the Ir(100) surface (-2.91 eV) binds hydrogen the strongest, followed by Ir(111) (-2.73 eV) and Ir(110) (-2.70 eV). Based on these calculations the Ir(100) binds hydrogen ~ 0.20 eV more strongly than the Ir(111) and (110) surfaces. The difference in binding energy between those facets can be deduced to the hydrogen-metal bond distances and binding geometries. It has been reported that for Ir(111) and Ir(110) hydrogen adsorption on top site[153, 154] is favored, while on Ir(100) the bridge site[155] is more favorable in energy terms. Due to the distinct geometries of the adsorption configuration for surface hydrogen, the H-Ir bond distance on (100) is larger (1.81 Å) than on (111) (1.59 Å) and (110) (1.62 Å). Assigning the distinct HUPD peaks to the three low-index surfaces, the most preferred Ni adsorption sites might be deduced. As the HUPD peak attributed to the (110) sites is significantly reduced by forming an overlayer of Ni, it appears that Ni adsorbs rather on (110) sites and that (100) sites are less favored. For the NSA catalyst system, the (110) peak is slightly visible whereas the (100) is more pronounced due to Ni in the subsurface layers. Interestingly, the HUPD charge is the lowest for the NSA catalyst (0.10 mC cm^{-2}). For pristine Ir_{poly} and Ni/ Ir_{poly} OL the HUPD charge was determined to 0.20 mC cm^{-2} and 0.13 mC cm^{-2}, respectively. The given order was also observed for the CO charge and might provide important indications on the activity of the Ni-modified catalysts.

The smaller HUPD charge of the NSA catalyst in comparison to the system in which Ni is present at the surface, might be set into relation with its lower activity performance towards catalyzing oxygen evolution.

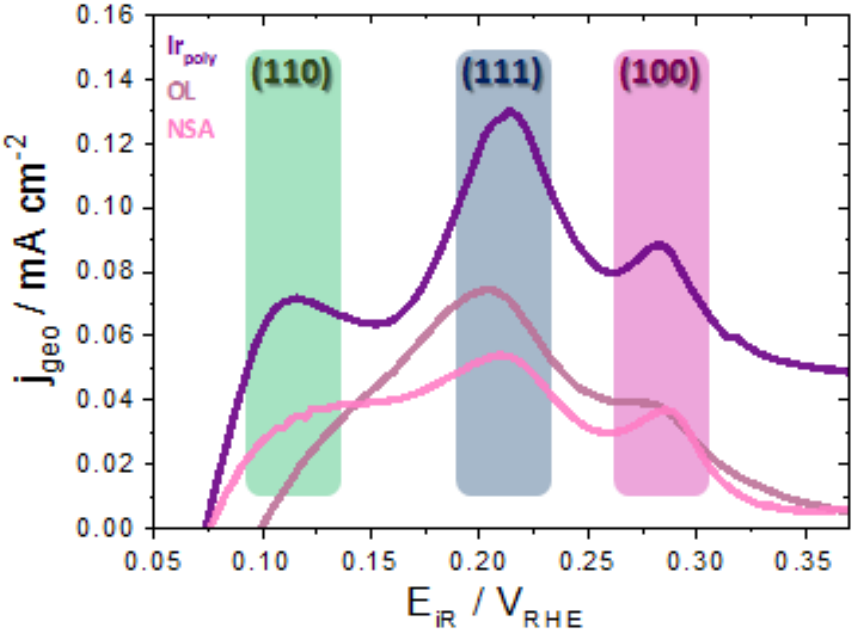

Figure 39| The second cycle of the CO stripping CV displaying the HUPD peaks of the three distinct catalyst systems. The allocation of the HUPD peaks is made based on DFT calculations of the hydrogen binding energy on the three low-index surfaces (111), (110) and (100) of Ir.

Table 5| DFT-calculated Binding energies of hydrogen and H-Ir bond distances on the three low-index surfaces of Ir.

	CN	*Site*	*BE / eV*	*H-Ir bond distance / pm*
(100)	6	bridging	-2.91	2×181
(111)	9	atop	-2.73	159
(110)	7	atop	-2.70	162

Chapter 7 Surface Electrochemistry and Catalysis of Spin-Coated, Thermally Reduced Iridium Thin-Films

This chapter is predominantly based on the following publication:

E. Özer, Z. Pawolek, S. Kühl, H. N. Nong, B. Paul, S. Selve, C. Spöri, C. Bernitzky and P. Strasser, *Surfaces* **2018**, *1*(1), 155 (DOI: https://doi.org/10.3390/surfaces1010012).

The electrochemical processes during electrocatalysis are highly sensitive to the surface geometric and electronic properties of the catalyst and its interaction with the substrate. The junction of the catalyst with the substrate affects the performance of electrode to a great extent. Improved fundamental understanding of the OER catalysis is possible on defined smooth model surfaces. Insights obtained from such studies aid in our understanding of the OER catalysis on more complex surfaces.

A suitable model system to study structural, compositional and electronic effects of Ir based bimetallic catalysts on their OER activity and stability are homogenous thin-films on Ti substrates with a defined film thickness and compositional and structural homogeneity. The thin-film approach builds on the single-crystal approach outlined in earlier chapters. It studies the effects of distinct facets and surface–specific structural designs on the OER catalysis, yet it also allows for more flexibility and variation in catalyst composition design and synthesis procedures.

Ir-containing homogenous metal and metal oxide thin–films have been successfully employed as model catalysts with a focus on material properties and catalyst substrate interactions.[32, 33] These model studies can make essential contributions uncovering activity and stability constraints for future optimization of existing OER catalysts. Compositionally homogenous thin–films with well–defined thickness emphasizes the focal point to be on the catalyst's intrinsic reactivity as mass transport effects caused, for instance, by a loss of reactants can be left unconsidered. Ir thin film model catalysts attract a greater variety of surface sensitive analytical techniques to correlate surface characteristics with their catalytic properties during the OER.

7.1 Experimental Part

7.1.1 Ti Cylinders

For the deposition of Ir thin-films, Ti cylinders with a height of 4 mm and a diameter of 10 mm were used as substrates. Suitable Ti rods (Gemmel, grade 1 or Chempur, 99.6 %) were cut accordingly. Prior to deposition, the cylinders were grinded and polished consecutively in a half-automatic polishing machine (AutoMet 250, Buehler) using a custom–made sample holder with drop–shaped holes. To guarantee that all cylinders were mounted with the same altitude, a height adjustment tool, especially manufactured for that purpose, was applied. In a first step the sample holder was placed on and then screw–tightened to the height adjustment tool. Thereafter, the cylinders were integrated into the sample holder's holes and tightened in that position with grub screws. The settings for grinding and polishing eight Ti cylinders to a mirror–like surface are given in Table 6. In the grinding step, machining marks from the cutting process are removed from the surfaces. The following two polishing steps are repeated consecutively until the desired surface finish is achieved. The grinding and polishing step is then followed by sonication of the cylinders in distilled water to clear the surface of polishing residues. In a last step, the cylinders need to be treated in hot (~150 °C, 2 h) nitric acid (23 %, prepared by dilution of 69 % HNO_3, AnalaR Normapur) to remove (mainly iron) impurities originating from the Ti rods. Finally, the cylinders are consecutively cleaned in water, acetone and again in water in ultrasonic bath.

Table 6| Polishing procedure for a mirror-like surface finish of Ti cylinders with a half-automatic polishing machine.

	Step 1: grinding	*Step 2: polishing*	*Step 3: polishing*
polishing cloth	SiC grinding paper P320	UltraPad	MicroCloth
polishing agent	water	MetaDi Supreme 9 µm	MasterMet 2 0.02 µm
rotation *base / rpm* *head / rpm*	complimentary 200 60	contra 150 30	contra 150 30
Force / N	40	50	40
time / min	1	10	10

7.1.2 Preparation Procedure of Electrode Materials

Ir metal thin-films on Ti substrate were prepared according to the synthesis procedure schematically shown in Figure 40. In a first step, homogenous thin Ir acetate films were deposited onto the substrate via spin coating (WS-650MZ--23NPP, Laurell) according to a previous reported procedure.[33, 118] The deposited acetate films were then either reduced directly by inductive heating (Ac samples) or calcined in air prior to the reduction step (Ox samples).

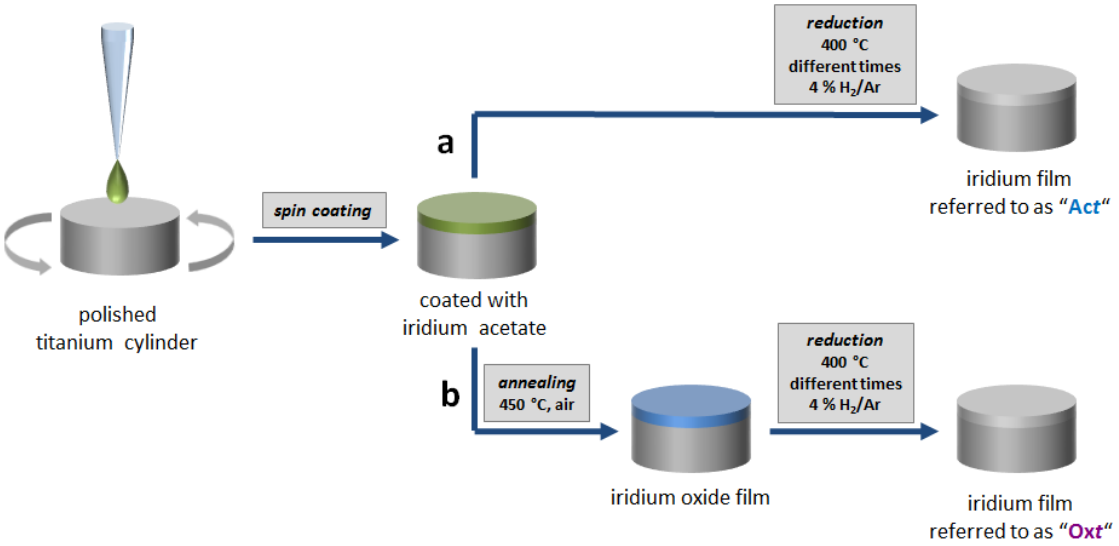

Figure 40| Schematic representation of the synthesis procedure for the preparation of Ir metal thin-film catalysts on Ti substrate using two different synthesis approaches. The upper line (a) refers to the synthesis of the directly reduced Ac samples. The lower route (b) corresponds to the synthesis of the Ox samples. In one additional step, the Ir acetate film is annealed in air prior to reductive heating. The sample names of each series will include the time 't' as Ox't' and Ac't'.

7.1.2.1 Spin coating procedure for preparation of thin precursor films

For the preparation of thin precursor films, the Ti cylinders were inserted into a tapered ring and then pressed into a custom–made sample holder made from polyoxymethylene (POM). This step must be executed properly due to the large acceleration and high rotational velocities during the spin coating process. An adapter was applied to the back of the sample holder to ensure a firm attachment of the holder to the spin coater during vacuum application. During rotation of the Ti substrate at 200 revolutions per minute (rpm), approximately 40 µl of the coating solution is applied onto the substrate. The coating solution is prepared by dissolving Ir acetate (80 g l^{-1}, ~ 0.2 mol Ir l^{-1}, Chempur, 99.95 %) in ethanol (abs., AnalaR

Normapur) by ultrasonication. Possible undissolved residues need to be removed by filtration through a syringe filter (Nylon, 0.2 µm). After 45 s at a rotational velocity of 2000 rpm, the Ti substrate is removed from the spin coating holder by applying force to the back of the cylinder. For accuracy, the loading of Ir was determined by inductively coupled plasma atomic emission spectroscopy (ICP-OES). Hereto, the spin–coated acetate films were dissolved in water.

7.1.2.2 Preparation of metallic Ir films

At this point two different synthesis routes were pursued to obtain the metallic Ir films. In the direct reduction route (Figure 40a) the films are directly reduced from the acetate in a custom–made inductive setup in 4 % H_2/Ar at 400 °C. The design and operational principles about the inductive electrochemical chamber are given in Chapter 5. In the oxide route (Figure 40b), the acetate films are initially calcined in a pre-heated Muffel furnace (Carbolite) at 450°C for 15 min in air prior to reduction. Samples will be referred to as A*ct* (samples reduced directly from the acetate) and Ox*t* (samples reduced from the oxide), where *t* is replaced by the time (in min) the sample was exposed to the reductive atmosphere in the inductive cell.

7.1.3 Physico-chemical Characterization

7.1.3.1 Inductively Coupled Plasma Atomic Emission Spectroscopy (ICP-OES)

The loading of Ir was determined with a Varian 715-ES ICP ICP-OES. Hereto a coated, however, non-calcined cylinder was introduced in 12 ml milli-q water. The ICP-tube was briefly shook before the cylinder was removed. The ICP-tube was weighed before and after it was filled with milli-q water.

7.1.3.2 Scanning Electron Microscopy (SEM) and Energy Dispersive X–ray Spectroscopy (EDX)

Scanning electron microscopy (SEM) images were obtained using a JEOL 7401F field emission scanning electron microscope with an accelerating voltage of 10 kV. The obtained images were edited using the software ImageJ. Corresponding EDX analysis was established by a Bruker XFLASH 4010 at an accelerating voltage of 6 keV. The instrument is equipped with an EDX detector (Quantax 400, Bruker). If not stated otherwise, the EDX was normalized by the sample current, which was collected in a Faraday cup.[156] The Faraday cup, which resembles an enclosed cavity

with a small opening is basically a metallic cup. Before and after each sample measurement, the Faraday cup is placed into the electron beam and electrically connected to the sample stage. The Faraday cup enables a precise measurement of the focused beam current at the target (which enters the cup through the small opening) as primary, backscattered and secondary electrons are all absorbed in the cup and prevented from escaping. An accurate determination of the concentration will be best achieved when normalizing the line intensities for each element by the captured charge densities (electron beam current × time). The loss of Ir during stability measurement was specified by quantitative analysis of the same catalyst before and after stability testing.

7.1.3.3 X-Ray Diffraction (XRD)

XRD patterns were obtained by grazing-incident X-ray diffraction (GIXRD) measurement in a Bruker D8 Advance diffractometer (Bruker AXS). The analysis was performed at a grazing incidence of 1° with a Goebel mirror, a Cu Kα source, a 0.23° secondary Soller and a scintillation counter as detector. The identification of the individual phases in the measured diffractograms was enabled with reference patterns. Rietveld refinement with the software TOPAS (Bruker AXS) allowed a clear definition of the individual phases present in the sample. A quantitative analysis, however, is not given with Rietveld refinement as it is primarily aimed at examining powder samples. The structure and composition of film samples do thus not allow an exact determination of concentrations as the individual phases might occupy distant layers, which consequently have an affect the intensity of the incident beam.

7.1.3.4 Transmission Electron Microscopy (TEM) and Selected Area Electron Diffraction (SAED)

For transmission electron microscopy (TEM) Cu grids with a holey carbon layer and 200 mesh by Quantifoil were coated with the dispersed catalyst. The measurements were performed at a FEI Tecnai G²20 S-TWIN transmission electron microscope with a LaB_6 cathode operated at an accelerating voltage of 200 kV. The SAED evaluation was performed by PASAD[157, 158] plugin in Digital Micrograph™, the obtained reciprocal distances were transferred to Cu Kα scale to obtain a calculated diffraction pattern.

For the investigation of a cross-section of Ir film on Ti, a TEM lamella was prepared by Focussed Ion Beam (FIB). A FEI Helios NanoLab 600 workstation equipped with (1) an Omniprobe lift-out system, (2) a Pt & W gas injector system, and (3) a scanning electron microscope (SEM) detector was used. High resolution TEM (HRTEM) was performed using a FEI Titan 80-300 TEM electron microscope with a high brightness X-FEG electron source and a Cs corrector for the objective lens. The microscope was operated at 200 kV.

7.1.3.5 X-Ray Photoelectron Spectroscopy (XPS)

Laboratory-based X-ray photoelectron spectroscopy (XPS) measurements were carried out at room temperature in an ultrahigh vacuum (UHV) setup using a monochromatic Al Kα source at 1486.6 eV. The XP spectra were analyzed using Casa XPS software. All spectra were charge-corrected with respect to the main peak in the C1s spectrum for adventitious carbon in the corresponding sample which was assigned to have a binding energy of 284.8 eV.[159]

7.1.4 Electrochemical Characterization

7.1.4.1 Activity, Stability and Faraday Efficiency Measurements

Electrochemical activity and stability measurements were performed in a rotating disk electrode (RDE) setup at room temperature in 0.05 M H_2SO_4 (diluted from 95 % H_2SO_4, Suprapure, Carl Roth) using a potentiostat (SP-240, BioLogic, France) and a common three–compartment electrochemical glass cell. A platinum mesh was used as counter electrode and a mercury/mercury sulfate electrode (MMS, sat., calibrated against RHE) as reference electrode. All potentials were converted into RHE scale (referred to as V_{RHE}). Nitrogen was used for degassing.

A silver/silver chloride electrode (Ag/AgCl, 3 M, calibrated against RHE) was employed as reference for Faraday efficiency (FE) measurements. These measurements were conducted in a custom–made electrochemical glass cell. The detailed descriptions can be found elsewhere.

To test the performance of the catalysts in the oxygen evolution reaction (OER), the electrodes were immersed in the electrolyte at a potential of 0.4 V_{RHE}. Subsequently cyclic voltammetry was performed in different ranges below the OER onset for surface characterization. The lower turning potential was 0.05 V_{RHE}, the upper turning potential was consecutively raised from 0.8 to 1.2 V_{RHE} in 0.2 V steps

(5 cycles each), followed by 50 cycles between 0.05 and 1.4 V_{RHE} for electrochemical oxidation and activation of the catalyst. After each 10th cycle of the latter, 3 cycles in a range of 0.4 to 1.4 V_{RHE} were performed to obtain the pseudo-capacitive charge (anodic charge q*). The rotation of the RDE was switched on to 1600 rpm and chronoamperometric steps were performed for 15 min at different potentials between 1.534 and 1.784 V_{RHE} (stepped potential voltammetry, SPV). At each potential, electrochemical impedance spectroscopy (PEIS) was measured to obtain the ohmic resistance. After degassing, the rotation of the RDE was turned off, and again 3 cycles in the anodic potential range of 0.4 to 1.4 V_{RHE} were conducted. The protocol was performed twice.

For electrochemical stability testing, the SPV in the OER protocol was replaced by one long chronoamperometry at circa 1.734 V_{RHE} (without correction of ohmic resistance) for 20 h. For FE testing, the first run of the OER protocol was performed in 0.05 M H_2SO_4. In the second run, the electrolyte was changed to 0.05 M H_2SO_4 including 0.01 M NaCl. A gas tight cell was used; the amount of produced oxygen was measured by mass spectrometry (Thermostar) of the continuously degassed electrolyte.

7.2 Physico-chemical Material Characterization

7.2.1 Morphology of Ir Metal Thin-Film Catalysts

7.2.1.1 SEM

In order to investigate the morphology of the Ox and Ac films, micrographs of the samples before (_AP) and after OER (_OER) as well as after Faraday efficiency measurements towards the OER (_FE) were obtained using a scanning electron microscope (SEM). The respective results are displayed in Figure 41 and Figure A6 (in the Appendix).

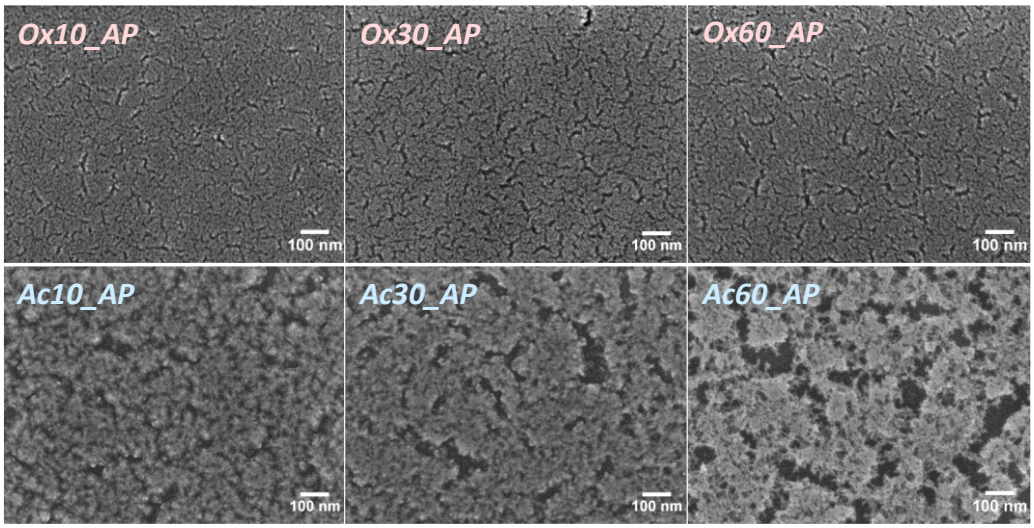

Figure 41| SEM images of Ox_AP (top) and Ac_AP (bottom) film series before OER and Faraday efficiency measurements. The weakly cracked morphology of the Ox films does not show any change in dependence of heating time. The cracks in the Ac films enlarge with increasing heating time.

The Ox_AP films (Figure 41, 1st row) display a homogeneously cracked surface with clear porosity. Their morphology (Ox10, Ox30 and Ox60) does not change significantly with heating time in contrast to the morphology of the Ac_AP film series. The surface of the Ac films (Figure 41, 2nd row) displays larger cracks compared to the Ox films, and in addition they exhibit a larger crack size distribution. Thus, a clear tendency towards a more cracked surface with longer annealing time was observed for the Ac_AP films. The morphological restructuring (and probable sintering process) produces a highly cracked, 'sponge-like' and more fibrous morphology. It can be assumed that in contrast to the Ac samples the calcination step in the Ox route creates a defined and crystalline rutile structure[33] from the beginning, which consequently leads to a faster formation of the final

metallic Ir structure through reductive heating. After OER and Faraday efficiency measurements the Ac_OER and Ac_FE samples exhibit a swollen and filled surface with rounded edges on the cracks. A similar effect is only weakly visible for the Ox films due to their less pronounced cracks (see Figure A6 in the Appendix).

7.2.1.2 Film Composition / EDX

EDX measurements performed of the _AP samples during SEM investigation in Figure S1 (in the Supplementary Information) show the atomic percentage (at%) ratio of O to Ir (not normalized by sample current) in dependence of heating time. The results reveal a significantly higher amount of O in the Ox samples than in the Ac samples, regardless of the heating time. This indicates the presence of an O species in the Ox films that cannot be removed by reductive heating under applied conditions or occurs while handling the samples under air, respectively. This species might either originate from a small fraction of (re)oxidized Ir in the film, physically adsorbed or trapped O within the pores of the film, or, most likely, a Ti oxide layer formed during the calcination step[33] and not being reduced at applied reduction conditions.

The position of O within the film, however, cannot be obtained by a single EDX measurement. For this purpose, several EDX measurements have been conducted along the radius of an Ox10_AP sample and IrO_x film on Ti (before reductive heating). The results are given in Figure 42. Here, the intensity (standardized to the sample current and time) of each element (left y–axis) along with the calculated O/Ir count ratio (right y-axis) is plotted against the radius of the film. Within a radius of 3.5 mm from the center, both samples show no variation in film thickness. Closer to the edge, the film thickness alters due to surface tension/boundary effects of the precursor solution during the spin coating process. The uneven film thickness at the edge of the sample and the ability of Ir to partially shield radiation emitted from deeper layers at least may give a hint on the oxygen distribution, considering two extreme cases. If oxygen was (exclusively) homogeneously distributed within the Ir(oxide) film (regardless of the chemical nature of O), the O/Ir ratio would be independent of the film thickness. In other words, at spots with lower Ir counts (= lower film thickness), the O counts should also be lower. If oxygen only existed within a Ti oxide layer underneath the film, the O/Ir ratio would increase with decreasing film thickness due to lower shielding by Ir. With respect to the IrO_x film on Ti (Figure 42a) both cases seem to apply here: a lower amount of Ir accompanied

by a lower amount of O (lower film thickness, 3.6 and 4.3 mm from center) points to an oxidized Ir film. At the same time, a higher O/Ir ratio speaks for a Ti oxide or Ir/Ti mixed oxide layer underneath the Ir oxide film. The homogenous part of the Ox10_AP film (Figure 42b) exhibits a drastically lower O/Ir ratio compared to the oxide film (Figure 42a), so a considerable amount of O has been removed from the sample by reductive heating. Even though inductive heating has reduced the film successfully, the location of remaining O has not changed during reduction: areas with a lower Ir amount in Figure 42b (lower film thickness, 4.4 mm) exhibit a larger O/Ir count ratio, indicating a significant amount of O beneath the film incorporated within a TiO_x or Ir-Ti mixed oxide layer. At areas with higher Ir amount (3.6 mm), the O total counts increases with Ir, pointing to a fraction of O existing inside the film. However, the metallic state of the as-prepared film, which was confirmed by XPS (as discussed later), excludes that O is chemically bound to Ir.

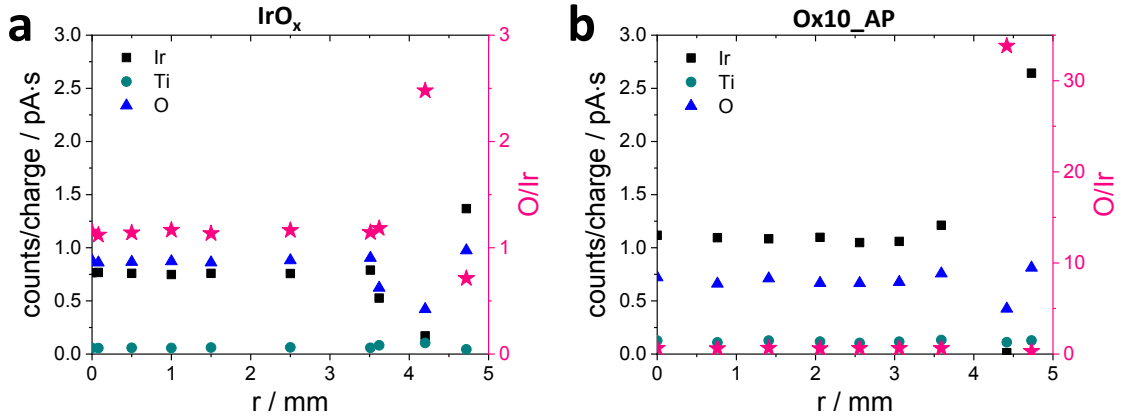

Figure 42| Counts per charge of the three main elements detected in EDX of (a) an IrO_x and (b) an Ox10_AP film. The different intensities are caused by different film thicknesses mainly due to by border effects during spin coating.

7.2.2 Structural Characterization of Ir Metal Thin-Film Catalysts

7.2.2.1 X-ray Diffraction

To examine if the crystallinity and atomic structure of the Ac and Ox films changes in dependence of reduction time, grazing-incident X-ray diffraction (GIXRD) analysis was conducted prior to OER measurements (see Figure 43). For both preparation methods, two crystalline phases are detected in the as-prepared state, where the dominating reflections (2θ: 35 ° and 40 °, purple sphere) can be assigned to the hexagonal phase of the Ti substrate. The weak reflections (2θ: 47 ° and 68 °, red star), however, are assigned to metallic Ir phases evidencing

crystallinity of the films. The low intensity of the reflections is a result of a low amount of Ir or rather a low thickness of the film in contrast to the bulk Ti cylinder.

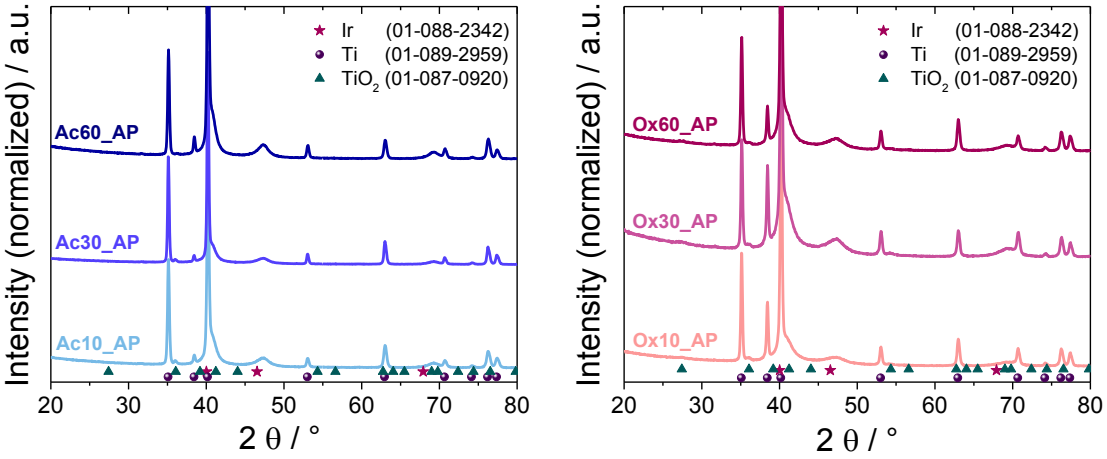

Figure 43| X-ray diffraction (XRD) of _AP (a) Ac and (b) Ox films show no major changes in the crystal structure in dependence of heating time. The large reflections can be attributed to the rutile phase of Ti.

Rietveld refinement technique was used to analyze the XRD patterns of the as-prepared samples. Selected results for the _AP Ox10 and Ac10 samples are shown in Figure 44 The analysis evidences the absence of a crystalline IrO_2 phase but suggests the presence of a TiO_2 rutile phase in a very small extent. Still, the existence of an amorphous or very nanocrystalline Ir oxide phase cannot be ruled out. To achieve a reasonable Rietveld refinement, an additional hexagonal phase had to be incorporated into the pattern fitting. The fittings further incorporate a metallic Ti phase and a nanocrystalline phase of metallic Ir. This supplementary reflection will be referred to as TiO_x and can be assigned to a Ti phase with larger lattice spacing rather than a rutile-type TiO_2. The presence of this phase might be deduced due to inclusion of oxygen into the lattice of Ti prior to the annealing process. The Rietveld refinement results for all other samples are given in Figure **A8**a and b in the Appendix.

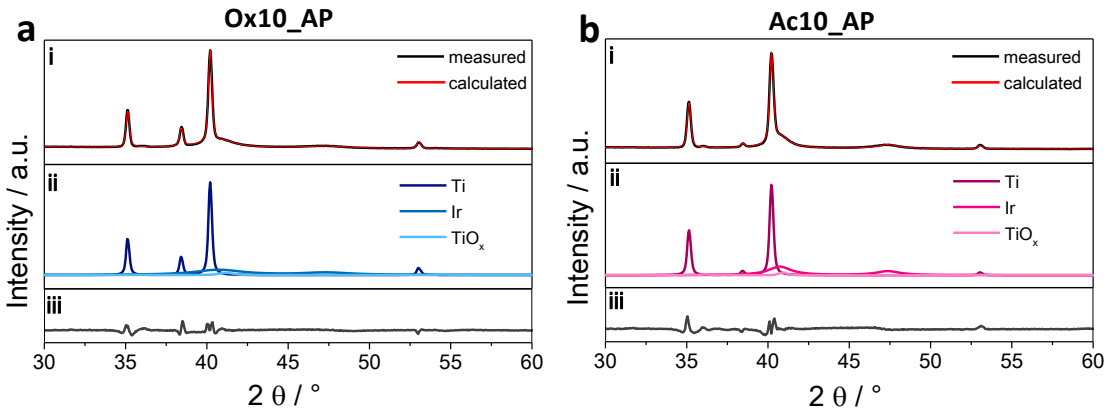

Figure 44| Grazing incidence X-ray diffraction measurements of (a) Ox10_AP and (b) Ac10_AP on Ti substrate including the results from Rietveld refinement. (i) Measured and calculated diffraction pattern, (ii) the individual phases that contributed to the refinement and (iii) difference pattern between the measured and calculated pattern.

7.2.2.2 SAED

To investigate the structure of the films at the nanoscale, selected area electron diffraction (SAED) was performed on the Ac_AP and Ox_AP catalyst films, as well as on the electrochemically treated Ac10_OER and Ox10_OER samples. The SAED patterns are given in Figure A9 (in the Appendix) and the corresponding calculated diffraction patterns (Cu Kα scale) are shown in Figure 45a-d and were made from dispersion of scraped off films. The reciprocal diffraction patterns were converted back into a diffraction pattern on the Cu scale. For the calcined IrOx film (prior to any reductive treatment), the clear diffraction pattern reveals a rutile-type phase corresponding to IrO_2 (see Figure A10 in the Appendix). According to SAED, after 10 min heating in the reducing atmosphere at 400 °C the rutile-type reflections are replaced by a metallic Ir phase (Figure 45a) which is still present upon cycling into OER potential regions (Figure 45c). The same applies for the Ac10 catalyst, where the evaluation of the internal order of the catalyst films confirms no IrO_x phase at several positions of Ac10 as well as Ac10_OER after polarization into OER potential regions. Accordingly, SAED evaluation conclusively confirms that all investigated films are consistently metallic and that the oxidation observed by XPS analysis (section 0) is limited to near-surface Ir. Furthermore, the morphology of the thin-films was selectively studied on a FIB-prepared TEM cross section of sample of Ac10. The resulting images are displayed in Figure 45e and f. After 10 min of heating in the reducing atmosphere, the catalyst film including the crystalline particles and the amorphous layer is about 10 nm thick. The high resolution TEM

(HRTEM) images reveal the presence of an amorphous interlayer between the crystalline Ti substrate and crystalline Ir particles. The particles, which are believed to be caused by cracking of the film, cover the amorphous layer unevenly. These particles have also been found in the TEM images of the scraped film (see Figure **A11** in the Appendix).

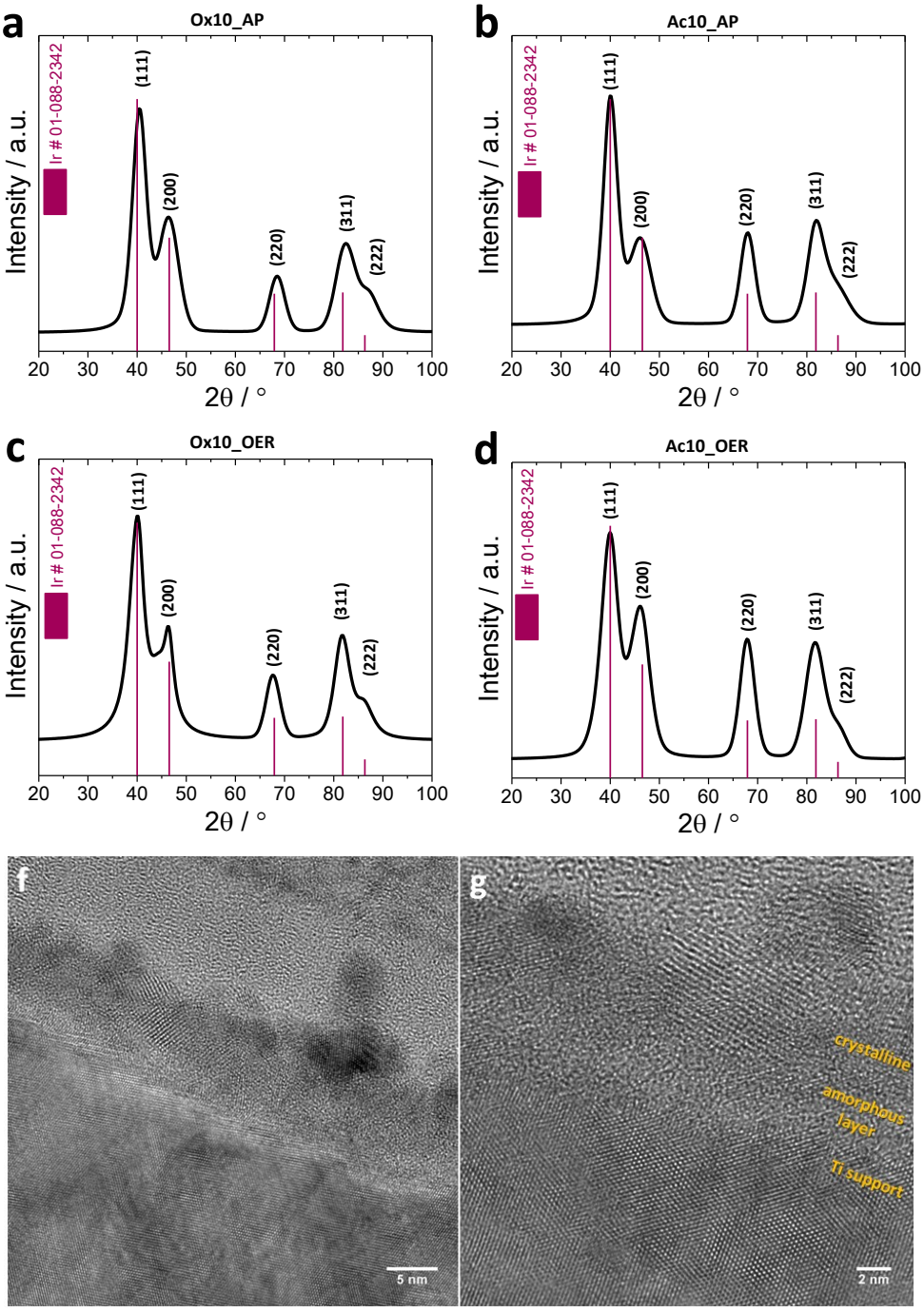

Figure 45 | (a-d) Calculated X-ray diffraction pattern of scraped off Ox10 and Ac10 films before (1st row) and after electrochemical OER testing (2nd row) only show metallic Ir. (e, f) TEM cross section of the as-prepared Ac10 film show crystalline Ir particles on an amorphous interlayer.

7.2.3 Surface Electrochemical Characterization

7.2.3.1 Anodic Charge and Cyclic Voltammetry

The cyclic voltammograms depicted in Figure 46 reflect the electrochemical processes taking place on the Ac and Ox films, just before the catalysts were being exposed to OER potentials. The respective surface voltammetric curves between 0.05 and 1.4 V_{RHE} of the Ac and Ox films prior to OER are presented in Figure A12 (pre-OER). For comparison, the surface CV scans after OER activity measurements are also given. In Figure 46b and c the currents were normalized to the anodic charge q*, also referred to as pseudo-capacitive charge, to account for comparable current densities within the given sample series. Trasatti[160-162] defined the anodic charge as a relative measure of the electrochemical active Ir oxide surface species. Hence, q* was collected in the potential area of 0.4 – 1.4 V_{RHE} (at 50 mV s^{-1}) after every tenth cycle of a complete surface layer scan from 0.05 to 1.4 V_{RHE}. The anodic charge values given in Figure 46a clearly show significant differences between Ac and Ox samples and distinctions within a synthesis route as a function of reduction time.

In Figure 46a there is a discernible and general trend to higher anodic charges with lower reduction time for both Ac and Ox samples. The longer heating period seems to create a film with greater crystallinity, which subsequently needs more time to become amorphous. This behavior is far more pronounced for the Ac films, supporting the thesis that the conditions under which the Ac samples have been inductively treated did not result in a final (metallic) structure. Thus, the Ac films are more sensitive towards the electrochemical treatment than the Ox films whose q* values do not differ significantly from each other. The Ac10 film catalyst offers by far the highest values of q* with a considerable increase during cycling between hydrogen and oxygen evolution reaction potentials. As the contribution of Ti oxide to the pseudo-capacitive charge is limited, the trends of q* provide a useful first indication of the Ir films' intrinsic reactivity.

The cyclic voltammograms of the inductively reduced Ac and Ox films in Figure **46**b and c show a strong similarity in their voltammetric features of the inductively reduced Ac and Ox films. Two characteristic redox peaks are centered near 0.1 and 1.0 V_{RHE}, respectively. The first redox peak, which is attributed to the adsorption and stripping of surface hydrogen, is a hydrogen underpotential deposition (HUPD) peak and has a shoulder centered at 0.2 V_{RHE}. The presence of two HUPD peaks is

an indicator of two different Ir adsorption sites and therefore signifies two chemically distinctive species of an active center. Interestingly, the Ac films exhibit a more defined HUPD shoulder compared to the Ox films that form a rather broad redox peak. The hydrogen adsorption region is then followed by the formation of the oxide species $Ir(OH)_3$ which is hindered in acidic solution to a large extent[163], explaining the weakly defined respective redox peak at ca. 0.6 V_{RHE}. The next pair of anodic and cathodic peak is located near 0.9 V_{RHE} and is attributed to the Ir(III) to Ir(IV) oxide transition.[164, 165] Ac10 catalysts exhibit a more defined shape of the redox peak at ~ 0.95 V_{RHE} in both runs

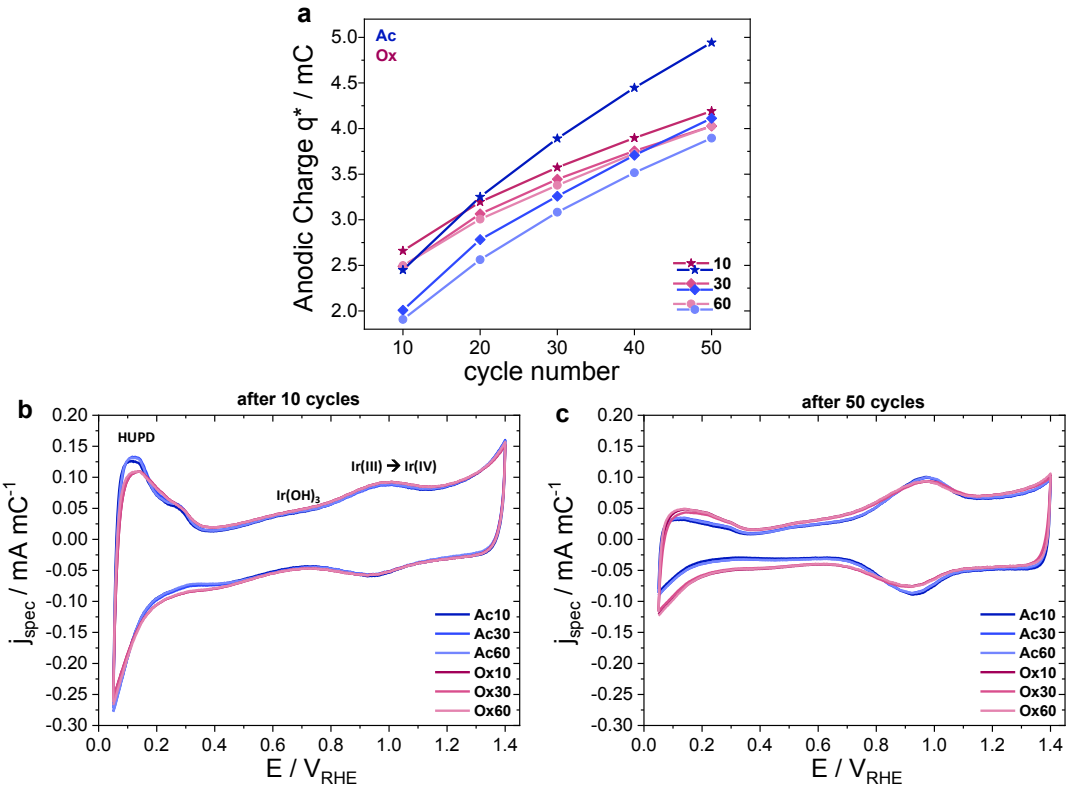

Figure 46| (a) Anodic charge q* obtained for _AP Ac (blue) and Ox (red) samples by integration of anodic currents measured by CV between the potential limits 0.4 and 1.4 V_{RHE} with 50 mV s^{-1}. (b) Cyclic voltammograms (50 mVs^{-1}) of the _AP Ac and Ox samples measured prior to OER after 10 and (c) after 50 cycles in the potential range of 0.05 and 1.4 V_{RHE} at a scan rate of 50 mV s^{-1}.

With increasing cycle number (from 10 to 50 cycles) the HUPD redox peak decreases drastically and is only slightly present after 50 cycles (compare Figure **46**b and c). The porous and hydrous nature of the electrochemically grown Ir oxide allows access of the electrolyte to the underlying surface Ir metal. Notice that the diminishing of the metallic character is more dominant on the Ir films on the Ac sample series, implying a faster completion of surface oxidation of the more open

structure of the Ac films due to evaporation of the acetate. The incorporation of oxygen into the metal structure might be facilitated by the morphology of the Ac films, whereas the structural composition of the Ir films of the Ox sample series seems to hamper the access to subsurface Ir sites and thereby their oxidation. As determined by the morphological analysis in Chapter 7.2.1, the defined and crystalline structure of the Ir films of the Ox sample series is more resistant to electrochemical oxidation to active Ir oxyhydroxide under anodic conditions. Prior to the second OER run the metallic feature remains absent for Ac10 in the 50th cycle, though slightly visible for Ox10.

7.2.3.2 OER Activity and Faraday Efficiency

The electrochemical activity curves of the stepped potential voltammetry are depicted in Figure 47a. Ac and Ox samples show different electrochemical behaviors. A longer heating period of the Ac samples is accompanied with a slight decrease in the electrocatalytic activity. The distinct activities of the directly reduced films are likely due to sintering or reorganization of the surface structure occurring during heating. The Ox-samples, however, do not show remarkable differences between different heating times, which agrees with a stable morphology of the films observed by SEM (see Figure 41 top row). That indicates the formation of a thermic stable structure, which is possibly benefited by the predefined structure of the former Ir oxide. A comparison between the current density and the charge normalized current density j_{spec} (Figure 47 b) does also support the prediction of a sintering process on the Ac films: while the curves of the Ac films approach each other, indicating a decrease of active surface area by sintering, the charge normalization barely changes the relative position of the Ox films' curves. Compared to polycrystalline bulk iridium (measured on a polished Ir cylinder) all films possess higher charge normalized current densities. The slightly non-linear/bend behavior of the Tafel plot (Figure 47c) and the loss of current density during each potential step of the SPV (see Figure A13 in the Appendix) is an interplay between the approach of the steady-state activity after a sudden potential step and the dissolution of the electrochemically obtained iridium oxides, as was evidenced by Mayrhofer *et al.*[166]

The determined Faraday efficiencies (FE) of the OER (_FE) in presence of chloride as a reactant of a competitive reaction (in 0.05 M H_2SO_4 with 0.01 M NaCl) are shown in Figure 47d. The films reduced from the oxide exhibit a higher FE towards

OER than the films reduced from the acetate. The latter also show larger differences in FE among each other. The Ox and the Ac films reveal a distinct trend in their FE with varying electrode potentials. With increasing potential, the FEs of the Ox films increase monotonically over the entire potential region. At higher potentials, oxygen evolution is more favored than chlorine evolution, as the kinetic hindrance of the OER process decreases at larger overpotentials. The Ac catalysts, however, initially show a slight overall decline before an increase in the FE can be observed. This effect points to complex reaction kinetics and will be further investigated in publications currently under preparation in our group. Nonetheless, a similar behavior of the Ox films at lower potentials cannot be excluded.

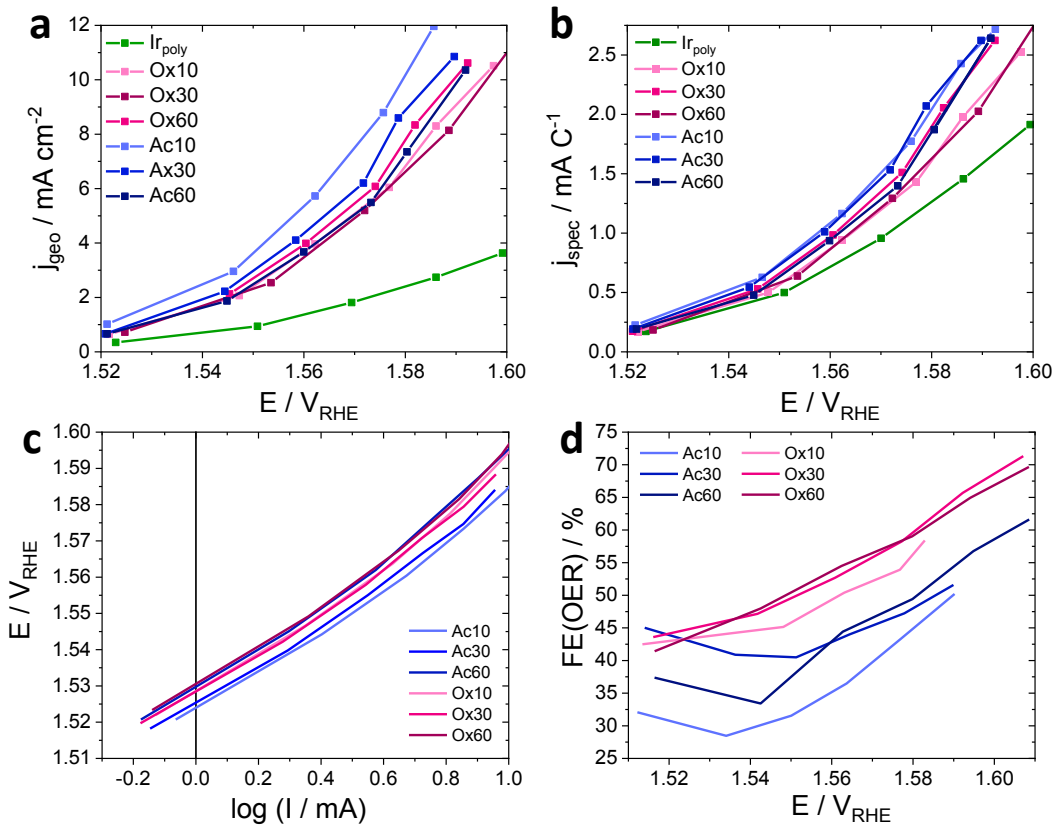

Figure 47| Electrochemical OER activity and FE curves of Ac and Ox films obtained by stepped potential voltammetry. (a) Geometrical current densities in 0.05 M H_2SO_4. The shorter heated Ac films exhibit a slightly higher activity compared to the Ox films and longer heated Ac films. (b) Specific current density in 0.05 M H_2SO_4. Due to charge normalization, the activities of the Ac films no longer differ significantly from each other. The relation of the Ox films' activities to each other is not affected. All reduced films show an enhanced OER performance than Ir_{poly}. (c) Tafel plot of the _OER films extrapolated from the SPV measurements (d) FE of OER in 0.05 M H_2SO_4/0.01 M NaCl. The Ox films show a considerable higher FE than the Ac films.

The stability performance was investigated by CA at ~ +1.734 V_{RHE} in 0.05 M H_2SO_4; the results are shown in Figure A14 in the Appendix. First, an abrupt drop of the current can be observed, assumed to be an approach to steady-state after quick potential change. The current then decreases slowly and almost linear, presumably associated with the dissolution of oxidic Ir. After about 3 h, the current becomes almost constant. There are two reasonable explanations for this behavior. Either an equilibrium of formation and dissolution of the active iridium oxide species (oxidation and dissolution rates are the same) is maintained or a more stable active species is present on the catalyst surface, as it was reported by Li *et al.*[22]

To examine the stability of the catalysts, EDX was measured on all samples, which have undergone electrochemical treatment including OER, stability testing and Faraday efficiency. Here, a loss of roughly 50 % Ir is observed, with an accuracy deviation of at most 10 %. This behavior agrees with the already mentioned lack of stability of electrochemically oxidized iridium.

7.2.3.3 Changes in the Surface Chemical State after OER Catalysis

The changes in the surface chemical state of Ir after activation and oxidation were traced with X-ray photoelectron spectroscopy (Figure 32). The Ir 4f XP spectra of the as-prepared Ac10 and Ox10 samples confirmed the presence of only metallic Ir in the XPS accessible area, indicating that the applied annealing step in H_2 is sufficient to reduce Ir on the surface to its metallic state. After the electrochemical treatments, the Ir 4f core-level spectra shifted to higher binding energy due to the formation of surface Ir oxide. The line shapes of the Ir 4f signals differ significantly depending on the potential range. Fits of the Ir 4f spectra revealed three different Ir species presented in these samples: metallic Ir^0, Ir^{IV} and Ir^Z species. The Ir species with a binding energy located at ~0.6 eV higher than that of the Ir^{IV} species was assigned as Ir^Z in this work, as the true origin of this component (Ir^{III} or Ir^V) is still a controversy.[31, 132]

After cycling in the potential range of 0.05-1.4 V_{RHE}, both Ac10 and Ox10 films were oxidized to a major extent; however, there is still discernible contribution of metallic Ir to the line shapes. On closer inspection, the Ir4f XP spectra of both films differ in the Ir^Z/Ir^{IV} species ratio, highlighting different oxidation behaviors. The Ac10_CV sample showed higher Ir^Z/Ir^{IV} ratio than the Ox10_CV sample, which might be the origin of its higher OER activity. In previous studies by Pfeifer *et al.*[29, 31] electronic defects in form of O 2p holes (O^{I-} species) were identified

in amorphous IrO_x. These highly electrophilic O^{I-} species are created by iridium vacancies in the IrO_x framework and possess a great activity in catalyzing the OER.[167] The formation of these species is in turn accompanied with the reduction of neighboring Ir^{IV} to Ir^{III} species, which appear at an Ir $4f_{7/2}$ binding energy of ~ 0.6 eV higher than the Ir^{IV} species according to their density functional theory calculations. Drawing upon these findings, the enhanced activity of the Ac10 catalyst may be deduced to coordination defects in the amorphous morphology facilitating the O-O formation in the OER.[29]

Upon exposing the catalysts to higher OER potentials (Ac10_OER and Ox10_OER) the metallic components diminished significantly to below 6 %. Two major oxidic components contribute to the Ir 4f spectrum. In the Ox catalyst (Ox10_OER) the Ir^Z/Ir^{IV} ratio is 0.7, showing that the dominant oxide species originates from Ir in the oxidation state IV. On the other hand, the Ir^Z/Ir^{IV} ratio in the Ac10_OER sample is 1.8, indicating the dominant species is the Ir^Z component. The higher specific OER activity based on charge normalization gives reason to believe that the O^{I-} species are present to a higher concentration on the Ac films. The difference in oxidation behavior of the Ac10 and Ox10 samples is plausibly explained by the difference in the morphology of the as-prepared metallic samples as discussed previously. The Ac10 film with highly cracked-, sponge-like morphology is prone to defect formation during electrochemical treatment, in contrast to the Ox10 film with smoother surface and more define structure as the starting point of the Ox film series is a rutile phase with Ir in the oxidation state +4.

The O 1s spectra of the Ac catalysts prior to and after OER testing revealed 3 different oxygen species which can be assigned to adsorbed water (~ 533.1 eV), lattice oxygen (~ 530.1 eV) and hydroxyl groups (~ 531.5 eV). All samples are distinguished by high surface hydroxyl group and very small lattice oxygen contents, typical for electrochemically grown iridium oxide.[168] The O1s XP spectra indicate that the oxide layers in the electrochemically treated samples are largely amorphous, which explains the absence of any crystalline IrO_x phase in the selected area electron diffraction (SAED) of these samples as discussed in section 7.2.2.2.

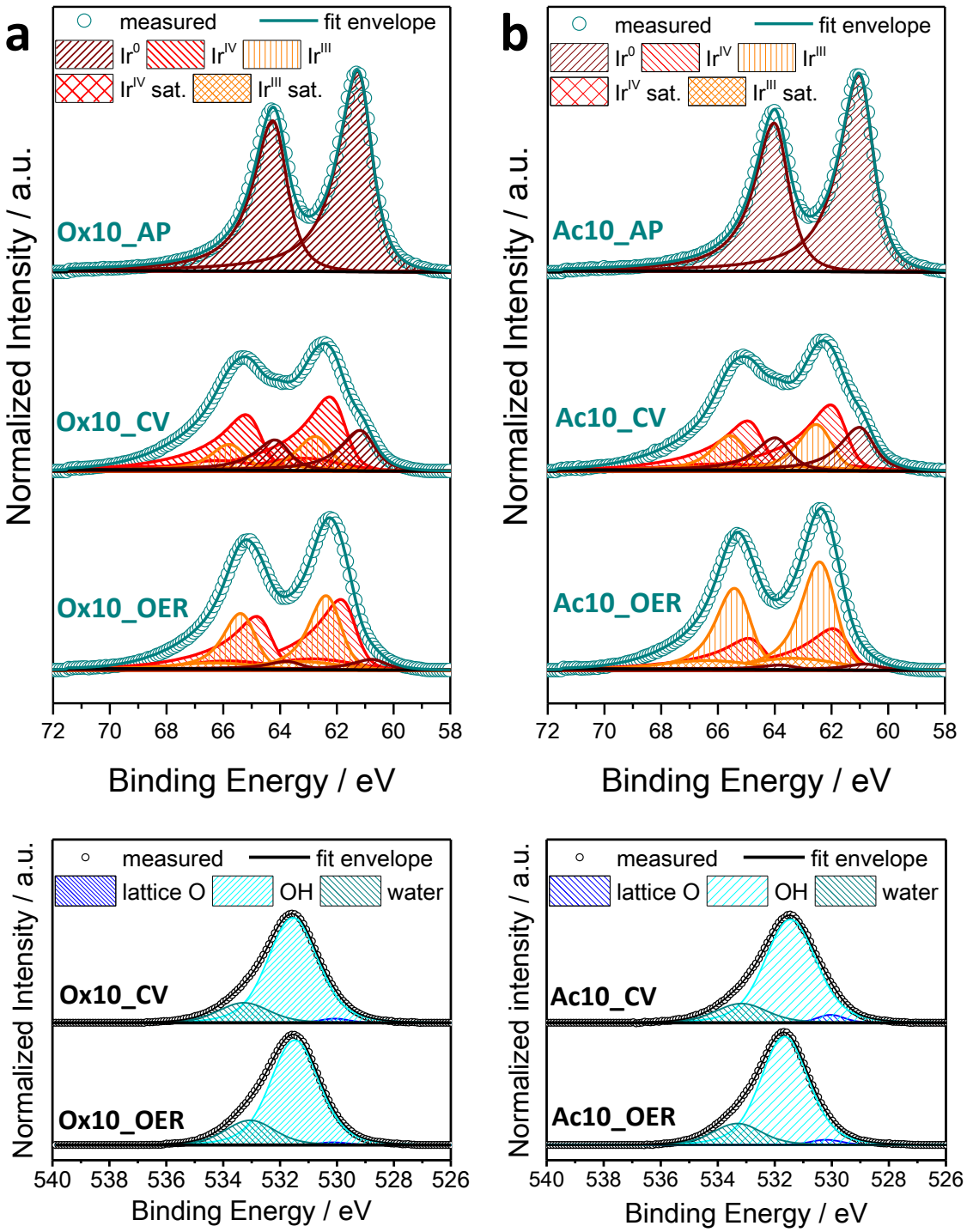

Figure 48| X-ray photoelectron spectroscopy of the Ox10 (a) and Ac10 (b) films at as-prepared states (_AP), after cyclic voltammetry between 0.05 – 1.4 V_{RHE} (_CV) and OER activity testing (_OER) with fitted components of Ir and O species. The as-prepared samples only show metallic Ir. Through potential cycling the major part of metallic Ir was oxidized to Ir^{III} and Ir^{IV}. After stepped potential voltammetry with potentials up to 1.60 V_{RHE} almost no Ir^0 is left and the ratio between Ir^{III} and Ir^{IV} is increased.

Chapter 8 Summary, Conclusions and Outlook

In this thesis, the successful design, assembly, verification and utilization of a novel, powerful coupled thermal-electrochemical electrode preparation-test chamber was presented that combines an inductive high-temperature annealing capability for single crystal and polycrystalline electrode preparations with versatile electrochemical modification and testing capabilities. During operation of the new cell, the crystal electrode surface is treated in a controllable atmospheric environment. The setup combines two integrated, yet distinct electrochemical cells which allow for a wide range of electrochemical procedures and measurements. One of the novelties is an electrode transfer mechanism into a portable transport chamber under inert gas. Thus, this newly introduced feature enables subsequent analytics without exposing the electrodes to the laboratory atmosphere. The rapid heating and temperature control up to 1900 °C in combination with a precise temperature protocol specification makes this cell unique among all previously reported electrochemical single crystal setups. The introduction of this setup makes the single crystals of Ir and Ru OER catalysts available for this kind of cell type for the first time. In addition, the cell is well suitable for performing deposition measurements in a spoon-like three-electrode setup with subsequent annealing for appropriate alteration of surface properties and reactivities.

The final cell design combines two separate electrochemical chambers in a closed setup. It not only allows for the application of a wider range of clean and enhanced single crystal research but also spreads the availability of studying larger single crystals to more laboratories. In this work, the concept was further enhanced by implementing a second electrochemical compartment, whereby both cabins can be independently filled with electrolyte from four separate purging electrolyte reservoirs. The considerably larger temperature range is strictly regulated by two sensitive IR sensors enabling a wide range of implementation strategies for electrochemical studies. The starting point of each electrochemical analysis with single crystal electrodes is clean and well-defined surfaces. In the presented setup, these surfaces are being produced by means of inductive heating in a controlled atmosphere. The adjusted gas flow prevents contamination of the electrochemical chamber with desorbed species and impurities from the surface. Ir single crystalline surfaces are finally prepared in a reductive atmosphere (H_2/Ar) to eliminate stronger and even chemically bond adsorbates.

The successful set up of the inductive electrochemical chamber and healing of single crystal surfaces was applied to the preparation of Ni-modified polycrystalline Ir electrodes including Ni/Ir overlayers and Nir/Ir near-surface electrodes. The rational design of electrocatalysts not only implies the controlled positioning of foreign atoms at the surface of the respective sample but can be further expanded to the sub-surface regions through thermal treatment in controlled atmosphere.

The analysis of the catalyst systems with respect to their electrocatalytic performance towards oxygen evolution revealed interesting insights. It is clearly evident that the Ni-modified polycrystalline Ir electrodes display distinct electrochemical properties. Incorporating Ni in form of an overlayer significantly reduces the overpotential to evolve oxygen in both acidic and alkaline solution. The promoting effect of Ni in IrNi bimetallic catalysts has been observed in various studies. In acidic milieu the higher activity might be deduced to the sacrificial leaching of Ni leading to a higher hydroxyl group (OH) fraction. The Ni-depleted active catalyst structure is expected to be composed of oxygen atoms being protonated from the electrolyte to form surface hydroxyl groups which presumably act as crucial intermediates in the OER mechanism. The beneficial effect of Ni addition to the OER activity, however, is no longer given to the same extent if Ni is present in the subsurface layer of the electrode. Thus, we can conclude that Ni in the NSA configuration is not able to perform as a sacrificial catalyst component as effectively as Ni in the OL configuration. Further, the electronic effect of Ni on Ir might exercise a negative effect on the binding energy of Ir towards reaction intermediates in the OER. However, it cannot be neglected that the reductive treatment which formed the NSA led to partial healing of the Ir surface with a smaller density of defect and step sites. As the environment of Ir was significantly altered, so was its activity. In alkaline media the highly hydrophilic Ni adatoms are sufficient to achieve the desired effect of increasing the OER performance of the catalyst material. Interestingly, the performance of the OL system increases in KOH after it was pretreated in acid electrolyte beforehand. This observation confirms the hypothesis of Ni dissolution in acid. It appears as if the preceding OER treatment in 0.05 M H_2SO_4 has an advantageous impact on the electrocatalytic properties in KOH and can be deduced to the aforementioned leaching of Ni in acidic raising the concentration of surface OH atoms. The performance in the OER of the catalysts including the CO oxidation performance is not only a function of the pure composition of the material but does strongly depend on the relative position of the

metals to each other. However, it must be kept in mind that the interpretation of the peaks with regard to the CO stripping measurements, especially of the shoulders is quite complex due to the presence of surface defects. In Chapter 6, electrochemical methods including cyclic voltammetry and controlled-potential coulometry are the first way of providing important insights into the mechanistic details of the electrochemical oxygen evolution in acidic and alkaline solution. From CO oxidation and DFT-based H-Ir bond energies certain suggestions could be drawn on the relative position of Ni in both modified catalyst systems. But electrochemical techniques alone cannot reveal the distribution of defects and adsorbates on surfaces of solids with a desired atomic resolution. The aim for future work would therefore be to scope surface properties and structures with scanning tunneling microscopies (STMs) which are outstanding instruments that measure with remarkable resolution and accuracy.

In the study of the morphology, structure and catalytic activity of supported metallic Ir films, the successful synthesis of metallic Ir thin-films on Ti substrate using two different synthesis approaches was presented. It was found that the catalyst structure was significantly influenced by the choice of the synthesis routes. Regardless of the heating time, the Ox route consistently resulted in the identical structure creating a system insensitive against fluctuations in synthesis parameters. The Ox route might therefore be conducted in a common tube furnace also, with a less sharp heating window (heating-up and cool down). In contrast, SEM and TEM revealed that the morphology of the Ir films synthesized over the Ac route exhibited a significant sensitivity towards the heating treatment. The application of sharp inductive heating accompanied by a defined heating time thus enables to control the progress of morphological restructuring like sintering processes. These distinctive morphological properties were found to have a strong effect on the catalytic properties. A slight decrease of OER activity with increasing heating period was observed; however, an opposite behavior was discovered for OER FE in chlorine containing electrolyte. The difference between the catalytic properties of both catalyst types is reduced, as the Ac films approach the Ox samples with longer heating time. Although this effect is not observable in the given scale of the morphology analysis, it cannot be excluded that structural similarities occur on a smaller scale. As expected, a complete oxidation of surface near Ir occurs during OER, while the majority of the film stays in its metallic state. In the search for cost-effective materials catalyzing the OER, the Ox route is a promising approach

to investigate further modifications with metallic additives as its final surface structure is quickly formed and tolerant towards different heating periods.

The results of this work show that the activities and performances of are highly sensitive to the materials composition and pretreatment. Established and effective synthesis routes have to be implemented to result in the desired material composition and optimization for increasing the rates in the electrocatalytic reaction. By integrating and combining density functional theory (DFT) methods with experimental results and advanced analytical techniques, the conclusions can be translated into optimal synthesis routes for functional catalytic nanoparticles. It must be kept in mind that further improvements of the energy conversion process in terms of efficiency, reversibility and cost-effectiveness must be pursued and continuously reviewed.

In the future, the new combined crystal electrode annealing and electrochemical test set up will be utilized for the investigation and characterization of the presence and nature of electronic catalyst-support interactions between IrOx phases and well-defined oxide layers or high surface area oxide powder supports.

1 Appendix

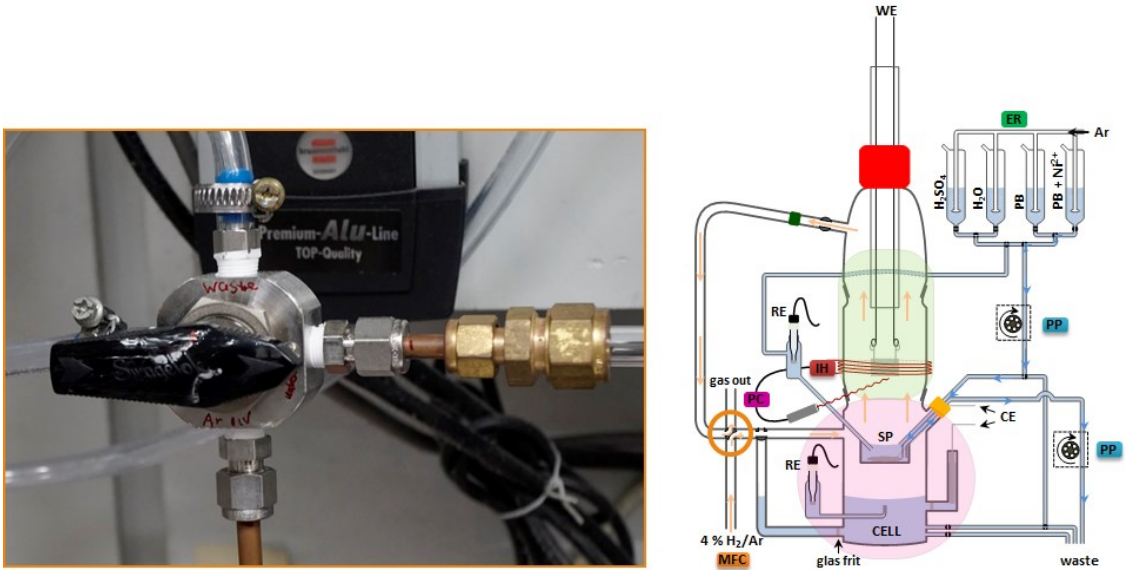

Figure A1| Installment of a 4-way valve allowing for a gas flow change in the chamber. During annealing the valve is adjusted in a way that the single crystal electrode is flushed from below.

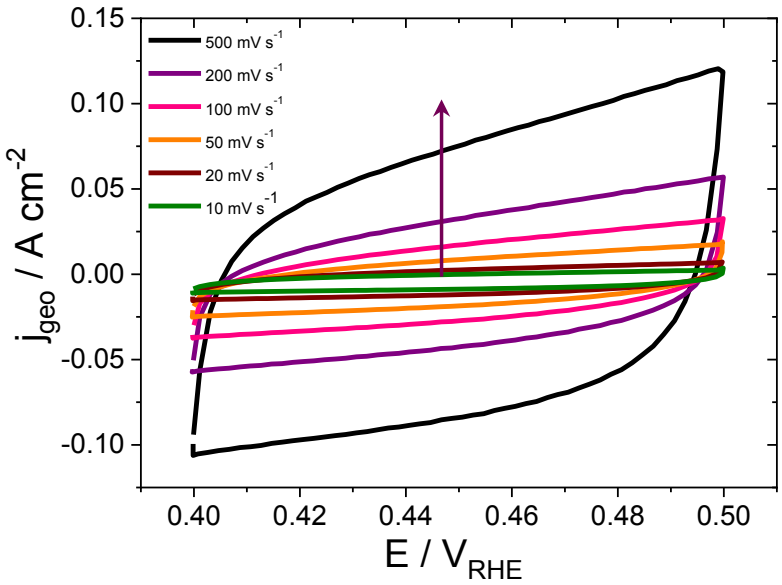

Figure A2| Double-layer capacitance measurements displaying cyclic voltammograms of Ir_{poly} measured in a potential window in which no faradic currents occur. Following scan rates were adjusted: 500 mV s^{-1}, 200 mV s^{-1}, 100 mV s^{-1}, 50 mV s^{-1}, 20 mV s^{-1} and 10mV s^{-1}.

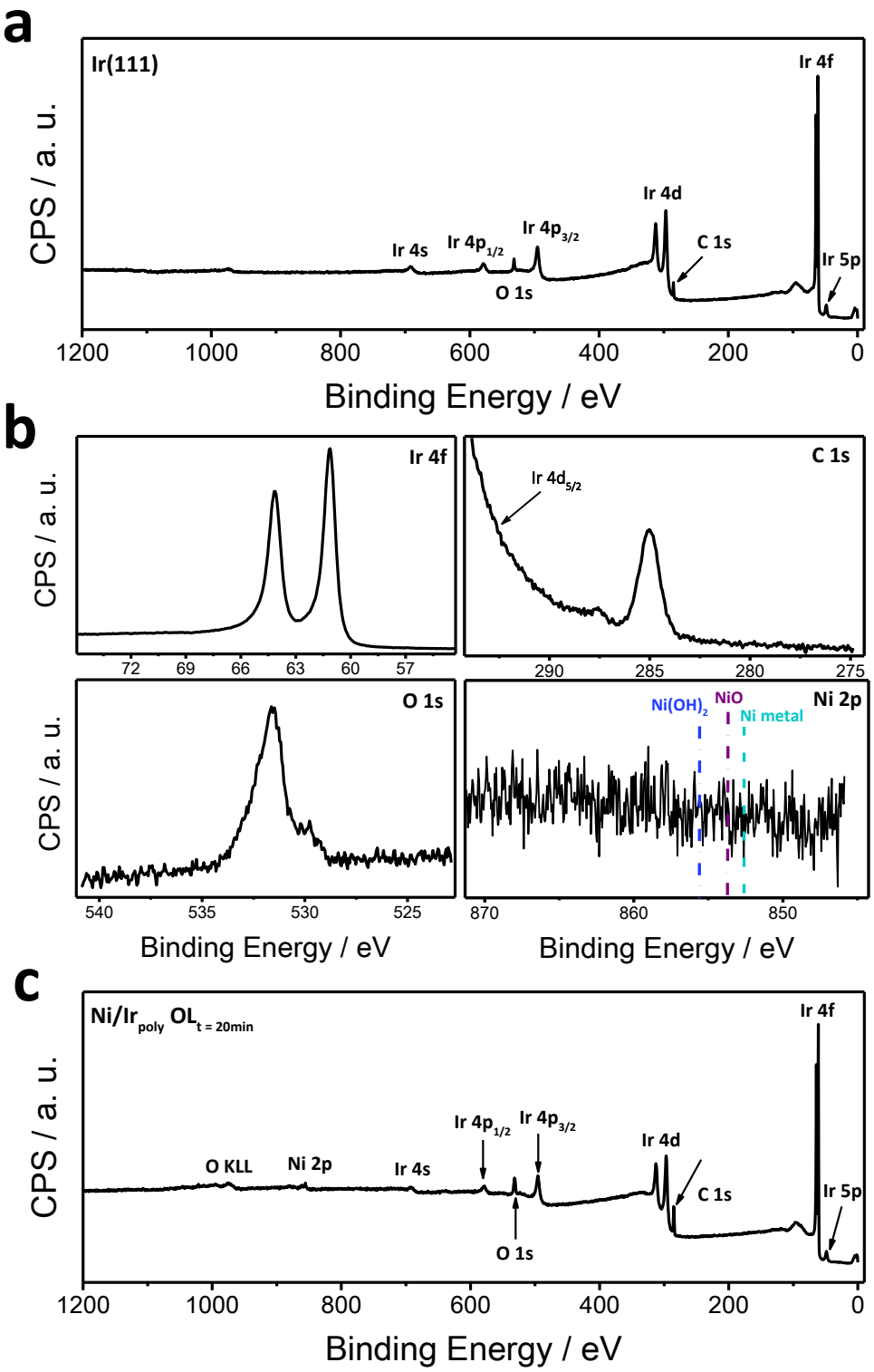

Figure A3| X-ray photoelectron spectroscopy measurements of (a) Ir(111) over the entire energy range. (b) High-resolution spectra of Ir(111) displaying the Ir 4f, C 1s, O 1s and Ni 2p spectra. (c) XP spectra of Ni/Ir_{poly} $OL_{t=20\ min}$ over the entire energy range.

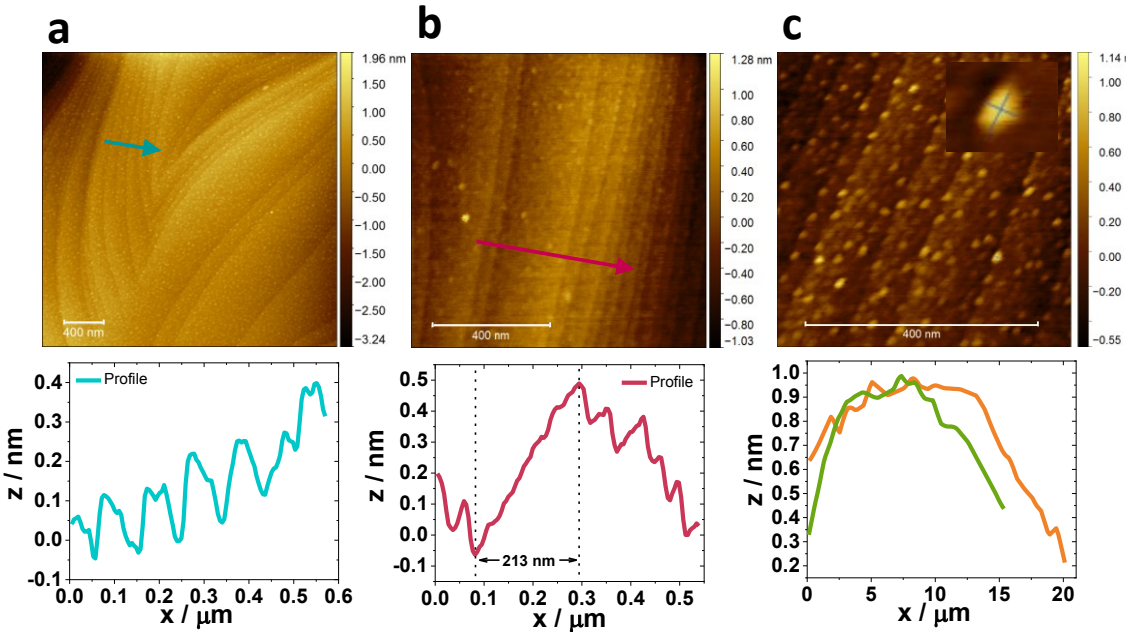

Figure A4| (a) Atomic force microscopy (AFM) images of Ni/Ir(111) OL with respective height profiles. (b) Magnification of a terrace assembly of (a) and (c) higher magnification. Scale bar is 400 nm. Arrows give the direction of the calculated height profile.

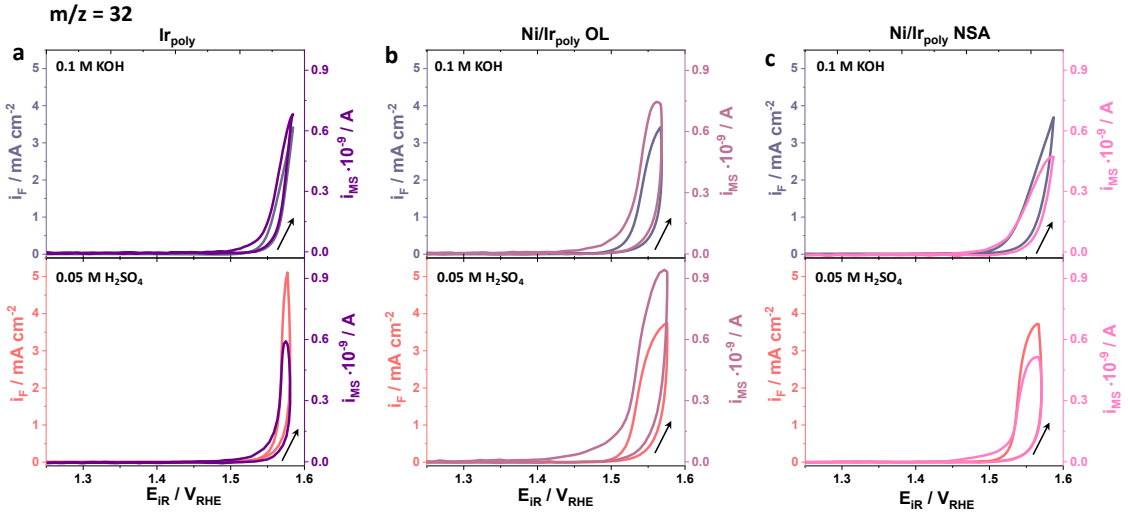

Figure A5| Differential electrochemical mass spectrometry (DEMS) measured in 0.1 M KOH followed by measurements in 0.05 M H_2SO_4 using a dual thin-layer flow-cell. Cyclic voltammograms were recorded at 50 mV s^{-1} between 1.0 and 1.6 V_{RHE}. (a) Ir_{poly}, (b) Ni/Ir_{poly} OL and (c) Ni/Ir_{poly} NSA. Geometric current densities measured with the potentiostat are in blue for 0.1 M KOH and in red for 0.05 M H_2SO_4 (left axis). The mass spectrometric faradaic ion currents of O_2 (m/z=32) are shown in the respective color code of the catalysts (right axis). Arrows indicate the scan direction.

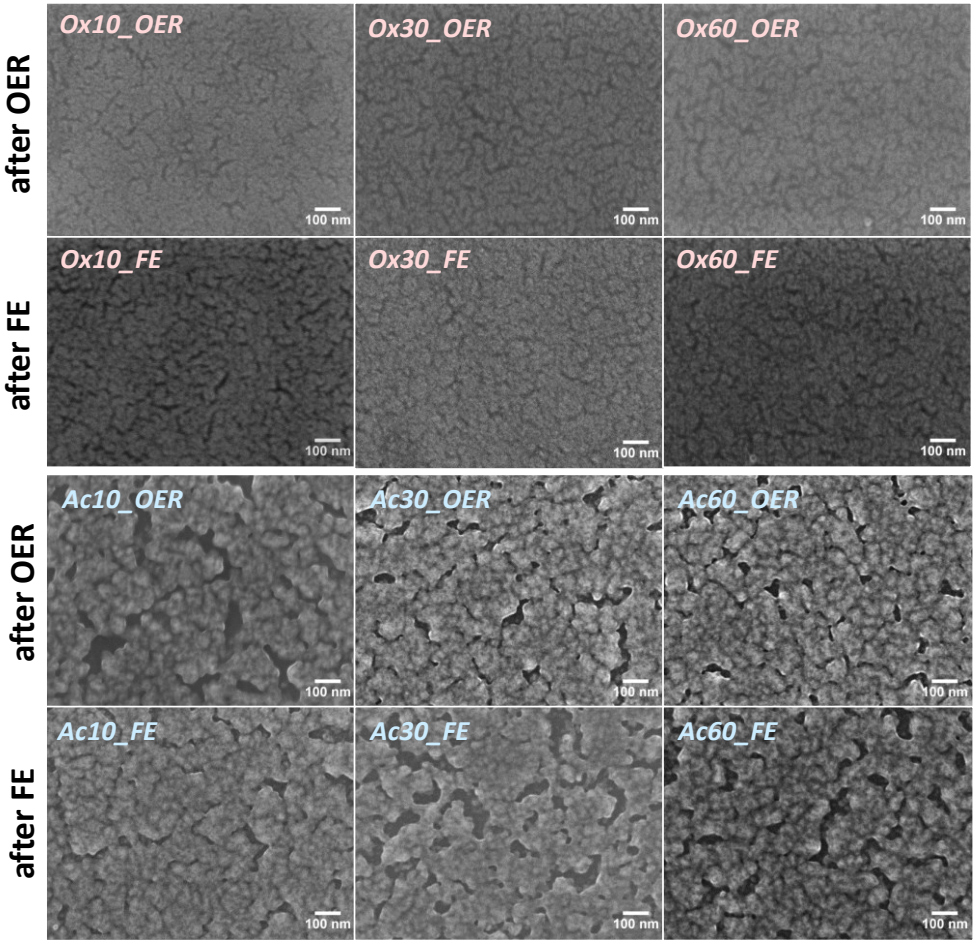

Figure A6| SEM images of Ox (top) and Ac (bottom) film series after OER (_OER, 1st and 3rd row) and after Faraday efficiency measurements (_FE, 2nd and 4th row).

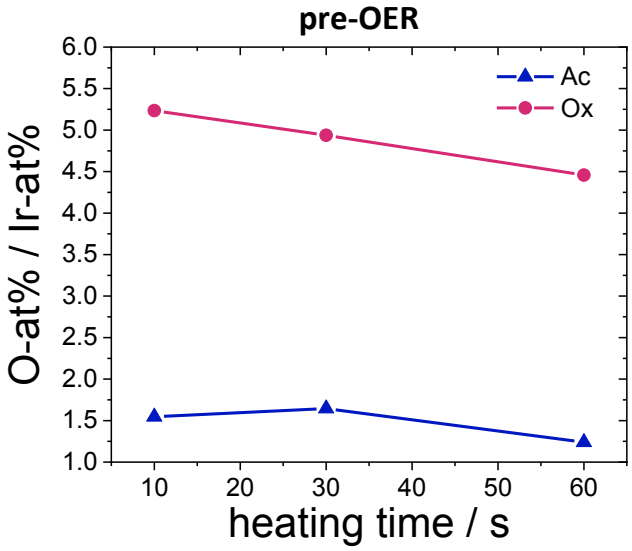

Figure A7| EDX results of _AP Ox and Ac films showing the atomic percentage (at%) ratio of O to Ir measured with 6 keV. Independent of heating time, the Ox films exhibit a significant higher oxygen amount than the Ac films.

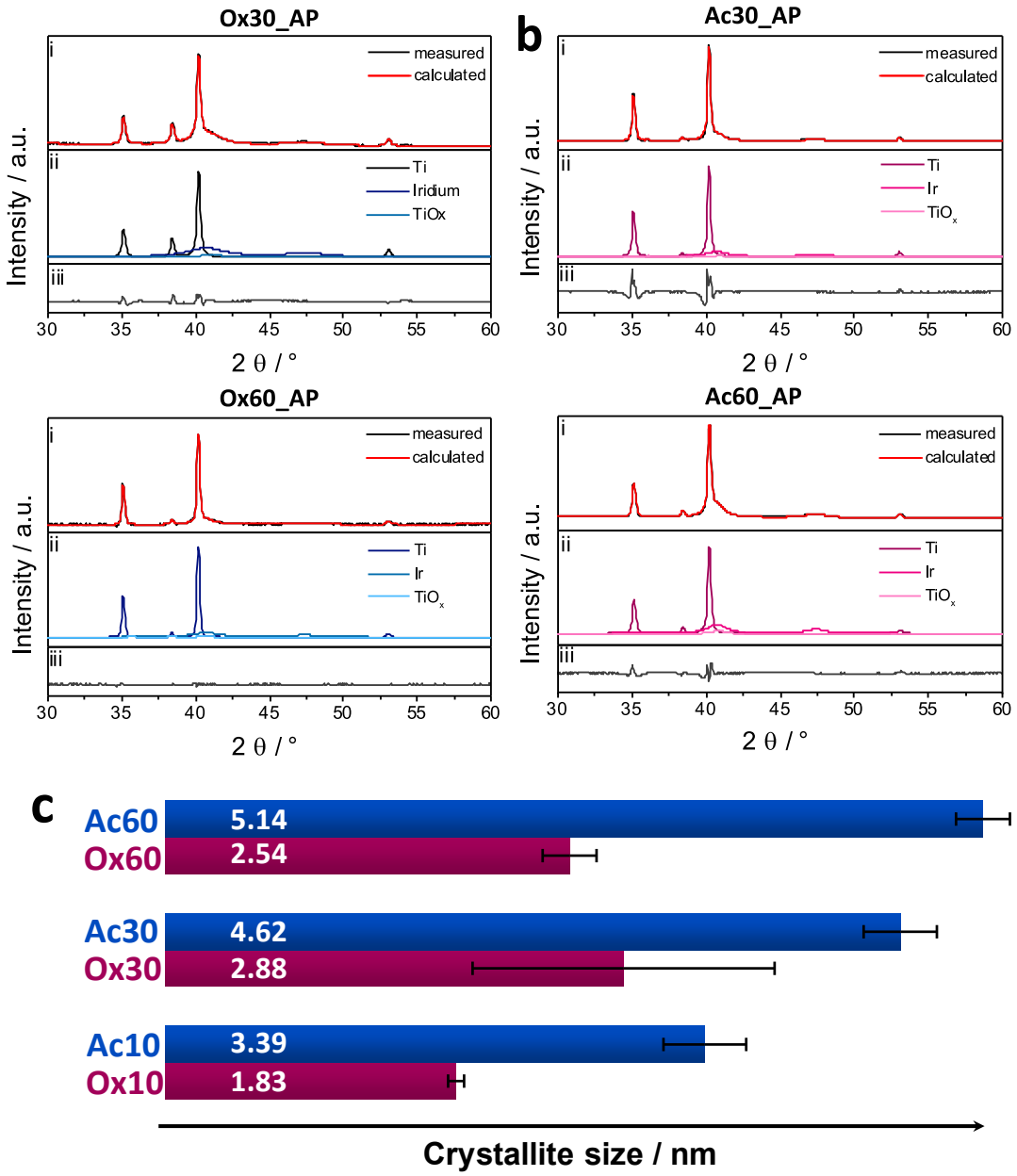

Figure A8| Grazing incidence X-ray diffraction measurement of _AP (a) Ox and (b) Ac samples on Ti substrate with (i) measured and calculated diffraction pattern from Rietveld refinement results. (ii) The Ti, Ir and TiO_x phases, which were used within the refinement. (iii) The difference between measured and calculated diffraction pattern. (c) Crystallite sizes of _AP samples obtained by quantitative Rietveld analysis are given in white in the respective bar.

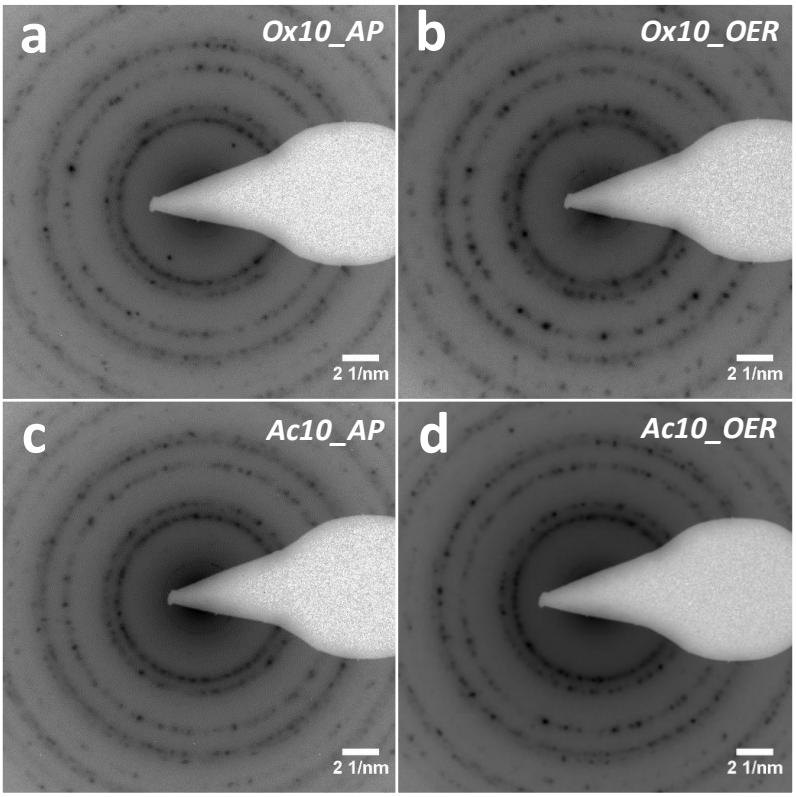

Figure A9| Selected area diffraction (SAED) images of the scraped (a, c) _AP and (b, d) _OER films.

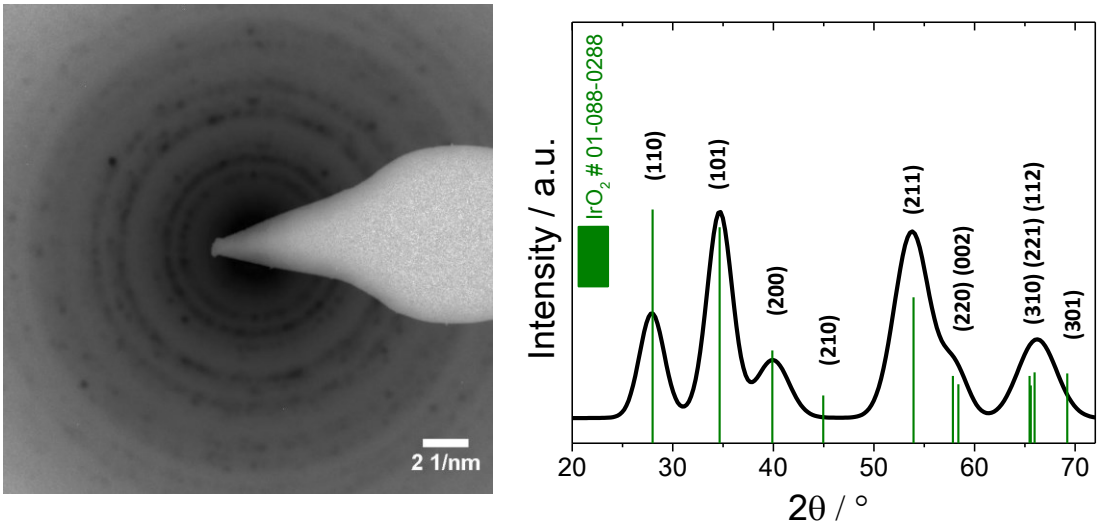

Figure A10| SAED and evaluated diffraction pattern of an IrOx film reveals a rutile-type phase.

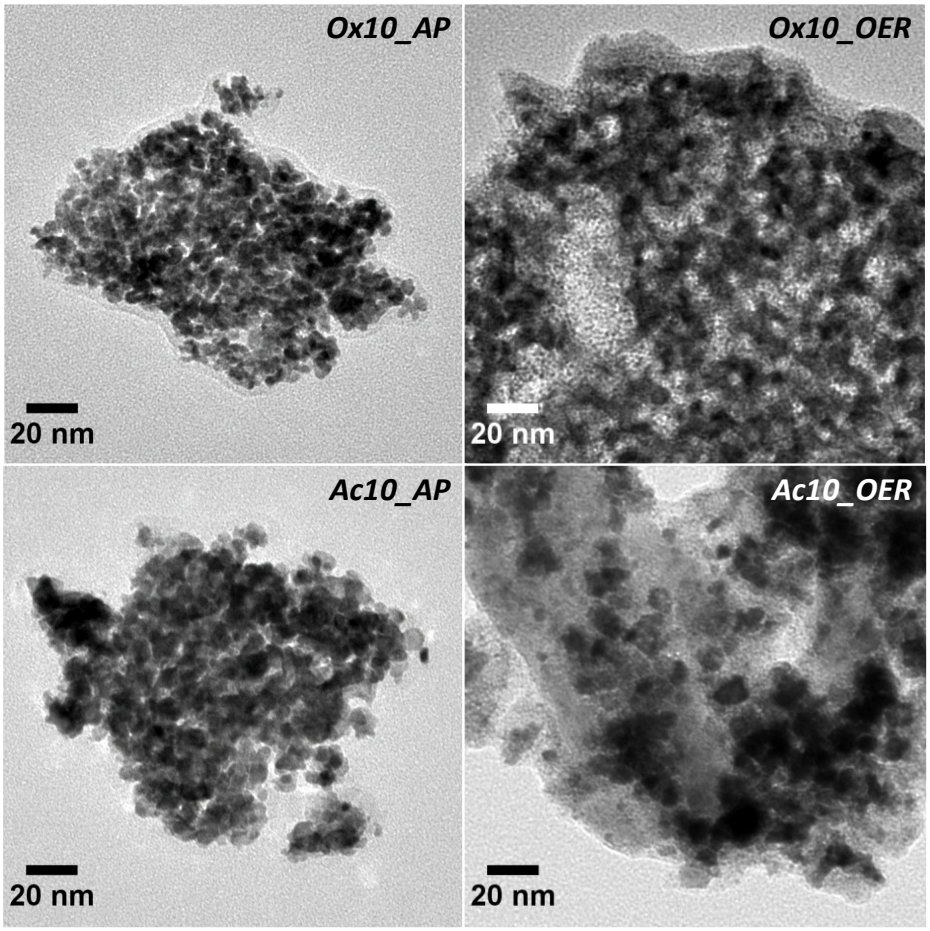

Figure A11| TEM images of the scraped _AP and _OER films displaying crystalline Ir particles.

pre-OER

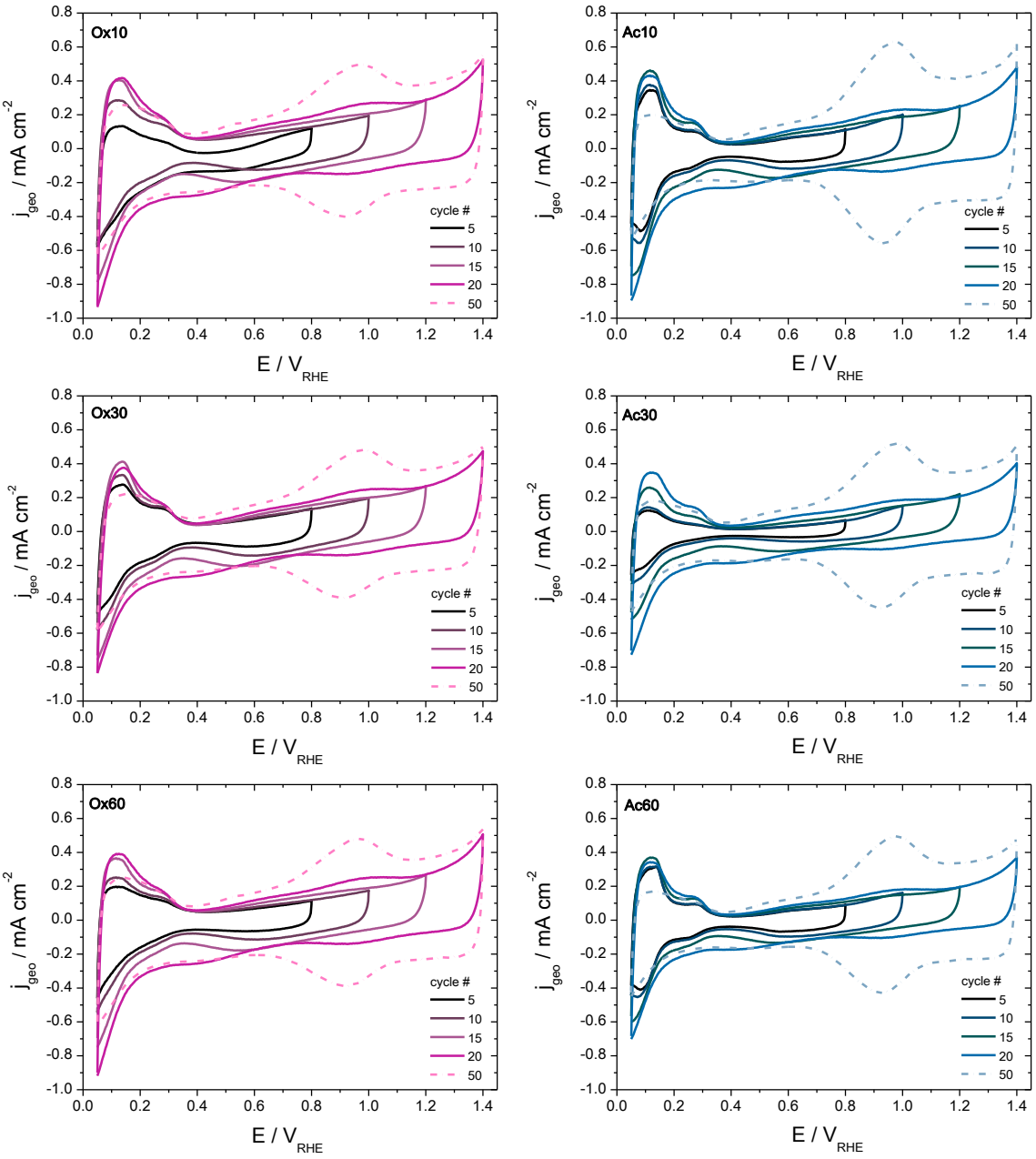
Ox10
Ac10
Ox30
Ac30
Ox60
Ac60
j_geo / mA cm^-2
E / V_RHE
cycle #
5
10
15
20
50

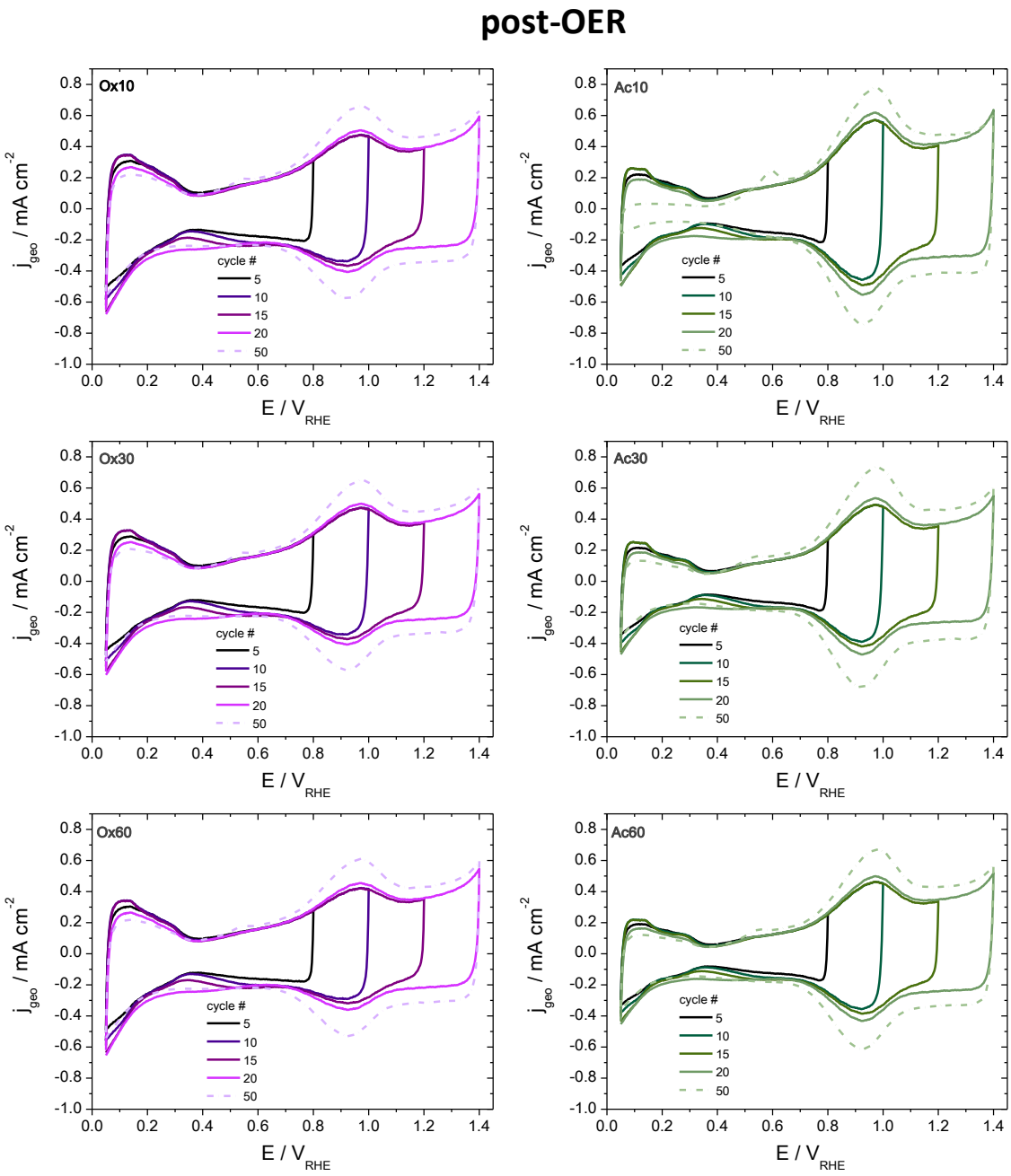

Figure A12| Voltammetric curves of Ac and Ox films before (pre-OER) and after (post-OER) oxygen evolution reaction (OER) in 0.05 M H_2SO_4 solution at a sweep rate of 50 mV s^{-1}. The potential range is between 0.05 and 1.4 V_{RHE}. The upper potential limit is progressively opened by 200 mV steps from 0.8 V_{RHE}. For every potential step, the 5th cycle is presented.

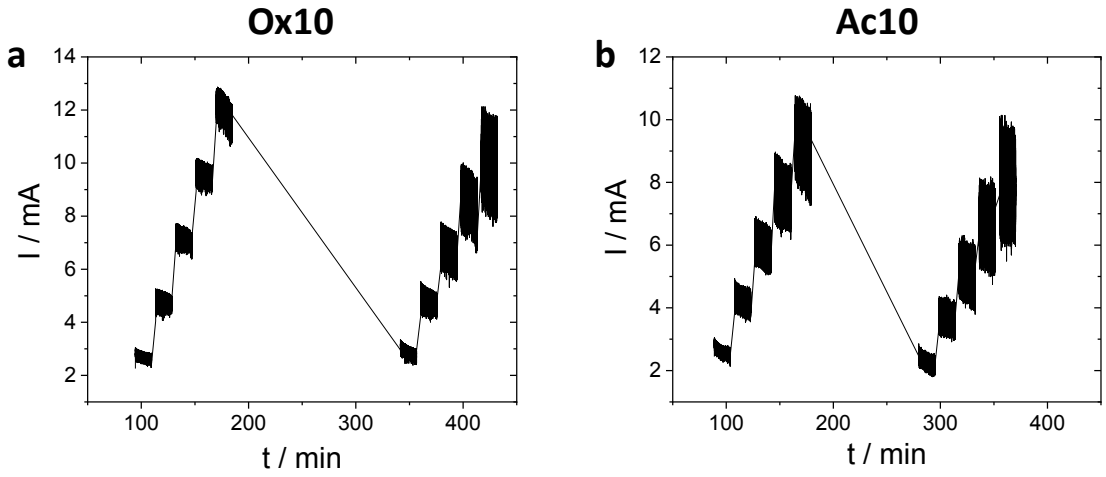

Figure A13| Stepped potential voltammetries (SPVs) exemplarily shown for Ox10 and Ac10. The non-stationary behavior of the potential steps may be caused by instabilities of the catalyst.

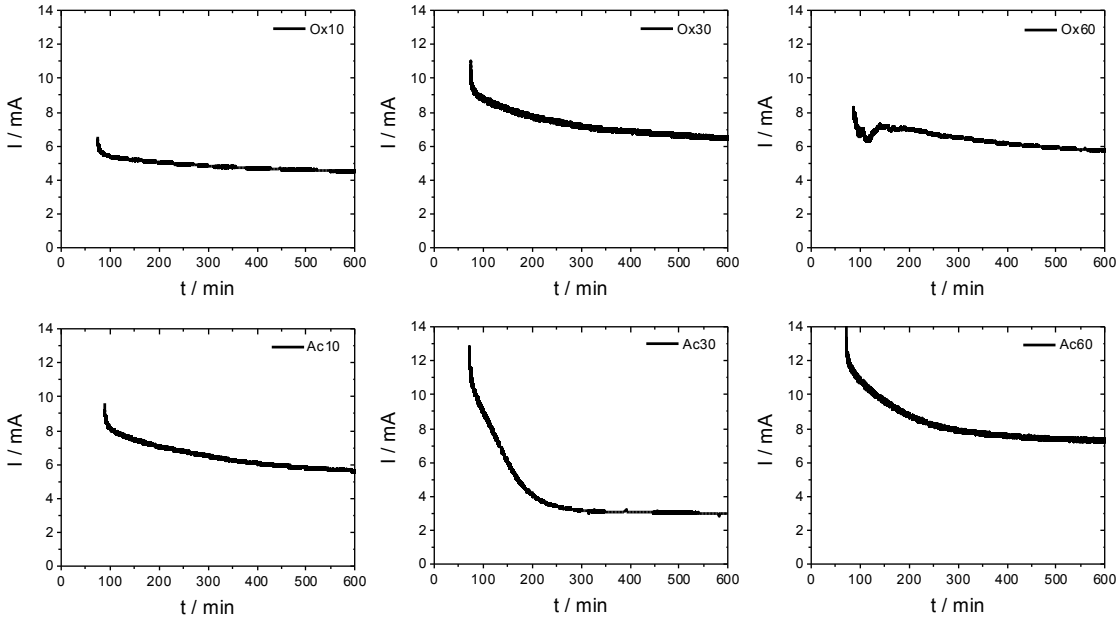

Figure A14| Stability measurements of Ox and Ac films in 0.05 M H_2SO_4 at 1.734 V_{RHE} (not IR corrected). The catalysts show a major loss of current in the beginning before running in to an almost stationary plateau, an approach to steady-state after quick potential change.

2 References

[1] D.Q. T. F. Stocker, G.-K. Plattner, L. V. Alexander, S. K. Allen, N. L. Bindoff, F.- M. Bréon, J. A. Church, U. Cubasch, S. Emori, P. Forster, P. Friedlingstein, N. Gillett, J. M. Gregory, D. L. Hartmann, E. Jansen, B. Kirtman, R. Knutti, K. K. Kumar, P. Lemke, J. Marotzke, V. Masson-Delmotte, G. A. Meehl, I. I. Mokhov, S. Piao, V. Ramaswamy, D. Randall, M. Rhein, M. Rojas, C. Sabine, D. Shindell, L. D. Talley, D. G. Vaughan, S.-P. Xie, *IPCC, 2013: Climate Change 2013: The Physical Science Basis. Contribution of Working Group I to the Fifth Assessment Report of the Intergovernmental Panel on Climate Change*, Cambridge, United Kingdom and New York, NY, USA, **2013**, pp 1535.

[2] ***BP** Statistical Review of World Energy 67th edition*, London, UK, **June 2018**, pp 53.

[3] https://www.energy-charts.de/energy_pie_de.htm?year=2017, **Fraunhofer ISE**, access date: 08.08.2018

[4] *Electrical Energy Storage*, International Electrotechnical Commission, IEC, Geneva, Switzerland, **2011**, pp 78.

[5] M.G. T. Smolinka, J. Garche, *NOW-Studie: Stand und Entwicklungspotenzial der Wasserelektrolyse zur Herstellung von Wasserstoff aus regenerativen Energien*, Fraunhofer ISE, FCBAT, **2011**, pp 1.

[6] A. Ursua, L.M. Gandia, P. Sanchis, *Proceedings of the IEEE 100*, **2012**, 410.

[7] F. Barbir, *Solar Energy 78*, **2005**, 661.

[8] M. Carmo, D.L. Fritz, J. Mergel, D. Stolten, *International Journal of Hydrogen Energy 38*, **2013**, 4901.

[9] S. Siracusano, V. Baglio, N. Van Dijk, L. Merlo, A.S. Aricò, *Applied Energy 192*, **2017**, 477.

[10] J.H. Russell, L.J. Nuttall, A.P. Fickett, *Am. Chem. Soc., Div. Fuel Chem., Prepr. 18*, **1973**, 24.

[11] A. Damjanovic, A. Dey, J.O.M. Bockris, *Journal of The Electrochemical Society 113*, **1966**, 739.

[12] J.O.M. Bockris, *The Journal of Chemical Physics 24*, **1956**, 817.

[13] J.O.M. Bockris, A.K.M. Shamshul Huq, *Proceedings of the Royal Society of London. Series A. Mathematical and Physical Sciences 237*, **1956**, 277.

[14] D.N. Buckley, L.D. Burke, *Journal of the Chemical Society, Faraday Transactions 1: Physical Chemistry in Condensed Phases 72*, **1976**, 2431.

[15] L.D. Burke, O.J. Murphy, J.F. O'Neill, S. Venkatesan, *Journal of the Chemical Society, Faraday Transactions 1: Physical Chemistry in Condensed Phases 73*, **1977**, 1659.

[16] N. Danilovic, R. Subbaraman, K.-C. Chang, S.H. Chang, Y.J. Kang, J. Snyder, A.P. Paulikas, D. Strmcnik, Y.-T. Kim, D. Myers, V.R. Stamenkovic, N.M. Markovic, *The Journal of Physical Chemistry Letters 5*, **2014**, 2474.

[17] Y. Matsumoto, E. Sato, *Materials Chemistry and Physics 14*, **1986**, 397.

[18] R. Kötz, H.J. Lewerenz, P. Brüesch, S. Stucki, *Journal of Electroanalytical Chemistry and Interfacial Electrochemistry 150*, **1983**, 209.

[19] R. Kötz, S. Stucki, D. Scherson, D.M. Kolb, *Journal of Electroanalytical Chemistry and Interfacial Electrochemistry 172*, **1984**, 211.

[20] H.J. Lewerenz, S. Stucki, R. Kötz, *Surface Science 126*, **1983**, 463.

[21] S. Cherevko, A.R. Zeradjanin, A.A. Topalov, N. Kulyk, I. Katsounaros, K.J.J. Mayrhofer, *ChemCatChem 6*, **2014**, 2219.

[22] T. Li, O. Kasian, S. Cherevko, S. Zhang, S. Geiger, C. Scheu, P. Felfer, D. Raabe, B. Gault, K.J.J. Mayrhofer, *Nature Catalysis 1*, **2018**, 300.

[23] M. Bernicke, E. Ortel, T. Reier, A. Bergmann, J. Ferreira de Araujo, P. Strasser, R. Kraehnert, *ChemSusChem 8*, **2015**, 1908.

[24] H.N. Nong, H.-S. Oh, T. Reier, E. Willinger, M.-G. Willinger, V. Petkov, D. Teschner, P. Strasser, *Angewandte Chemie International Edition 54*, **2015**, 2975.

[25] T. Reier, Z. Pawolek, S. Cherevko, M. Bruns, T. Jones, D. Teschner, S. Selve, A. Bergmann, H.N. Nong, R. Schlögl, K.J.J. Mayrhofer, P. Strasser, *Journal of the American Chemical Society 137*, **2015**, 13031.

[26] C.C.L. McCrory, S. Jung, J.C. Peters, T.F. Jaramillo, *Journal of the American Chemical Society 135*, **2013**, 16977.

[27] E. Antolini, E.R. Gonzalez, *Solid State Ionics 180*, **2009**, 746.

[28] R. Kötz, S. Stucki, *Electrochimica Acta 31*, **1986**, 1311.

[29] V. Pfeifer, T.E. Jones, J.J. Velasco Velez, R. Arrigo, S. Piccinin, M. Havecker, A. Knop-Gericke, R. Schlogl, *Chemical Science 8*, **2017**, 2143.

[30] V. Pfeifer, T.E. Jones, J.J. Velasco Vélez, C. Massué, R. Arrigo, D. Teschner, F. Girgsdies, M. Scherzer, M.T. Greiner, J. Allan, M. Hashagen, G. Weinberg, S. Piccinin, M. Hävecker, A. Knop-Gericke, R. Schlögl, *Surface and Interface Analysis 48*, **2015**, 261.

[31] V. Pfeifer, T.E. Jones, J.J. Velasco Velez, C. Massue, M.T. Greiner, R. Arrigo, D. Teschner, F. Girgsdies, M. Scherzer, J. Allan, M. Hashagen, G. Weinberg, S. Piccinin, M. Havecker, A. Knop-Gericke, R. Schlogl, *Physical Chemistry Chemical Physics 18*, **2016**, 2292.

[32] T. Reier, I. Weidinger, P. Hildebrandt, R. Kraehnert, P. Strasser, *ECS Transactions 58*, **2013**, 39

[33] T. Reier, D. Teschner, T. Lunkenbein, A. Bergmann, S. Selve, R. Kraehnert, R. Schlögl, P. Strasser, *Journal of The Electrochemical Society 161*, **2014**, F876.

[34] E. Ortel, T. Reier, P. Strasser, R. Kraehnert, *Chemistry of Materials 23*, **2011**, 3201.

[35] A. de Oliveira-Sousa, M.A.S. da Silva, S.A.S. Machado, L.A. Avaca, P. de Lima-Neto, *Electrochimica Acta 45*, **2000**, 4467.

[36] E. Herrero, L.J. Buller, H.D. Abruña, *Chemical Reviews 101*, **2001**, 1897.

[37] R.B. Grant, R.M. Lambert, *Journal of Catalysis 92*, **1985**, 364.

[38] C. Lamy, J.M. Leger, J. Clavilier, R. Parsons, *Journal of Electroanalytical Chemistry and Interfacial Electrochemistry 150*, **1983**, 71.

[39] N.M. Markovic, H.A. Gasteiger, P.N. Ross, *The Journal of Physical Chemistry 99*, **1995**, 3411.

[40] I.H. Omar, H.J. Pauling, K. Jüttner, *Journal of The Electrochemical Society 140*, **1993**, 2187.

[41] H.-S. Oh, H.N. Nong, P. Strasser, *Advanced Functional Materials 25*, **2015**, 1074.

[42] T. Ohta, Energy Carriers And Conversion Systems With Emphasis On Hydrogen - Volume I, *Encyclopedia of life support systems. Energy sciences, engineering, and technology resources*, Eolss Publishers, **2009**, pp. 136.

[43] A. Tremel, Electricity-based Fuels, *SpringerBriefs in Applied Sciences and Technology*, Springer International Publishing, **2017**.

[44] S. Trasatti, *Journal of Electroanalytical Chemistry 476*, **1999**, 90.

[45] R. de Levie, *Journal of Electroanalytical Chemistry 476*, **1999**, 92.

[46] R.W. Ramette, *Journal of Chemical Education 64*, **1987**, 885.

[47] H. Eyring, *Chemical Reviews 17*, **1935**, 65.

[48] J.N. Coupland, An Introduction to the Physical Chemistry of Food, *Food Science Text Series*, Springer New York, **2014**, pp. 45.

[49] J.O.M. Bockris, Z. Nagy, *Journal of Chemical Education 50*, **1973**, 839.

[50] I.C. Man, H.-Y. Su, F. Calle-Vallejo, H.A. Hansen, J.I. Martínez, N.G. Inoglu, J. Kitchin, T.F. Jaramillo, J.K. Nørskov, J. Rossmeisl, *ChemCatChem 3*, **2011**, 1159.

[51] J. Rossmeisl, A. Logadottir, J.K. Nørskov, *Chemical Physics 319*, **2005**, 178.

[52] J. Rossmeisl, Z.W. Qu, H. Zhu, G.J. Kroes, J.K. Nørskov, *Journal of Electroanalytical Chemistry 607*, **2007**, 83.

[53] I. Chorkendorff, J.W. Niemantsverdriet, Introduction to Catalysis, *Concepts of Modern Catalysis and Kinetics*, Wiley-VCH Verlag GmbH & Co. KGaA, **2005**, pp. 1.

[54] R.I. Masel, *Principles of Adsorption and Reaction on Solid Surfaces*, A Wiley-Interscience publication, Wiley, NY **1996**.

[55] T. Bligaard, J.K. Nørskov, S. Dahl, J. Matthiesen, C.H. Christensen, J. Sehested, *Journal of Catalysis 224*, **2004**, 206.

[56] A.S. Bandarenka, M.T.M. Koper, *Journal of Catalysis 308*, **2013**, 11.

[57] M.T.M. Koper, *Nanoscale 3*, **2011**, 2054.

[58] K.A. Stoerzinger, L. Qiao, M.D. Biegalski, Y. Shao-Horn, *The Journal of Physical Chemistry Letters 5*, **2014**, 1636.

[59] A. Bergmann, E. Martinez-Moreno, D. Teschner, P. Chernev, M. Gliech, J.F. de Araújo, T. Reier, H. Dau, P. Strasser, *Nature Communications 6*, **2015**, 8625.

[60] A.B. Laursen, A.S. Varela, F. Dionigi, H. Fanchiu, C. Miller, O.L. Trinhammer, J. Rossmeisl, S. Dahl, *Journal of Chemical Education 89*, **2012**, 1595.

[61] Y.-H. Fang, Z.-P. Liu, *Journal of the American Chemical Society 132*, **2010**, 18214.

[62] P. Castelli, S. Trasatti, F.H. Pollak, W.E. O'Grady, *Journal of Electroanalytical Chemistry and Interfacial Electrochemistry 210*, **1986**, 189.

[63] J. Carlos Calderón, L. Ndzuzo, B.J. Bladergroen, S. Pasupathi, *Materials Today: Proceedings 5*, **2018**, 10551.

[64] J. Greeley, I.E.L. Stephens, A.S. Bondarenko, T.P. Johansson, H.A. Hansen, T.F. Jaramillo, J. Rossmeisl, I. Chorkendorff, J.K. Nørskov, *Nature Chemistry 1*, **2009**, 552.

[65] D. Kaewsai, M. Hunsom, *Nanomaterials 8*, **2018**.

[66] I.E.L. Stephens, A.S. Bondarenko, L. Bech, I. Chorkendorff, *ChemCatChem 4*, **2012**, 341.

[67] I.E.L. Stephens, A.S. Bondarenko, U. Grønbjerg, J. Rossmeisl, I. Chorkendorff, *Energy & Environmental Science 5*, **2012**, 6744.

[68] H. Ibach, *Physics of Surfaces and Interfaces*, Springer Berlin Heidelberg, **2006**.

[69] B. Hammer, J.K. Nørskov, Theoretical surface science and catalysis—calculations and concepts, *Advances in Catalysis*, Academic Press, *45* **2000**, pp. 71.

[70] P.W. Anderson, *Physical Review 124*, **1961**, 41.

[71] D.M. Newns, *Physical Review 178*, **1969**, 1123.

[72] I. Chorkendorff, J.W. Niemantsverdriet, Surface Reactivity, *Concepts of Modern Catalysis and Kinetics*, Wiley-VCH Verlag GmbH & Co. KGaA, **2005**, pp. 215.

[73] J.R. Kitchin, J.K. Norskov, M.A. Barteau, J.G. Chen, *The Journal of Chemical Physics 120*, **2004**, 10240.

[74] T. Bligaard, J.K. Nørskov, B.I. Lundqvist, Chapter 8 Understanding Heterogeneous Catalysis from the Fundamentals, *Handbook of Surface Science*, North-Holland, *3* **2008**, pp. 269.

[75] H.E. Hoster, O.B. Alves, M.T.M. Koper, *ChemPhysChem 11*, **2010**, 1518.

[76] Y.-J. Deng, V. Tripkovic, J. Rossmeisl, M. Arenz, *ACS Catalysis 6*, **2016**, 671.

[77] P. Strasser, S. Kühl, *Nano Energy 29*, **2016**, 166.

[78] P. Strasser, S. Koh, T. Anniyev, J. Greeley, K. More, C. Yu, Z. Liu, S. Kaya, D. Nordlund, H. Ogasawara, M.F. Toney, A. Nilsson, *Nat Chem 2*, **2010**, 454.

[79] J.O.M. Bockris, A.K.N. Reddy, *Modern Electrochemistry*, 2nd ed., Plenum Press, New York, *2B* **2000**, pp. Chapter 13.

[80] L. Pauling, *The Nature of Chemical Bond*, 3rd ed., Cornell University Press, Ithaca, NY, **1960**, pp. Chapters 3 and 11.

[81] W. Borchardt-Ott, Die 7 Kristallsysteme, *Kristallographie: Eine Einführung für Naturwissenschaftler*, Springer Berlin Heidelberg, Berlin, Heidelberg, **1993**, pp. 108.

[82] R.C. Alkire, P.N. Bartlett, J. Lipkowski, Nanopatterned and Nanoparticle-Modified Electrodes, *Advances in Electrochemical Sciences and Engineering*, Wiley, *17* **2017**, pp. 1.

[83] B. Lang, R.W. Joyner, G.A. Somorjai, *Surface Science 30*, **1972**, 440.

[84] S. Haussühl, *Berichte der Bunsengesellschaft für physikalische Chemie 94*, **1990**, 209.

[85] J. Friedrich, Methods for Bulk Growth of Inorganic Crystals: Crystal Growth, *Reference Module in Materials Science and Materials Engineering*, Elsevier, **2016**, pp. 1.

[86] D.M. Rowe, CRC Handbook of Thermoelectrics, CRC Press, **1995**, pp. 90.

[87] J. Clavilier, R. Faure, G. Guinet, R. Durand, *Journal of Electroanalytical Chemistry and Interfacial Electrochemistry 107*, **1980**, 205.

[88] A.T. Hubbard, *Chemical Reviews 88*, **1988**, 633.

[89] D. M. Kolb, *UHV Techniques in the Study of Electrode Surfaces*, **1987**.

[90] I. Bozovic, O. Gmbh, G. J N Bremen, Eckstein, *Reflection High-Energy Electron Diffraction as a Tool for Real-Time Characterization of Growth of Complex Oxides*, **2018**.

[91] R. Vogel, I. Kamphausen, H. Baltruschat, *Berichte der Bunsengesellschaft für physikalische Chemie 96*, **1992**, 525.

[92] A.S. Bondarenko, I.E.L. Stephens, I. Chorkendorff, *Electrochemistry Communications 23*, **2012**, 33.

[93] J. Clavilier, D. Armand, S.G. Sun, M. Petit, *Journal of Electroanalytical Chemistry and Interfacial Electrochemistry 205*, **1986**, 267.

[94] J. Clavilier, A. Rodes, K.E. Achi, M.A. Zamakhchari, *J. Chim. Phys. 88*, **1991**, 1291.

[95] N.P. Lebedeva, M.T.M. Koper, J.M. Feliu, R.A. van Santen, *Electrochemistry Communications 2*, **2000**, 487.

[96] S. Bandarenka Aliaksandr, S. Varela Ana, M. Karamad, F. Calle-Vallejo, L. Bech, J. Perez-Alonso Francisco, J. Rossmeisl, E.L. Stephens Ifan, I. Chorkendorff, *Angewandte Chemie International Edition 51*, **2012**, 11845.

[97] C.L. Green, A. Kucernak, *The Journal of Physical Chemistry B 106*, **2002**, 1036.

[98] A.A. El-Shafei, *Journal of Electroanalytical Chemistry 447*, **1998**, 81.

[99] K.J. Andersson, F. Calle-Vallejo, J. Rossmeisl, I. Chorkendorff, *Journal of the American Chemical Society 131*, **2009**, 2404.

[100] J.S. Tsay, T. Mangen, R.J. Linden, K. Wandelt, *Surface Science 482-485*, **2001**, 866.

[101] J. Knudsen, A.U. Nilekar, R.T. Vang, J. Schnadt, E.L. Kunkes, J.A. Dumesic, M. Mavrikakis, F. Besenbacher, *Journal of the American Chemical Society 129*, **2007**, 6485.

[102] E. Özer, C. Spöri, T. Reier, P. Strasser, *ChemCatChem 9*, **2016**, 597.

[103] A. M Gómez-Marín, R. Rizo, J.M. Feliu, *Some reflections on the understanding of the oxygen reduction reaction at Pt(111)*, **2013**.

[104] F. Calle-Vallejo, M.T.M. Koper, A.S. Bandarenka, *Chemical Society Reviews 42*, **2013**, 5210.

[105] S. Cherevko, S. Geiger, O. Kasian, N. Kulyk, J.-P. Grote, A. Savan, B.R. Shrestha, S. Merzlikin, B. Breitbach, A. Ludwig, K.J.J. Mayrhofer, *Catalysis Today 262*, **2016**, 170.

[106] O. Kasian, S. Geiger, P. Stock, G. Polymeros, B. Breitbach, A. Savan, A. Ludwig, S. Cherevko, K.J.J. Mayrhofer, *Journal of The Electrochemical Society 163*, **2016**, F3099.

[107] D. Schmeisser, K. Jacobi, *Surface Science 88*, **1979**, 138.

[108] W. Gaebler, K. Jacobi, W. Ranke, *Surface Science 75*, **1978**, 355.

[109] L.B. Rogers, D.P. Krause, J.C. Griess, D.B. Ehrlinger, *Journal of The Electrochemical Society 95*, **1949**, 33.

[110] T. Mills, G.M. Willis, *Journal of The Electrochemical Society 100*, **1953**, 452.

[111] R.C. DeGeiso, L.B. Rogers, *J. Electrochem. Soc. 106*, **1959**, 433.

[112] D.M. Kolb, M. Przasnyski, H. Gerischer, *Journal of Electroanalytical Chemistry and Interfacial Electrochemistry 54*, **1974**, 25.

[113] R.R. Adžić, *Israel Journal of Chemistry 18*, **1979**, 166.

[114] S. Szabó, *International Reviews in Physical Chemistry 10*, **1991**, 207.

[115] A.A. El-Shafei, *Journal of Electroanalytical Chemistry 380*, **1995**, 269.

[116] C. Kim, T. Möller, J. Schmidt, A. Thomas, P. Strasser, *ACS Catalysis 9*, **2019**, 1482.

[117] E. Özer, B. Paul, C. Spöri, P. Strasser, *Small Methods 0*, **2018**, 1800232.

[118] T. Reier, *Structure-activity-stability and in-situ Raman spectroscopic studies of oxygen evolution catalysts in acidic environment* **2016**, http://dx.doi.org/10.14279/depositonce-5010

[119] L. Trotochaud, S.L. Young, J.K. Ranney, S.W. Boettcher, *Journal of the American Chemical Society 136*, **2014**, 6744.

[120] P.E. Blöchl, *Physical Review B 50*, **1994**, 17953.

[121] G. Kresse, D. Joubert, *Physical Review B 59*, **1999**, 1758.

[122] G. Kresse, J. Furthmüller, *Physical Review B 54*, **1996**, 11169.

[123] G. Kresse, J. Furthmüller, *Computational Materials Science 6*, **1996**, 15.

[124] J.P. Perdew, K. Burke, M. Ernzerhof, *Physical Review Letters 77*, **1996**, 3865.

[125] Z. Jusys, H. Massong, H. Baltruschat, *Journal of The Electrochemical Society 146*, **1999**, 1093.

[126] A.H. Wonders, T.H.M. Housmans, V. Rosca, M.T.M. Koper, *Journal of Applied Electrochemistry 36*, **2006**, 1215.

[127] S. Geiger, *Stability investigations of iridium-based catalysts towards acidic water splitting* **2018**, https://hss-opus.ub.ruhr-uni-bochum.de/opus4/frontdoor/index/index/docId/5589

[128] T. Bligaard, J.K. Nørskov, *Electrochimica Acta 52*, **2007**, 5512.

[129] Y. Lee, J. Suntivich, K.J. May, E.E. Perry, Y. Shao-Horn, *The Journal of Physical Chemistry Letters 3*, **2012**, 399.

[130] N. Mamaca, E. Mayousse, S. Arrii-Clacens, T.W. Napporn, K. Servat, N. Guillet, K.B. Kokoh, *Applied Catalysis B: Environmental 111-112*, **2012**, 376.

[131] H.N. Nong, L. Gan, E. Willinger, D. Teschner, P. Strasser, *Chemical Science 5*, **2014**, 2955.

[132] G. Sanchez Casalongue Hernan, L. Ng May, S. Kaya, D. Friebel, H. Ogasawara, A. Nilsson, *Angewandte Chemie International Edition 53*, **2014**, 7169.

[133] M. Favaro, C. Valero-Vidal, J. Eichhorn, F.M. Toma, P.N. Ross, J. Yano, Z. Liu, E.J. Crumlin, *Journal of Materials Chemistry A 5*, **2017**, 11634.

[134] R.L. Doyle, M.E.G. Lyons, The Oxygen Evolution Reaction: Mechanistic Concepts and Catalyst Design, *Photoelectrochemical Solar Fuel Production: From Basic Principles to Advanced Devices*, Springer International Publishing, Cham, **2016**, pp. Chapter 2.

[135] L. Gong, D. Ren, Y. Deng, B.S. Yeo, *ACS Applied Materials & Interfaces 8*, **2016**, 15985.

[136] N. Nong Hong, H.S. Oh, T. Reier, E. Willinger, M.G. Willinger, V. Petkov, D. Teschner, P. Strasser, *Angewandte Chemie 127*, **2015**, 3018.

[137] C. Wang, Y. Sui, M. Xu, C. Liu, G. Xiao, B. Zou, *ACS Sustainable Chemistry & Engineering 5*, **2017**, 9787.

[138] H. Bode, K. Dehmelt, J. Witte, *Electrochimica Acta 11*, **1966**, 1079.

[139] D.A. Corrigan, S.L. Knight, *Journal of The Electrochemical Society 136*, **1989**, 613.

[140] L.C. Seitz, C.F. Dickens, K. Nishio, Y. Hikita, J. Montoya, A. Doyle, C. Kirk, A. Vojvodic, H.Y. Hwang, J.K. Norskov, T.F. Jaramillo, *Science 353*, **2016**, 1011.

[141] S. Rudi, C. Cui, L. Gan, P. Strasser, *Electrocatalysis 5*, **2014**, 408.

[142] G. García, M.T.M. Koper, *Physical Chemistry Chemical Physics 10*, **2008**, 3802.

[143] C. Cui, M. Ahmadi, F. Behafarid, L. Gan, M. Neumann, M. Heggen, B.R. Cuenya, P. Strasser, *Faraday Discussions 162*, **2013**, 91.

[144] V. Beermann, M. Gocyla, S. Kühl, E. Padgett, H. Schmies, M. Goerlin, N. Erini, M. Shviro, M. Heggen, R.E. Dunin-Borkowski, D.A. Muller, P. Strasser, *Journal of the American Chemical Society 139*, **2017**, 16536.

[145] M. Chatenet, Y. Soldo-Olivier, E. Chaînet, R. Faure, *Electrochimica Acta 53*, **2007**, 369.

[146] J.S. Spendelow, J.D. Goodpaster, P.J.A. Kenis, A. Wieckowski, *The Journal of Physical Chemistry B 110*, **2006**, 9545.

[147] N.P. Lebedeva, A. Rodes, J.M. Feliu, M.T.M. Koper, R.A. van Santen, *The Journal of Physical Chemistry B 106*, **2002**, 9863.

[148] A. López-Cudero, A. Cuesta, C. Gutiérrez, *Journal of Electroanalytical Chemistry 579*, **2005**, 1.

[149] T.R. Garrick, T.E. Moylan, M.K. Carpenter, A. Kongkanand, *Journal of The Electrochemical Society 164*, **2017**, F55.

[150] F. Hasché, M. Oezaslan, P. Strasser, *Physical Chemistry Chemical Physics 12*, **2010**, 15251.

[151] G. Li, L. Anderson, Y. Chen, M. Pan, P.-Y. Abel Chuang, *Sustainable Energy & Fuels 2*, **2018**, 237.

[152] P. Ferrin, S. Kandoi, A.U. Nilekar, M. Mavrikakis, *Surface Science 606*, **2012**, 679.

[153] C.J. Hagedorn, M.J. Weiss, W.H. Weinberg, *Physical Review B 60*, **1999**, R14016.

[154] W.P. Krekelberg, J. Greeley, M. Mavrikakis, *The Journal of Physical Chemistry B 108*, **2004**, 987.

[155] D. Lerch, A. Klein, A. Schmidt, S. Müller, L. Hammer, K. Heinz, M. Weinert, *Physical Review B 73*, **2006**, 075430.

[156] M.R. Babapour Ghadikolaee, E. Talebi Ghadikolaee, *Journal of Fusion Energy 31*, **2012**, 569.

[157] C. Gammer, C. Mangler, C. Rentenberger, H.P. Karnthaler, *Scripta Materialia 63*, **2010**, 312.

[158] http://www.univie.ac.at/pasad/, **PASAD**, access date: 18.05.18

[159] M.C. Biesinger, B.P. Payne, A.P. Grosvenor, L.W.M. Lau, A.R. Gerson, R.S.C. Smart, *Applied Surface Science 257*, **2011**, 2717.

[160] S. Trasatti, *Electrochimica Acta 29*, **1984**, 1503.

[161] S. Ardizzone, A. Carugati, S. Trasatti, *Journal of Electroanalytical Chemistry and Interfacial Electrochemistry 126*, **1981**, 287.

[162] L.A. da Silva, V.A. Alves, M.A.P. da Silva, S. Trasatti, J.F.C. Boodts, *Electrochimica Acta 42*, **1997**, 271.

[163] J. Juodkazytė, B. Šebeka, I. Valsiunas, K. Juodkazis, *Electroanalysis 17*, **2005**, 947.

[164] B.E. Conway, J. Mozota, *Electrochimica Acta 28*, **1983**, 9.

[165] T. Reier, M. Oezaslan, P. Strasser, *ACS Catalysis 2*, **2012**, 1765.

[166] S. Cherevko, S. Geiger, O. Kasian, A. Mingers, K.J.J. Mayrhofer, *Journal of Electroanalytical Chemistry 773*, **2016**, 69.

[167] H.N. Nong, T. Reier, H.-S. Oh, M. Gliech, P. Paciok, T.H.T. Vu, D. Teschner, M. Heggen, V. Petkov, R. Schlögl, T. Jones, P. Strasser, *Nature Catalysis*, **2018**.

[168] V.A. Saveleva, L. Wang, D. Teschner, T. Jones, A.S. Gago, K.A. Friedrich, S. Zafeiratos, R. Schlögl, E.R. Savinova, *The Journal of Physical Chemistry Letters 9*, **2018**, 3154.

3 List of Figures

4 List of Tables

5 List of Abbreviations

Ac	Acetate
AES	Atomic emission spectroscopy
AFM	Atomic force microscopy
AP	as-prepared
DEMS	Differential electrochemical mass spectrometry
DOF	Density of states
FE	Faraday efficiency
FIB	Focused ion beam
ICP-MS	Inductively coupled plasma-mass spectrometry
LEED	Low-energy electron diffraction
NEXAFS	Near-edge x-ray absorption fine structure
OER	Oxygen evolution reaction
PEIS	Potentio electrochemical impedance spectroscopy
PEMFC	Proton exchange membrane fuel cell
POM	Polyoxymethylene
RDE	Rotating disc electrode
RHE	Reversible hydrogen electrode
SEM	Scanning electron microscopy
SHE	Standard hydrogen electrode
SPV	Stepped potential voltammetry
STP	Standard temperature and pressure
(HR)TEM	(High-resolution) transmission electron microscopy
UHV	Ultra-high vacuum
UPD	Underpotential deposition
XAS	X-ray absorption spectroscopy
XPS	X-ray photoelectron spectroscopy